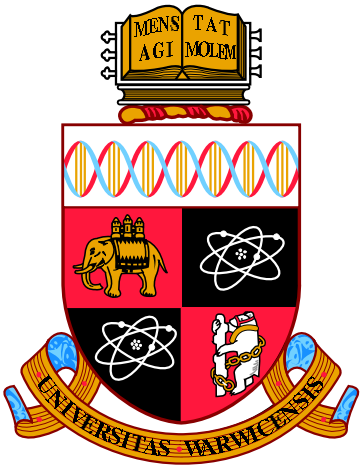

Photoelectron diffraction determination of adsorbate structures

by

Dagmar Kreikemeyer Lorenzo

Thesis

Submitted to the University of Warwick

for the degree of

Doctor of Philosophy

Physics

December 2011

THE UNIVERSITY OF WARWICK

Contents

List of Tables

List of Figures

Acknowledgments

First, I would like to thank my supervisor Phil Woodruff, for offering me the oppurtunity to work on this project and for always being positive and supportive, even when the experiments weren't as straightforward as we expected. But especially, I would like to thank him for running the group in such a kind way. It has been a pleasure to work in such a nice, friendly and helpful environment.

Obviously, I am very grateful to the person with whom I spent most of the time during the first three years of my PhD. Thank you, Werner, for your patience in helping me in my first weeks at the Fritz with the code and with all the Igor macros. It was a lot of fun to share three years of experiments and many scientific (and non-scientific) conversations in the office with you. I would not have made it without you. And of course, I also have to thank you for teaching me weird Austrian expressions.

I also want to thank my colleagues at Warwick: David, Tsenolo and Daryl, for their help in the numerous beamtimes at BESSY and Matt, with the DFT calculations. David, a special thanks for the enormous help with the code and all my computing problems. Without your help I would have panicked many more times, and it also compensated for the many times you broke the thermocouple at BESSY. Tsenolo, thank you for answering all my questions from my very first day and for the funny nights at BESSY.

This work could not have been done without our technicians at BESSY, Willy Mahler and Birgitt Zada. Additionally, I want to thank the members of the "Electronic Structure" group of the Inorganic Chemistry Department of the Institute, for their help and support during our "high-pressure" beamtime at ISISS.

Also to Dr. Kuhlenbeck's group for the very interesting beamtime. I learned a lot about LEED and mixed oxides in those two weeks. Elena, a big thanks for sharing with me very enjoyable lunchtimes.

I would like to thank the whole Molecular Physics department, in particular, Gerard Meijer, for treating me as a "normal" MP member, even though officially I was not; and also to Inga and Andrea for running the department so well, and for always being there to help us with so many problems. Thank you to all the PhD students, Diplomanden, Post-Docs, and everyone else, for all the Wandertage, Christmas parties, wine tastings, Kaffee und Kuchen, and countless social events. You have been my family over these three and a half years in Berlin. Especially I want to thank two people who have become more than just colleagues. Thank you to Cyndi (ay Dios mío) and Adela for cheering me up in the bad moments, and sharing with me the good ones.

I don't want to forget my friends in Madrid, who shared with me my first steps in the physics business: Pablo G., Eva, Miguel, Sara, Erika and Christian. For the brunches, the cinema evenings, and the dancing nights, I want to thank my (physicist) friends in Berlin: Mariana, Teo, Rocío, Isa, Jesús, Hakim, Ania, Eli, and Cristina y Juan. But especially, I want to thank my best friend, Pilar, for taking such good care of me. I will miss you a lot.

I cannot forget my family, without which I would not have started this adventure. Thanks to my brother Christian and his family, who are very interested in vectors, to my aunt Bego and of course, to my parents. Papá y mamá, gracias por vuestro apoyo en todos los pasos de mi vida y sobre todo, gracias por creer en mi más que yo misma.

And of course, I want to thank the person who has helped and supported me most over the last years, especially the last months. Frank: thanks for helping me with the Latex problems, for your patience and your understanding, and for all your love even when I was under a lot of stress. Ich freu mich auf unsere gemeinsame Zukunft. Te quiero. Mucho.

Declarations

This thesis is submitted to the University of Warwick for the admission of the degree of Doctor of Philosophy. The work presented in this thesis is my own, except where it is stated otherwise. The work presented here was performed at the Fritz Haber Institute of the Max Planck Society and at the synchrotron radiation facility Berliner Elektronenspeicherring-Gesellschaft für Synchrotronstrahlung (BESSY) under the supervision of Professor D.P. Woodruff in the period of May 2008 to December 2011. No part of this material has been previously submitted to this or any other institution for admission of any degree.

Part of this work was presented at the German National Conferences in Dresden 2009 and 2011 and Regensburg 2010; at the 10th International Conference on Atomically Controlled Surfaces, Interfaces and Nanostructures (ACSIN) (Granada, Spain, 2009); at the 18th International Vacuum Conference (IVC) (Beijing, China, 2010); at the 18th Interdisciplinary Surface Science Conference (ISSC) (Warwick, England); and at the 28th European Conference on Surface Science (ECOSS) (Wroclaw, Poland, 2011).

Some articles based on this work have been published:

- D. Kreikemeyer-Lorenzo, M.K. Bradley, W. Unterberger, D.A. Duncan, T.J. Lerotholi, J. Robinson, and D.P. Woodruff, *The structure of methoxy species on Cu(110). A combined photoelectron diffraction and density functional theory determination*, Surface Science, vol. 605, 193, (2010)

- M.K. Bradley, D. Kreikemeyer-Lorenzo, W. Unterberger, D.A. Duncan, T.J. Lerotholi, J. Robinson, and D.P. Woodruff, *Methoxy species on Cu(110). Un-*

derstanding the local structure of a key catalytic reaction intermediate, Physical Review Letters, vol. 105, 086101, (2010)

- D. Kreikemeyer-Lorenzo, W. Unterberger, D.A. Duncan, M.K. Bradley, T.J. Lerotholi, J. Robinson, and D.P. Woodruff, *Face-Dependent Bond Lengths in Molecular Chemisorption: The Formate Species on Cu(111) and Cu(110)*, Physical Review Letters, vol. 107, 046102, (2011)

Other details of this work are in preparation for publication.

Abstract

Scanned-energy mode photoelectron diffraction (PhD) is a well-known method to determine quantitatively the local structure of adsorbates at surfaces. In this thesis, it has been employed to determine the adsorption site of a selection of molecules on surfaces.

The adsorption on Cu(110), of methoxy (CH_3O), an intermediate in the catalytic decomposition of methanol (CH_3OH), has been studied. O 1s PhD spectra show the strongest modulation at 30° and 40° polar emission angles, both in the [1 $\bar{1}$ 0] azimuth, which is consistent with a bridge position adsorption site in the [1 $\bar{1}$ 0] azimuth. The subsequent analysis, as well as parallel DFT studies, confirms two bridge adsorption sites, with different bond lengths to the underneath copper atoms. A tilt of the molecules of 37° in the [1 $\bar{1}$ 0] azimuth is also observed, with the carbon atoms pointing in opposite directions for every adsorption site. This tilt creates a zig-zag model, which fits with an old STM [1] study.

Formate (HCOO), a surface intermediate of the catalytic decomposition of formic acid (HCOOH), has been studied on two different faces of copper, Cu(110) and Cu(111). Although the adsorption sites obtained for both surfaces is similar, namely a short-bridge site slightly off atop, a significant difference of ≈ 0.1 Å in the copper-oxygen bond lengths is found, being 1.99 Å for Cu(111) and 1.90 Å for Cu(110).

In this thesis, it is demonstrated that it is possible, though very challenging, to perform PhD successfully under higher pressures. Methanol oxidation on Cu(110) has been studied under reaction conditions. At temperatures below ≈ 450 K, the adsorption sites of methoxy and formate, the most important surface intermediates of this reaction, have been proved to be similar as in the previous studies performed in ultra high vacuum.

A recent investigation of two different organic molecules, azobenzene ($C_{12}H_{10}N_2$) and aniline (C_6H_7N), on rutile TiO_2(110) and anatase TiO_2(101) surfaces with scanning tunneling microscopy (STM) [2] indicates that both molecules lead the formation of the same superstructure, believed to be of a common species, phenyl imide (C_6H_5N). PhD has been exploited to determine the local adsorption site of adsorbed species formed by both molecules on rutile TiO_2(110). N 1s photoelectron diffraction data are almost identical for both molecules, providing further support for a common surface species with the same, or a closely similar. Additional NEXAFS results support these results, implying that the local adsorption site of azobenzene and aniline is indeed the same. PhD results, which show the largest modulation amplitude at normal emission, suggests that the phenyl imide bonds via the N atoms atop a five-fold coordinated surface Ti atom, with the molecular plane tilted with respect to the surface normal, with a N-Ti bond length of 1.77 Å.

[1] F. Leibsle, S. Francis, S.Haq, and M. Bowker, *Aspects of formaldehyde synthesis on Cu(110) as studied by STM*, Surf. Sci. **318**, 46 (1994).

[2] S.-C. Li, and U. Diebold, *Reactivity of TiO_2 rutile and anatase surfaces toward nitroaromatics*, J. Am. Chem. Soc. **134**, 64 (2010).

Abbreviations

- AFM Atomic force microscopy
- BESSY Berliner Elektronenspeicherring-Gesellschaft für Synchrotronstrahlung
- CAE Constant analyser energy
- CASTEP Cambridge Serial Total Energy Package
- DFT Density functional theory
- EELS Electron energy loss spectroscopy
- ESCA Electron spectroscopy for chemical analysis
- EXAFS Extended X-ray absorption fine structure
- FCC Face-centered cubic
- GGA Generalized Gradient Approximation
- ISISS Innovative Station of In situ Spectroscopy
- LEED Low energy electron diffraction
- MEIS Medium energy ion scattering
- NEXAFS Near edge X-ray absorption fine structure
- NIXSW Normal incidence X-ray standing wavefield absorption
- PBE Perdew-Burke-Ernzerhof

- PhD Scanned-energy mode photoelectron diffraction
- RAIRS Reflection absorption infra-red spectroscopy
- RPBE Revised Perdew-Burke-Ernzerhof
- SEXAFS Surface extended X-ray absorption fine structure
- SR Synchrotron radiation
- STM Scanning tuneling microscopy
- sXPS Soft X-ray photoelectron spectroscopy
- SXRD Surface X-ray diffraction
- TPD Temperature programmed desorption
- TPRS Temperature programmed reaction spectroscopy
- TSP Titanium sublimation pump
- UHV Ultra high vacuum
- UPS Ultra-violet photoemission spectroscopy
- XANES X-ray absorption near-edge structure
- XPD X-ray photoelectron diffraction
- XPS X-ray photoelectron spectroscopy

Chapter 1

Introduction

Surface science has experienced an enormous boost in the last few decades. This increasing interest arises from the importance of surface properties for many applications in "real life". One of the reasons for this interest of surface science is its application in heterogeneous catalysis due to the great amount of chemical reactions that occur on surfaces. The understanding of how the surfaces behave can enhance these catalytic processes. Surfaces are a kind of "defect" of solid state materials, and breaking the periodicity of a three dimensional solid can lead to changes, for instance, in the surface and electronic structure.

One of the chemical reactions studied in this thesis is the catalytic decomposition of methanol to produce formaldehyde, one of the most extended processes in industry. Approximately 21 million tons of formaldehyde are produced in one year in the whole world. Many catalytic processes, such as the one just mentioned, are very sensitive to the local structure of the surface and of the active sites. If the local geometry of these active sites on the surfaces can be determined, the catalytic reactions might be performed faster and more easily, thus, reducing the time and the cost of the catalytic process. The determination of the local geometry of the reaction intermediates on the surface in a quantitative way is the motivation for the main part of the work presented in this thesis.

Very important for the field of surface science, was the development of new experimental techniques. In the 1980s, scanning probe microscopy techniques, such as the scanning tunneling microscope (STM) [1, 2] or the atomic force microscopy (AFM) [3], represented a major breakthrough, allowing one to observe the surfaces at an atomic scale in real space. X-ray photoelectron spectroscopy (XPS) [3–5] and ultra-violet photoemission spectroscopy (UPS) [3] provide information on the composition of the sample. Using other spectroscopic techniques, such as reflec-

tion absorption infra-red spectroscopy (RAIRS) [6] or electron energy loss spectroscopy (EELS) [7], the vibrations of molecules on surfaces can be determined. However, these techniques cannot provide quantitative information on the structure of the surface. Surface extended X-ray fine structure (SEXAFS) [8] can determine adsorbate-substrate bond lengths and near edge X-ray absorption fine structure (NEXAFS) [3, 9–12] provides information on the bond lengths within molecular adsorbates and also on the bond angles. Other techniques, such as low energy electron diffraction (LEED) [3, 13, 14], or scanned-energy mode photoelectron diffraction (PhD) [3, 8, 15, 16] provide information on the local geometry of surfaces, and also the structure of reconstructed surfaces after adsorbing molecules on them. Density functional theory (DFT) [17–20] calculations have improved in the past years due to the accessibility to better and faster computers. Many DFT studies have been published on the determination of surface structures based on calculated minimum energy structures with considerably success, although some of the conclusions of these studies have been proved to be wrong. The combination of two or more of these surface sensitive techniques helps to understand the surfaces better. In this thesis, PhD has been the main technique to investigate the adsorption site of different molecules adsorbed on surfaces.

Scanned-energy photoelectron diffraction exploits the coherent interference between the directly emitted wavefield from a core level of an atom adsorbed on the sample and the components of the same wavefield backscattered by the neighbouring substrate atoms. By scanning the photon energy, the photoelectron energy changes, and the backscattered waves switch in and out of phase with the directly-emitted wave, modulating the intensity. These variations in the intensity depend directly on the relative positions between the emitter (the adsorbate atom) and the scatterers (the neighbour atoms). Information on the bond lengths between the adsorbate and the substrate atoms are also provided. This technique has the advantages that it is elemental and chemical-state specific. PhD has been proved to be a well-established technique in determining surface structures under ultra high vacuum (UHV).

The study of adsorbates on surfaces was promoted in the 1960s by the introduction of UHV, and also by stabilising the molecules on the surfaces at low temperatures (significant lower than under reaction conditions). In UHV, the conditions ($P < 10^{-9}$ mbar) are almost perfect and experiments can be carried out without being contaminated by residual gases. On the other hand, these conditions are far away from "real life", as for example, the reaction conditions (high temperatures and pressures) necessary for industrial processes. In the past few years, a few techniques have tried to close the gap between UHV and realistic conditions. X-ray

photoelectron spectroscopy has been applied successfully to characterise surfaces at higher-pressures, and STM has been able to take images of surface reactions. However, so far, no quantitative structural method that does not rely on long-range order has been applied under reaction conditions. In this work, scanned-energy mode photoelectron diffraction has been applied under "high" pressures for the first time in order to determine the local structure of surface intermediates of a chemical reaction under steady-state conditions, thus closing the gap between UHV and industrial processes.

1.1 Organisation of the thesis

This thesis is a report of work performed at the Fritz Haber Institute and the experimental data collected at the synchrotron radiation facility BESSY II, in Berlin, Germany, in the period of May 2008 to December 2011. The work presented here covers the study of the adsorption site of the most important surface intermediates of methanol oxidation, methoxy and formate, on Cu(110) under ultra high vacuum and under reaction conditions. The adsorption of formate on Cu(111) was also studied. Finally the adsorption of two other molecules, azobenzene and aniline, was studied on the (110) face of rutile titanium dioxide. For these investigations, energy-scanned photoelectron diffraction was the main technique used, but in the case of aniline and azobenzene on TiO_2 near edge X-ray absorption fine structure was also employed. The organisation of the thesis is the following:

Chapter 2 is concerned with the experimental details related to this thesis. First, details of the beamline at BESSY are provided. X-ray photoelectron spectroscopy is then introduced. A larger section about photoelectron diffraction is then introduced. This section contains information on the experimental chamber, the theoretical background of the technique and it describes the data collection and the procedure used for the structure determination. Finally, two other complementary techniques are introduced, LEED and NEXAFS.

Chapters 3 to 6 contain the experimental results and associated computational modelling for the systems studied: methoxy on Cu(110), formate on Cu(110) and on Cu(111) and azobenzene and aniline on TiO_2. These experiments have been measured under ultra high vacuum. Methanol oxidation on Cu(110) under reaction conditions has also been studied and is presented in chapter 5. Each chapter explains the cleaning and dosing procedure; the characterisation of the sample by X-ray spectroscopy; the PhD results are then shown, along with the structural models found through theoretical calculations and the comparison between the results

of experiments and theory. Finally, a discussion is included.

Chapter 7 comprises a summary of all the work presented in this thesis and includes suggestions for future investigations.

Chapter 2

Experimental details

The goal of this thesis was the determination of the local structure of different adsorbates on metal and oxide surfaces. The main technique used for this purpose was scanned-energy photoelectron diffraction (PhD), a well-established structural technique, which provides direct information on the relative positions of the adsorbate and surface atoms. PhD is based on X-ray photoelectron spectroscopy (XPS), and takes advantage of its elemental and chemical specificity. One of the main advantages of PhD with respect to other structural methods (e.g., LEED) is that it does not require long range periodicity. However, other experimental methods were also employed as a support when PhD could not give an answer to the raised questions. Near edge X-ray absorption fine structure (NEXAFS) was used in the study of nitroaromatic molecules on titanium dioxide to provide extra information on the orientation and tilt of the adsorbates on the surface, information that could not be obtained from PhD. Low energy electron diffraction (LEED) together with XPS were used to characterise the sample and check its cleanliness.

PhD and NEXAFS require the use of a tunable X-ray source with very intense light. For that, all the experiments presented here were performed in the synchrotron radiation facility in Berlin, Germany (BESSY II). XPS can be carried out with synchrotron radiation (SR) or an external source, but in this thesis all the XP spectra were taken also with synchrotron radiation.

In this chapter all the experimental details related to this thesis will be treated. First, a brief explanation of synchrotron radiation and a description of the experimental beam line will be presented. Then, all the experimental methods will be explained, with an emphasis on photoelectron diffraction and all the aspects of the experiments (data collection, experimental equipment, etc...).

2.1 Synchrotron radiation

The electromagnetic radiation emitted when near relativistic charged particles travel in curved paths is called synchrotron radiation [21]. This radiation can be generated over a broad range of wavelengths, from visible light to the hard X-ray of the electromagnetic spectrum. The importance of synchrotron radiation relies on its high intensity, its broad spectral range and other properties such as collimation, polarisation, coherence, etc... These properties make synchrotron radiation a very useful tool for the study of surface science, and in particular, its tunability makes it essential for photoelectron diffraction.

A storage ring synchrotron radiation source is a circular particle accelerator that enables a current of electrons to circulate at relativistic velocities for several hours. A storage ring consists of a sequence of dipole (bending) magnets and quadrupole (focusing and defocussing) magnets joined by field-free regions, called drift spaces. The circular shape of the accelerator allows the electrons to travel in this closed orbit for several hours. Synchrotron radiation is emitted from all curved parts of the ring. Currently there are around fifty synchrotron radiation facilities all over the world, but all the experiments presented in this thesis were carried out in the Berliner Elektronenspeicherring-Gesellschaft für Synchrotronstrahlung (BESSY II) in Berlin, Germany. BESSY has a circumference of 240 m, with $\approx$ 50 beamlines or experimental stations. The beamline where most of the experiments were performed was the UE56-2_PGM-2; only the study of the oxidation of methanol at high-pressures was performed at the beamline ISISS (Innovative Station of In situ Spectroscopy). BESSY II is one of the so-called third generation storage rings. This type of synchrotron source is characterised by lower electron beam emittance and many straight sections for insertion devices, such as wigglers or undulators.

The electron beam is not generated in the storage ring. It is instead generated by a thermoionic gun (as is depicted in Figure 2.1), where the electrons are emitted by a hot cathode and then accelerated and focused with the help of an anode electrode. The electron beam is then focused into the microtron, which is a pre-injection device where the beam gains energy to approximately a few MeV. A microtron is a type of cyclotron, where the electrons pass through an acceleration voltage and due to a magnetic field, they are moving in circular orbits and re-encounter the acceleration voltage every time. When the electron beam reaches the desired energy, it is injected into the circular accelerator with the help of a bending magnet. The electrons are then accelerated to $\sim$ 1.7 GeV. Finally, the electrons are inserted into the storage ring.

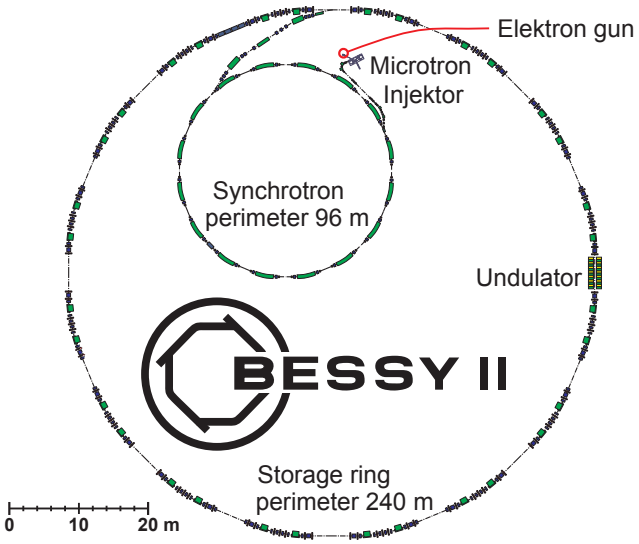

Figure 2.1: Diagram of the synchrotron radiation facility in Berlin, BESSY II (taken from [22]).

There are three modes of operation in the storage ring in Berlin, depending on how are the electrons injected into it:

1. Mutibunch mode (the one used in this thesis), where around 350 packets are injected in the beam separated by a few nanoseconds.

2. Single bunch mode, where a single packet is injected in the storage ring and every packet returns every 800 ns. This mode is typically used for time resolved experiments.

3. Low-alpha mode. This mode can be operated in single and multibunch mode. Here, the photon pulses are shortened (2 ps vs 30 ps in the normal mode) enabling time resolved experiments in the multibunch mode. Furthermore, the lengths of the electron packets are decreased providing Terahertz radiation.

As mentioned before, one of the characteristic of third generation storage rings is the insertion of magnetic devices other than bending magnets which enhance the spectral properties of the radiation [21]. These devices can be wigglers and undulators. The spontaneous emission (synchrotron radiation) of electrons traveling close to the speed of light falls into a narrow cone centered around the direction of electron motion. The opening angle of this cone is of the order of γ^{-1} ,where γ is the Lorentz factor (see Figure 2.2).

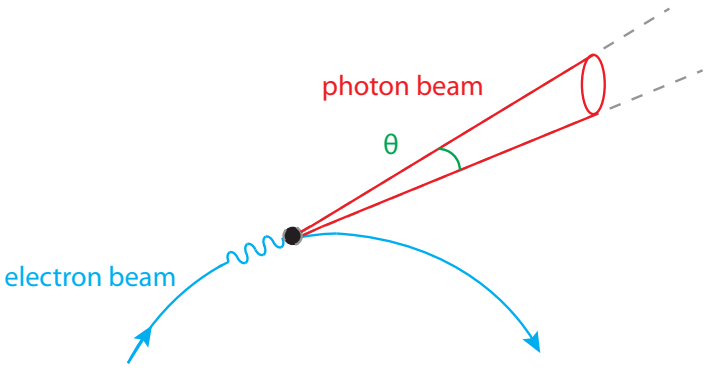

Figure 2.2: Schematic diagram of the radiation beam traveling in a curved path emitting photons from an undulator into a narrow cone of natural emission angle $\cong \gamma^{-1}$. The energy of the electrons is $E{=}\gamma mc^2$.

The cone of light produced by a bending magnet [21] is a continuous band of radiation in the bending plane, with a fan-shaped beam of photons (broad in the horizontal plane but small in the vertical plane). A wiggler is a succession of magnetic poles with alternating polarity. Each pole bends the electron beam through a relative large angle in comparison with mc^2/E. These devices are placed in the straight parts of the ring, but because the alternating deflections counteract each other, the beam is not bent and the electrons continue traveling in their orbit. The flux and brightness of the beam are intensified by N (N is the number of poles of the device). An undulator, which is the device used in the UE56-2_PGM-2 at BESSY, works in principle as a wiggler (alternating poles) with the difference that now the bending angle is of the order of mc^2/E. In this way, the angle of emission is comparable with the natural emission angle of the synchrotron radiation, $\cong \gamma^{-1}$ (Figure 2.2) and therefore, the intrinsic brightness of the synchrotron radiation is preserved in the horizontal and vertical planes. Also, coherent interference takes place in an undulator resulting in a spectrum enhanced at certain wavelengths, whereas in a wiggler the radiation adds incoherently resulting in a spectrum that is smooth and continuous.

The undulator device working at the mentioned beamline used at BESSY comprises two undulators, one on top of the other. Each of the undulators consists of a series of dipole magnets of 31 periods (see Figure 2.3) of 56 mm. The coherent interference of light emitted from different periods provides a photon beam with a peak intensity much higher than the emission light from a bending magnet. Using only one of the undulators, linearly polarised light can be achieved, as it is necessary

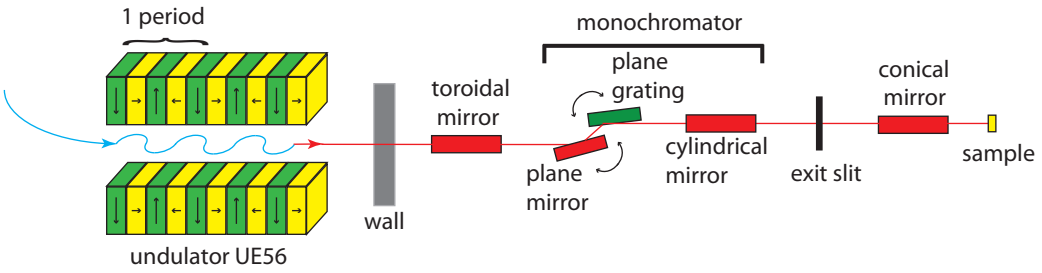

Figure 2.3: Design of the UE56-2_PGM-2 beamline at BESSY II in Berlin (not to scale).

for the photoelectron diffraction experiments.

Figure 2.3 shows a schematic diagram of the UE56-2_PGM-2 beamline at BESSY II. The photon beam, after passing through the undulator (and the wall separating the storage ring from the experimental hall) encounters a toroidal mirror which focuses the beam horizontally and collimates the beam in the vertical direction. After that, the radiation beam passes through the monochromator which comprises a plane mirror, the plane gratings and a cylindrical mirror. The objective of the monochromator is to diffract the beam by a grating (400 l/mm or 1200 l/mm) to select the pertinent energy for the experiment. The plane mirror can rotate in order to achieve a constant beam position and the cylindrical mirror immediately after the plane grating focuses the diffracted photon beam vertically into the exit slit. Finally, the radiation beam travels through a conical mirror, which re-focuses the beam again. The focus of the beam is 20 - 200 μm vertically, depending on the settings of the exit slit, and 900 μm horizontally. However, the flux density of the spot is too high for the photoelectron diffraction experiments, leading to damage of the sample, so a transfer tube is placed between the last flange of the beamline and the experimental chamber. This transfer tube is around 1.5 m long, and thus defocussing of the light allows the experiments to be carried out. The experiments presented in this thesis require photon energies in the range of 200 to 900 eV. The desired energy can be selected by controlling the undulator and the monochromator. Using the third harmonic of the undulator and with the 400 l/mm grating, energies in the mentioned range were achieved with a high photon flux.

2.2 X-ray photoelectron spectroscopy

X-ray photoelectron spectroscopy (XPS) is a surface analysis technique based on the photoelectric effect, which was first explained by Einstein [23] in 1905. The idea

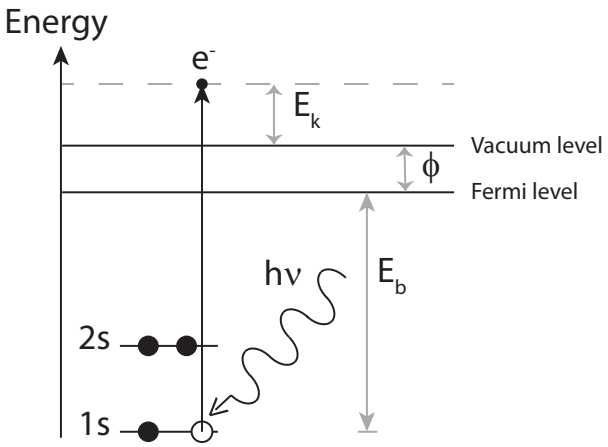

Figure 2.4: Schematic diagram of the photoemission process from a 1s core level. E_b denotes the binding energy, E_k denotes the kinetic energy and ϕ the work function.

of this technique is that an incoming photon from an X-ray source impinges in a surface inducing the emission of an electron. The only condition that the photon has to fulfill is that its energy (E_{phot}=h·ν) is greater than the binding energy of the electron and the work function of the solid (where the work function is the minimum energy required to remove an electron from the Fermi level to the vacuum level). XPS is a very useful tool in surface science, mainly due to its surface specificity. This property is enhanced by the use of the rather low kinetic energies (100 - 900 eV) used in this work, which decreases the inelastic mean-free-path of the photoelectrons and therefore its mean escape depth. This ensures that only electrons from the outermost layers are being detected. Also the choice of the emission angle can determine the surface specificity (at grazing angles the technique is more surface specific than at normal emission).

Photoelectron spectroscopy can be performed at photon energies between approximately 5 and 2000 eV. At energies lower than 100 eV, electrons from the valence band of the surface are excited and this technique is called ultra-violet photoemission spectroscopy (UPS). However, if photons with energies between 100 and 2000 eV are used, electrons from the core levels from atoms in the surface are also emitted. XPS performed in the 100-1000 eV range is known as soft X-ray photoelectron spectroscopy (sXPS). In the work presented in this thesis, all measurements were taken in this range, due to the higher photoionisation cross-sections for low atomic number elements (such as the ones measured here: O, N, C). Binding energies of the core electrons in a solid are characteristic of each element and are relatively

insensitive to changes in the valence electrons due to, for example, chemical bonding with other atoms in a solid. This property ensures that the technique is element specific. The process of photoemission from a core level is illustrated in Figure 2.4.

The energy of the emitted electron, E_k, which is detected by the analyser, is given by:

$$E_k = h\nu - E_b - \phi \tag{2.1}$$

where ϕ is the work function of the sample, and E_b is the binding energy of a core level with respect to the highest occupied level of the solid, i.e., the Fermi level in the case of a metal and the top of the valence band for a semiconductor.

Another important characteristic of XPS is the possibility of probing the chemical environment of the surface species. Due to this characteristic this technique is also known as "electron spectroscopy for chemical analysis" (ESCA). The exact binding energy of a core electron from a surface atom depends on the local environment of the sample. Changes in the chemical environment will influence the electronic structure of the atom. Hence, atoms of the same element with different chemical environments will show slightly different binding energies. These changes in the energy are called chemical shifts and can be from tenths of an eV to as much as a few eV. Depending on the bandwidth of the light and the resolution of the detector, these chemical shifts can be resolved.

XPS can be carried out with synchrotron radiation but also with a normal lab-based X-ray source, which makes it a very convenient technique. All XP spectra presented here were taken using synchrotron radiation.

2.3 Photoelectron Diffraction

Photoelectron diffraction is a well-known technique for probing the local atomic environment of adsorbate atoms. One of the main advantages of this technique in comparison with the well-established LEED technique (see section 2.4) is that it provides structural information without the need of long range periodicity. The purpose of this thesis is to determine the adsorption site of different adsorbates on different surfaces. In this section, it will be explained how photoelectron diffraction can solve the local structure problem.

This technique can be operated in two different modes, angle scan and scanned-energy photoelectron diffraction. All the results presented in this work have been carried out using scanned-energy photoelectron diffraction (PhD), but differences between these two techniques will also be explained in this chapter.

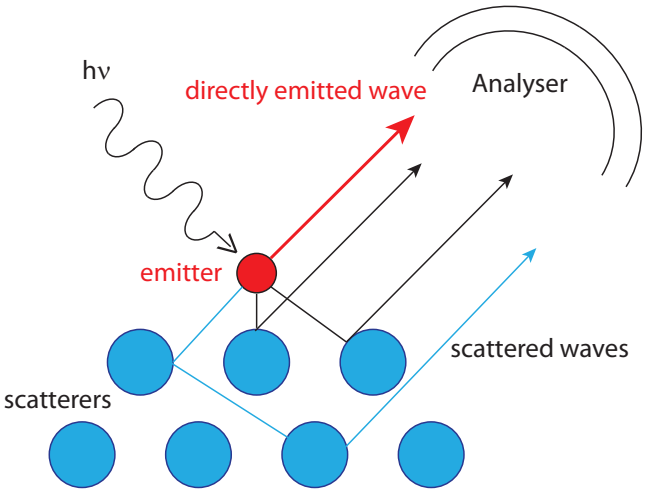

Figure 2.5: Schematic diagram representing the photoelectron diffraction technique, in the scanned-energy mode. Blue atoms depict surface atoms (scatterers) and the red atom is the adsorbate (emitter) atom. The component of the wavefield from the emitter interferes with the components of the same wavefield scattered by the surrounding atoms. The directly emitted wave is represented in red, in black are the singly-scattered waves and in blue the doubly-scattered waves.

2.3.1 Description

Photoelectron diffraction exploits the coherent interference of components of the photoelectron wavefield directly emitted from a core level of an adsorbate atom or a surface localised atom and components of the same wavefield elastically scattered by the neighbouring atoms (see Figure 2.5). The scattering interferences produce variations in the measured photoemission intensity both as a function of emission direction and photoelectron energy, due to phase differences associated with the different scattering pathways [8].

As mentioned before, there are two different modes of operation to obtain structural information: angle scan and scanned-energy photoelectron diffraction. These two different modes arise from the way the electron scattering cross-section depends on the scattering angle and photoelectron kinetic energy. Figure 2.6 shows the modulus of the atomic scattering factor as a function of the scattering angle θ for a Cu atom for several different photoelectron kinetic energies. At higher kinetic energies ($\geq$ 500 eV) this quantity is dominated by the peak appearing at θ=0°, which corresponds to forward scattering (i.e., scattering occurring in the direction of movement of the electron). The simplest case of photoelectron diffraction would

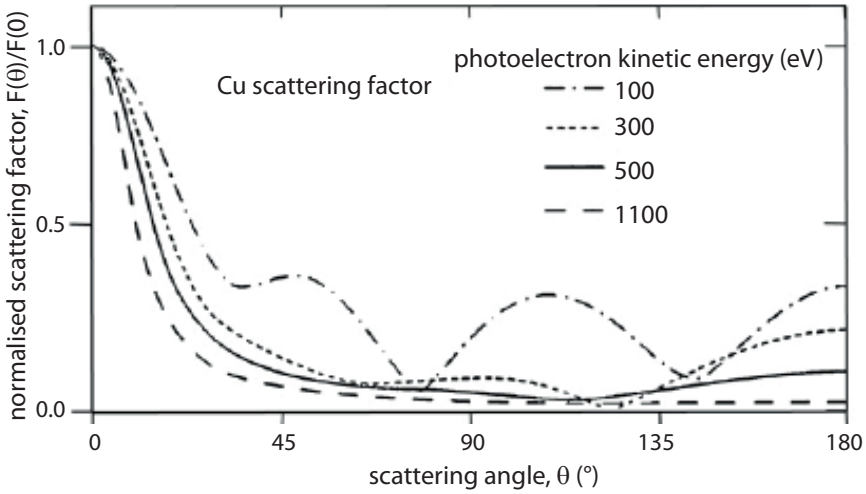

Figure 2.6: Modulus of the elastic scattering factor for electrons by a copper atom as a function of scattering angle at several different electron energies, as reported in [8]. All curves are normalised to the scattering factor at zero angle.

be to exploit the forward scattering by choosing a relative high kinetic energy.

For this procedure, the emitter atom has to lie "below" the scatterer atoms with respect to the analyser. For emission along the emitter-scatterer direction there is no pathlength difference between the directly emitted wave and the scattered one [8, 15, 16]. Therefore, they interfere constructively. However, if there was a phase shift between the two waves, the interference could be destructive. For this case, at 0° scattering angle and for high energies the phase shifts are very small and can be neglected. Hence, there is a maximum in intensity along the axis between emitter and scatterer, as shown in Figure 2.7. This diffraction, known as "zero-order", does not depend on the photoelectron wavelength and energy. When the scattering angle starts to increase, the pathlength difference is no longer zero leading to increasing destructive interference and therefore a minimum in the measured intensity. This mode of operation is known as angle scan photoelectron diffraction, or also X-ray photoelectron diffraction (XPD). The main advantage of this mode of operation is the possibility of measuring with a normal X-ray source, Mg or Al Kα with photon energies of 1253.6 and 1486.6 eV, such as those commonly used in the laboratory, providing high enough kinetic energy. XPD is also commonly used for the characterisation of epitaxial thin films.

On the other hand, this method can not provide information on the location of an atom "above" the surface. At photolectron kinetic energies lower than 500 eV, the elastic electron scattering cross-sections are reasonably large at scattering

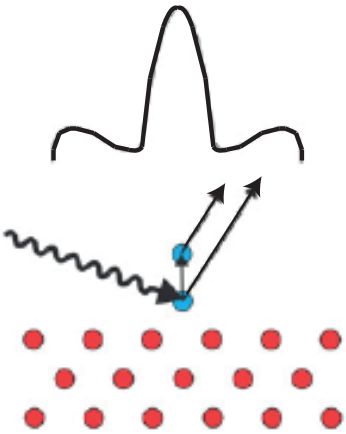

Figure 2.7: Schematic diagram showing the forward scattering photoelectron diffraction phenomenon from an adsorbate atom on a surface, taken from [8]. In the upper part of the figure, the resulting form of the photoelectron intensity as a function of the polar emission angle is depicted. The photoelectron intensity shows a peak along the intramolecular direction.

angles greater than $\approx 90^{\circ}$ (see Figure 2.6). For this backscattering geometry, the scattering paths and therefore the phase shift between emitter and scatterers depend strongly on the photon energy. Backscattering photoelectron diffraction can be resolved in angle or in energy, but is more common to perform the energy-scan mode. In this mode of operation, called scanned-energy photoelectron diffraction (PhD), the intensity of core level photoemission from an adsorbate atom is measured in a specific direction as a function of photon energy. As mentioned before, the directly-emitted wave and the backscattered waves interfere coherently. The backscattered components (by the substrate atoms) of the photoelectron wavefield follow different scattering paths which switch in and out of phase with the directly emitted wave (coming from the adsorbate atom), thus modulating the intensity. This interference behaviour depends directly on the relative position between emitter and scatterer.

In contrast to XPD, this mode of operation requires the use of a tunable X-ray source, such as synchrotron radiation.

2.3.2 Theoretical background

The simplest approach [8] to explain the scattering interference phenomenon was based on single scattering simulations. This approach included a few simplifications: first, to consider only the interference of the directly-emitted wave and the singly-scattered waves (see Figure 2.5). The second assumption is to consider the emission from an initial *s*-state. The final simplification is to treat the photoelectron wavefield

as incident plane waves.

With these three simple assumptions, the final intensity of the photoelectrons can be explained as the square of the modulus of the sum of the directly-emitted and singly-scattered components of the wavefield [8]:

$$I(\mathbf{k}) \propto |cos\theta_k + \sum_j \frac{cos\theta_r}{r_j} f_j(\theta_j, k) W(\theta_j, k) e^{(-L_j/\lambda(k))} e^{(i(kr_j(1-cos\theta_j)+\delta_j(\theta_j,k)))}|^2 \quad (2.2)$$

The first term, cos θ_k accounts for the polarisation angular dependence of the directly-emitted wave. In the same way, cos θ_r denotes the angular dependence of the polarisation at the scattering atoms located at $\mathbf{r}_j$ relative to the emitter. The summation is over the scattering atoms denoted by the suffix *j*. The next two terms account for the atomic scattering factor, f_j, as seen before (see Figure 2.6), and the Debye-Waller factor, which describes the attenuation of the modulations due to thermal vibrations. Both factors depend on the scattering angle, θ_j, and on the energy, through the modulus of wavevector, *k*. The attenuation of the intensity due to inelastic scattering is described by *exp*(-$L_j/\lambda(k)$), where L_j denotes the extra pathlength that the scattered components have to travel through the crystal with respect to the directly-emitted wave. The last term of the equation accounts for the phase in the coherent interference. The first part, r_j(*1 - cos* θ_j), describes the pathlength difference,and the second part, δ_j, is the scattering phase shift.

This expression can be simplified for scanned-energy photoelectron diffraction. An expansion of Equation 2.2 will lead to a series of terms describing the interference between the directly-emitted wave and every scattered wave and also a series of terms describing the interference between the scattered waves. These cross-terms may be assumed to average to zero, resulting in a much simpler expression, which describes the PhD modulation function, χ:

$$\chi(\mathbf{k}) \propto \sum_j \frac{cos\theta_r}{r_j} f_j(\theta_j, k) W(\theta_j, k) e^{(-L_j/\lambda(k))} cos(kr_j(1 - cos\theta_j) + \delta_j(\theta_j, k)) \quad (2.3)$$

However, although this approach is good enough for the understanding of the photoelectron diffraction phenomenology, it has been demonstrated that is not appropriate for a quantitative analysis of the data and can lead to incorrect interpretations and to the wrong final structural model [8, 24]. Two of the previous simplifications have to be revised [8]:

1. The photoelectron wavefield has to be treated as incident curved waves.

The previous plane wave description is a far-field approximation of the outgoing spherical wave from the emitter, but this is not right for near-neighbour atoms, where emitter and scatterers are only separated by ~ 2 Å.

2. Multiple scattering has to be included instead of the single-scattering approximation. This idea was already used for LEED and analysis of photoelectron diffraction experiments using this approximation provided much better results than the previous simplification.

A series of papers by Fritzsche [25–28] describes the basis of the multiple scattering code used for photoelectron diffraction in this work, based on the final state wavefunction being a sum over all scattering pathways that the electron can take from the emitter atom to the detector outside the sample. Each pathway is calculated using a magnetic quantum number expansion. Due to the large number of angular momenta necessary for the multiple scattering calculations using a wave expansion, exact calculations are rather expensive at energies above 30 eV and also very time-consuming [29]. Therefore, certain approximations have to be considered.

In a first-order perturbation theory, the electron intensity can be described as:

$$I(\mathbf{K}) = \sum_{R_0} |\psi(\mathbf{K}, \mathbf{R}_0)|^2 \approx \sum_{R_0} \sum_{m_0} |\sum_{l_0} M_{L_0}(E) B_{L_0}(\mathbf{k}, \mathbf{R}_0)|^2 \tag{2.4}$$

where $\mathbf{K}$ and $\mathbf{k}$ account for the wavevector outside and inside the crystal, respectively. The relation between the two wavevectors is determined by the refraction at the surface potential step. The summation is over all the emitter positions, $\mathbf{R}_0$, E is the kinetic energy of the emitted electrons and M_{L0} are the transition matrix elements from the initial state to the final states. The angular momenta are given by $\mathrm{L}_0 = (\ l_0\ ,\ m_0)$. The final state wavefunctions within the crystal are described by the coefficients B_{L_0}. Some approximations need to be performed due to the great complexity of these coefficients, which include all possible scattering effects of all the atoms. Thus, $\mathrm{B}_{L_0}(\mathbf{k},\ \mathbf{R}_0)$can be expanded as:

$$\begin{aligned} B_{L_0}(\mathbf{k}, \mathbf{R}_0) = e^{-i\mathbf{k}\cdot\mathbf{R}_0} A^{(0)}_{L_0}(\mathbf{k}, \mathbf{R}_0) + \sum_{\mathbf{R}_1} e^{-i\mathbf{k}\cdot\mathbf{R}_1} A^{(1)}_{L_0}(\mathbf{k}, \mathbf{R}_1, \mathbf{R}_0) \\ + \sum_{\mathbf{R}_1} \sum_{\mathbf{R}_2} e^{-i\mathbf{k}\cdot\mathbf{R}_2} A^{(2)}_{L_0}(\mathbf{k}, \mathbf{R}_2, \mathbf{R}_1, \mathbf{R}_0) + ... \end{aligned} \tag{2.5}$$

The first term of equation Equation 2.5 describes the directly-emitted wave, the second one describes the singly-scattered waves, the third one the doubly-

scattered waves and so on. All terms with $\mathbf{R}_{i+1} = \mathbf{R}_i$ from Equation 2.5 can be excluded as they account for scattering from the same atom, which is not physically possible. The terms corresponding to the final state wavefunctions are further described in a partial wave expansion as a function of spherical harmonics $\mathrm{Y}_{L_0}(\mathbf{k})$, where L_0 is the angular momentum. These expansions are described in the following equations:

$$A^{(0)}_{L_0}(\mathbf{k}, \mathbf{R}_0) = i^{-l_0} Y_{L_0}(\mathbf{k}) \tag{2.6}$$

$$A^{(1)}_{L_0}(\mathbf{k}, \mathbf{R}_1, \mathbf{R}_0) = \sum_{L_1} i^{-l_1} Y_{L_1}(\mathbf{k}) T_{l_1}(\mathbf{R}_1) G_{L_1 L_0}(\mathbf{R}_1 - \mathbf{R}_0) \tag{2.7}$$

$$\begin{aligned} A^{(2)}_{L_0}(\mathbf{k}, \mathbf{R}_2, \mathbf{R}_1, \mathbf{R}_0) = \sum_{L_1} \sum_{L_2} i^{-l_2} Y_{L_2}(\mathbf{k}) T_{l_2}(\mathbf{R}_2) \\ \times G_{L_2 L_1}(\mathbf{R}_2 - \mathbf{R}_1) T_{l_1}(\mathbf{R}_1) G_{L_1 L_0}(\mathbf{R}_1 - \mathbf{R}_0) \end{aligned} \tag{2.8}$$

The coefficients $\mathrm{T}_{l_j}(\mathbf{R}_j)$ describe the complex scattering phase shifts, δ_j, of the atom located at $\mathbf{R}_j$ relative to the emitter. These terms include also the thermal vibrations [29] and are described as:

$$T_{l_j}(\mathbf{R}_j) = i \cdot sin(\delta_l) \cdot e^{(i\delta_l)} \tag{2.9}$$

The coefficients $\mathrm{G}_{L_{i+1} L_i}$ describe the propagation of the spherical wave in an angular momentum representation:

$$G_{L_{i+1} L_i}(\mathbf{R}) = 4\pi \sum_{L_2} i^{l_0 - l_1 - l_2} h_{l_2}(kR) Y^*_{L_2}(R) \int d\Omega Y^*_{L_1} Y_L Y_{L_2} \tag{2.10}$$

where $\mathbf{R}$ is the vector between two scattering paths, and $\mathrm{h}_l(\mathrm{x})$ are the spherical Hankel functions [30].

With these approximations, the electron intensity described in Equation 2.4 becomes:

$$\begin{aligned} I(\mathbf{K}) = \sum_{R_0} |\psi(\mathbf{K}, \mathbf{R}_0)|^2 \approx \sum_{R_0} \sum_{m_0} |\sum_{l_0} M_{L_0}(E) B_{L_0}(\mathbf{k}, \mathbf{R}_0)|^2 = \\ \sum_{R_0} \sum_{m_0} |\sum_{l_0} M_{L_0}(E) \sum_{i=0}^{s} e^{-i\mathbf{k}\cdot\mathbf{R}_i} A^{(i)}_{L_0}(\mathbf{k}, \mathbf{R}_s, ...\mathbf{R}_1, \mathbf{R}_0)|^2 \end{aligned} \tag{2.11}$$

where the directly-emitted wave corresponds to i= 0, singly-scattered to i= 1, and the maximum scattering order to i= s. In this equation, the phase of the outgoing wave is described by the term $e^{-i\mathbf{k}\cdot\mathbf{r}_i}$. The final modulation function is then calculated by normalising the intensity by the non-diffractive intensity.

Vibrations

Thermal vibrations attenuate the amplitude of photoelectron diffraction modulations. This effect is caused by a "phase smearing" due to small changes in the scattering path lengths. In order to include this effect of vibrations, a Debye-Waller factor is included in the electron wavefunction, as for the case of extended X-ray absorption fine structure (EXAFS) [31]. The temperature-dependent Debye-Waller factor assumes that the individual atomic motions are uncorrelated and isotropic. It can be described as [32]:

$$W_j = exp[-k^2(1 - cos\theta_j)\langle\sigma_j^2\rangle] \tag{2.12}$$

where k is the wavenumber, θ_j is the scattering angle and $\langle {\sigma_j}^2\rangle$ describes the temperature-dependent mean-square relative displacement. This latter term is defined by [31]:

$$\langle\sigma_j^2\rangle = \langle(\mathbf{u}_0 \cdot \mathbf{r}_j^0)^2\rangle + \langle(\mathbf{u}_j \cdot \mathbf{r}_j^0)^2\rangle - 2\langle(\mathbf{u}_0 \cdot \mathbf{r}_j^0)(\mathbf{u}_j \cdot \mathbf{r}_j^0)\rangle \tag{2.13}$$

where $\mathbf{u}_0$ and $\mathbf{u}_j$ are the displacements of the emitter atom, and the j^{th} atoms, respectively, and $\mathbf{r}_j$ denotes the position of the atoms. The vibrational effects show its maximum at 180° backscattering and zero for forward scattering. The modulation attenuation due to thermal vibrations increases exponentially with the kinetic energy of the electrons [32].

2.3.3 Experimental setup

The experimental equipment used for all the experiments, except for the high-pressure methanol oxidation study (see chapter 5), consists of two different chambers, one on top of the other, separated by a gate valve, and a manipulator on top of the top chamber. A schematic diagram of the vacuum system is shown in Figure 2.8. Both chambers are connected to turbo molecular pumps backed by a rotary pump. They are also fitted with titanium sublimation pumps (TSPs). With this pumping system, it is easy to go from atmospheric pressure to ultra high vacuum. The final UHV pressure is achieved by baking the whole chamber to temperatures

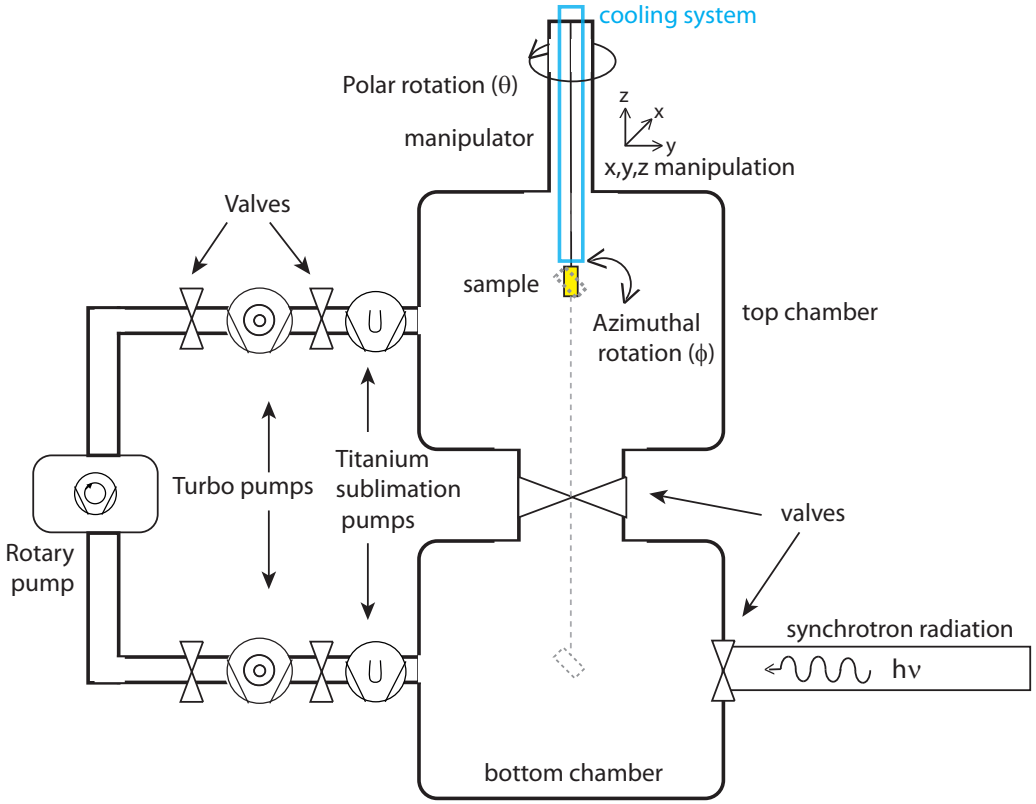

Figure 2.8: Front view of the experimental equipment. The chamber consists of two chambers on top of each other separated by a gate valve. The sample can me moved in x, y, and z, and in the polar (θ) and azimuthal angle (ϕ).

above 100 °C (120 - 180 °C). The baking takes about 20 hours, and is followed by degassing of all the filaments present (e.g., LEED, TSPs, sample holder, etc). After this, the base pressure in the chamber is about 10^{-10} mbar. The chamber is made of Mu-metal, a nickel-iron alloy with high magnetic permeability. This material is commonly used to screen the experiment from the ambient magnetic fields.

The manipulator can rotate the sample in the polar (θ) and the azimuth angle (ϕ), and move the sample in x, y and z directions. The manipulator has a liquid nitrogen reservoir which is connected to the sample holder through a copper braid, thereby cooling the sample via thermal conduction.

Figure 2.9 shows a top view of the top and the bottom chamber. The top chamber is used for the preparation of the sample. It is supplied with an ion sputter gun, used to clean the sample via ion bombardment, an ion gauge, a mass spectrometer, a few ports where evaporators can be connected and a LEED optic. The top chamber is also connected to a gas line, separated by a gate valve. In this line different gases and liquids can be attached, e.g., argon, oxygen, methanol or formic acid. All these chemicals are attached to the gas line via leak valves. Also an ion gauge is attached to the gas line to measure the partial pressure. The bottom chamber is the actual experimental chamber and therefore it is attached to the beamline. This chamber was attached to the beamline UE56-2_PGM2, at BESSY II. An external X-ray source is also attached to the bottom chamber, which makes it possible to perform some preparatory experiments when there is no access to the synchrotron radiation. An ion gauge, the pumping system and the detector, which is a commercial Omicron EA-125HR 125 mm mean radius hemispherical electrostatic analyser [33], are also attached to the bottom chamber. A schematic diagram of the analyser can be seen in Figure 2.10. The beamline and the analyser are mounted at a fixed angle of 60°. By rotating the manipulator in θ, the sample can be moved from normal incidence to normal emission (grazing incidence).

The analyser [33] consists of two concentric hemispheres with a potential difference between them. The retarding optics, shown in Figure 2.10, collect the electrons coming from the sample and focus them onto the entrance slit of the analyser. At the same time, these lenses also select the angular acceptance of the analyser and the spot size, i.e., the area of the sample that is being analysed. Finally, the electrons are retarded to match the pass energy of the analyser. This operational mode, where the pass energy is kept constant and the retarding energy is varied is called constant analyser energy (CAE). The electrostatic field created between the two hemispheres allows only electrons with the right kinetic energy (the pass energy) to enter into the detector. Electrons with higher (lower) kinetic energy

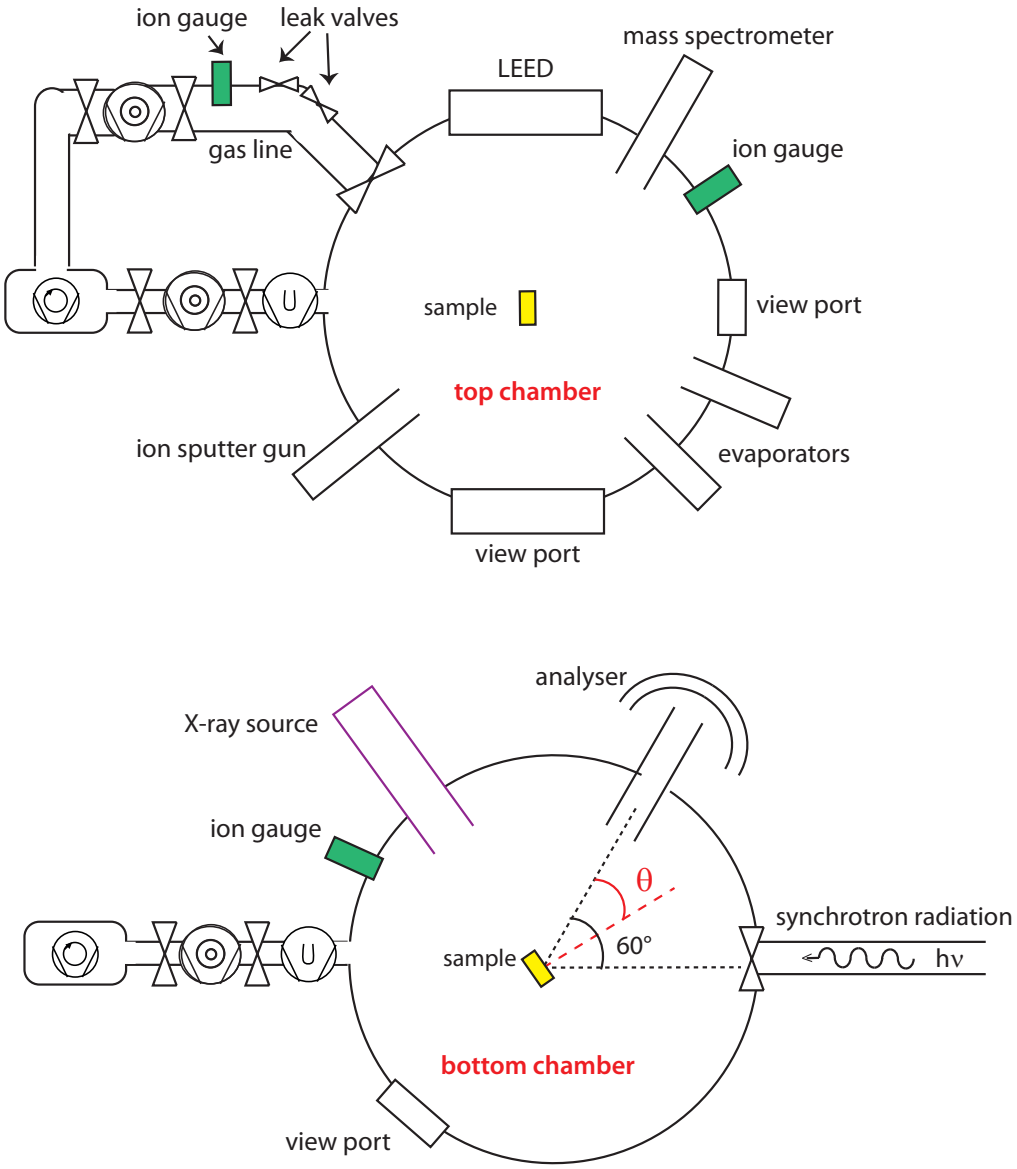

Figure 2.9: Top view of the top and the bottom chamber. The top chamber is basically used for preparation of the sample and LEED experiments, and the bottom chamber is employed for XPS (either with synchrotron radiation or with the external X-ray source), NEXAFS and PhD experiments.

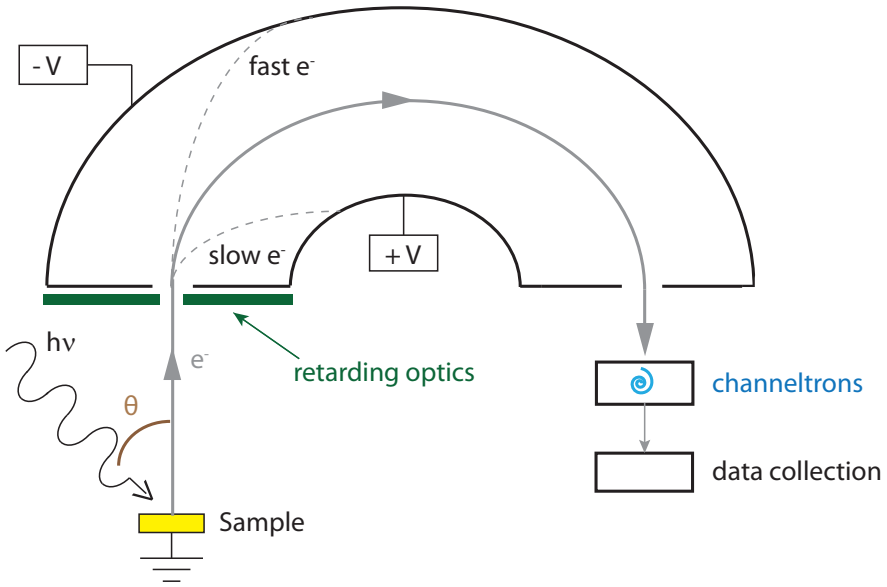

Figure 2.10: Diagram illustrating the operation of an Omicron EA-125HR 125 mm mean radius hemispherical electrostatic analyser. θ denotes the angle between the beamline and the entrance slit of the analyser.

will hit the outer (inner) hemisphere and will not contribute to the measured signal. Electrons with the right energy will reach the detector, where seven channel electron multipliers (channeltrons) are placed. Each channeltron is shifted from the position of the central channeltron and they measure spectra which are offset in energy from the true spectra by an amount proportional to the pass energy. In this way, every channeltron is getting extra information and they provide an intensity multiplied by a factor of seven. Then, the channeltrons also amplify the electron flux a factor of 10^8.

The sample is mounted on a molybdenum backplate, where it is fixed with tantalum clips. To prepare the samples it was necessary to heat them to high temperatures. Therefore, an electrical filament was placed behind the backplate, with which it was possible to reach $\sim$ 700 K via thermal radiation. In other cases, it was necessary to reach higher temperatures. For that, a high voltage was applied to the sample and this was heated by electron bombardment. The temperature was measured using an K-type thermocouple attached to the sample. This was also used to ground the sample.

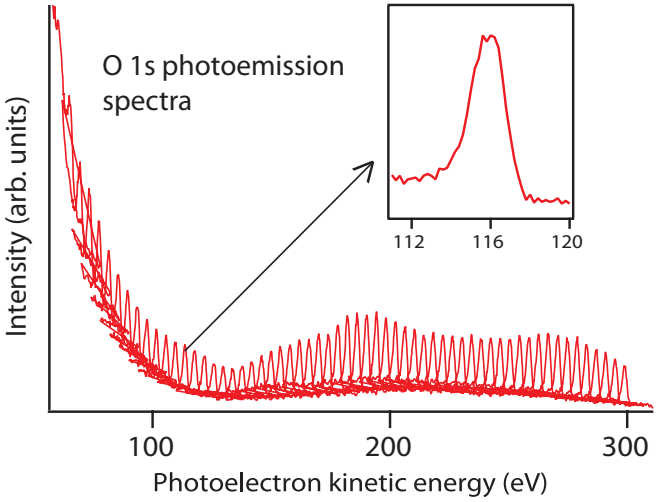

Figure 2.11: Photoelectron diffraction spectrum of an O 1s core level from HCOO on a Cu(111) surface. The photoemission intensity of O 1s is measured as a function of kinetic energy at a fixed geometry. The inset shows an individual X-ray photoelectron spectrum.

2.3.4 Data collection

One energy photoelectron diffraction scan consists of a sequence of (typically around 70) individual X-ray photoelectron spectra from a core level of an atom at a fixed geometry, with fixed energy steps of 4 eV. A typical PhD scan is shown in Figure 2.11. Each scan takes between 1.5 and 2 hours, so to verify that there is no damage, XP spectra are taken right before and after every PhD scan at the same photon energy. This process is repeated for different geometries, varying the polar angle and the azimuth angle. The more geometries are measured, the more accurate is the structure determination. The procedure to obtain the final modulation function ($\chi(E)$) from the raw data begins by normalising the measured intensities of the peaks to the beamline current, I_0, which changes with time. The next step is to create a smooth background along the whole range of energy. This is performed by taking an average value of the high kinetic energy tails of two neighbouring peaks. The high energy is chosen over the low energy tail because it is less noisy. The difference between the two values is then subtracted from the second in order to normalise it to the first one. This process is repeated along the whole range of energy of the PhD spectrum.

The next step is to fit each individual peak with a Gaussian peak, a linear background and a step with a slope. The integrated areas of these peaks provide

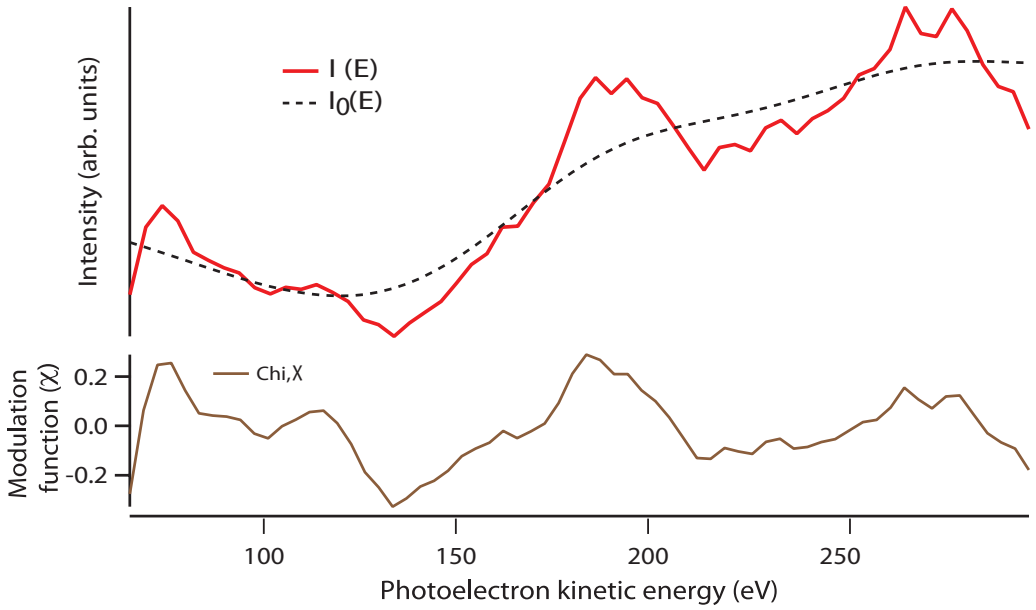

Figure 2.12: In the upper panel, the photoemission intensity is shown as a function of photoelectron kinetic energy. The red line represents the intensity, *I(E)*, and the black dashed line represents the spline, $I_0(E)$, to which the intensity is normalised to obtain the modulation function, $\chi(E)$ (brown line, lower panel). This data is obtained from the raw data shown in Figure 2.11.

the intensities as a function of photoelectron kinetic energy, *I(E)*, as shown in the upper part of Figure 2.12. In order to extract the non-diffractive effects (e.g., variations of the photoionisation cross-sections with the energy, variations of the analyser transmission and variations of the monochromator) from *I(E)*, a spline function is created, $I_0(E)$. This spline is depicted also in the upper part of Figure 2.12. The final modulation function, χ, shown in the lower part of Figure 2.12, is then calculated by subtracting this spline function from *I(E)* and normalising it with it. It is given by:

$$\chi(E) = \frac{I(E) - I_0(E)}{I_0(E)} \tag{2.14}$$

Since XPS is elemental and chemical-state specific, so is PhD. If the individual XP spectra show chemical shifts (that can be resolved), the modulation functions for these different surface species of the same element can be analysed independently and structural information can be extracted from each of them. If, on the other hand, the chemical shifts can not be resolved, the χ function will be a combination of the signal of these different species on the sample and no independent

structural information can be obtained.

2.3.5 Structure determination

The next step is to compare the experimental modulation function with multiple scattering simulations, in a way very similar to that used for quantitative low energy electron diffraction. The method is based on trial-and-error, i.e., the idea is to simulate different possible structures and compare them with the experimental data, adjusting the structure until the agreement is good. In order to quantify this comparison, we use a reliability-factor or R-factor based on that used for LEED [34].

The R-factor for scanned-energy mode photoelectron diffraction is based on the calculation of the location and size of the modulations in intensity due to the diffraction, and these are the values that are compared [35]. The R-factor is calculated from the experimental modulation function, χ_{ex}, and the modulation function obtained from multiple scattering theory, χ_{th}, as follows [8]:

$$R = \frac{\sum(\chi_{th} - \chi_{ex})^2}{\sum(\chi_{th}^2 + \chi_{ex}^2)} \tag{2.15}$$

For R = 0 the agreement between theory and experiment is perfect, whereas R = 1 corresponds to uncorrelated data. An R-factor lower than 0.3 is typically considered to be a good result for the PhD technique, although a larger value may be acceptable in some cases. Many parameters can be varied to improve the agreement between experimental data and simulations, namely the location of the adsorbate, relaxations of the surface, interatomic and intramolecular distances, vibrational amplitudes, inner potentials and scattering parameters. A visual inspection of the simulated data is very important and can also give extra information. For example, if the periodicity and the phase of experimental and simulated data are right, but the relative intensities not, the atom maybe located in the right position but the vibrational amplitudes or the inner potential will be probably wrong. This could lead to a poor R-factor.

2.3.6 Error determination

Once we have obtained a good R-factor, the final step is to determine if this is the global minimum and to establish the precision of the structural parameters that provided the best fit. The methodology used in photoelectron diffraction [36] is based on the method described by Pendry [34] for estimating errors. The first step is to simulate different structures, and for each structure i an R-factor R_i (R_1, R_2, R_3,...., R_N) is obtained. The minimum of these values is called R_{min} and its

associated structure is assumed to be the right one. The next step is to calculate the variance of R_{min}. All the structures with associated R-factors that fulfill the condition $R \leq R_{min}$ +var(R_{min}) are accepted and therefore their parameter values associated with this fit will be accepted as good. The variance of this minimum R-factor is defined as:

$$var(R_{min}) = R_{min} \cdot \sqrt{\frac{2}{N}} \tag{2.16}$$

where N is the number of independent pieces of structural information contained in the experimental data. Pendry defines N as the maximum number of peaks that could appear in the whole energy range, δE, of the LEED intensity spectra. This number is limited by the natural linewidth, which is assumed to be $4|V_{0i}|$, where V_{0i} is the inner potential. So, instead of counting the individual peaks, Pendry's approach is to divide the entire energy range by the linewidth of the peaks:

$$N = \frac{\delta E}{4|V_{0i}|} \tag{2.17}$$

In photoelectron diffraction, the intrinsic width of the peaks is limited by the inelastic mean-free-path and also by the finite angular and energy resolution of the experiment. The multiple scattering simulations [36] include some energy broadening, so the effective peak width in PhD spectra is obtained from the quadrature of the sum of the imaginary part of the inner potential (V_{0i}) and the energy broadening factor E_b, and so N is defined as:

$$N = \frac{\delta E}{4\sqrt{(V_{0i}^2 + E_b^2)}} \tag{2.18}$$

In order to estimate the errors of any parameter, a so-called line scan is performed. This line scans consist of a series of calculations where the value of the parameter is changed in fixed steps around the value which provides the best fit. By plotting the R-factor as a function of the values of the parameter whose error is being calculated, the result is usually a parabola where the vertex of the parabola is the value providing the best fit. Next, the variance is plotted on the same graph and the points where the variance intersects the parabola give the value of the error. For example, Figure 2.13 shows the estimation of the error of the height of a formate species on a Cu(110) surface. Here, the parameter whose error was estimated is the height of the oxygen atom over the surface. The best-fit is obtained for 1.86 Å, and the error in this case is symmetric and would be ± 0.03 Å.

It is important to note that sometimes the structural parameters are corre-

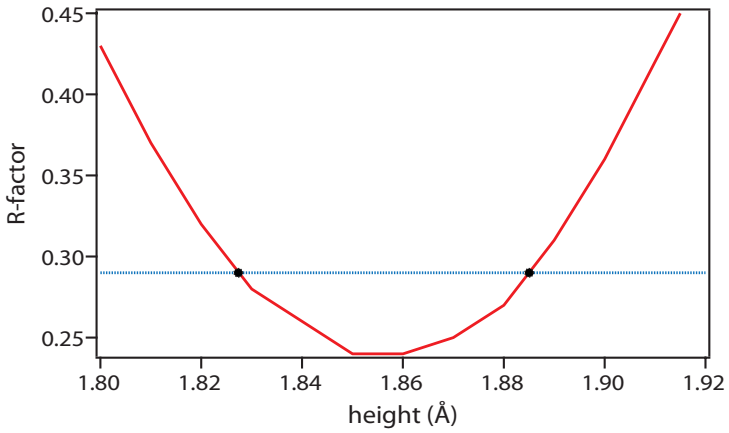

Figure 2.13: Schematic diagram of the estimation of the error of a certain parameter, in this case, the height of formate on a Cu(110) surface. The red line represents the line scan around the best-fit value. The blue line depicts the sum of R_{min} and the variance, and the black dots represent the intersection between the parabola of the line scan and the variance. The distance between the vertex of the parabola and the intersection gives the error of the parameter. In this case, the error is symmetric and is $\sim$ 0.03 Å (1.86 Å $\pm$ 0.03 Å).

lated and this methodology of error estimation could then fail; in these cases, it is necessary to change those parameters in a correlated way to compensate the variations in one of them. This can be done by determining the Hessian matrix, as it is further explained in [37].

2.4 Low energy electron diffraction

Low energy electron diffraction [13, 14] is the oldest technique for the determination of surface structures and the one with the largest number of structures resolved [38, 39]. This technique is based on elastic backscattering electron diffraction. LEED uses an external electron gun (see Figure 2.14), so unlike photoelectron diffraction, the electrons originate outside the sample and not in the sample itself. The electron beam current is typically $\sim$ 1 μA and the electron energy -V_E is in the range of 20-500 eV. Electrons in this energy range have a wavelength comparable with the interatomic distances between adsorbates and surface and therefore diffraction is possible. Thus, the electron beam is directed onto a sample that has to be electrically conducting, and is connected to earth to prevent charging. The electrons are then backscattered from the surface. These backscattered electrons have to cross a series of hemispherical grids before they reach the fluorescent screen, which is the

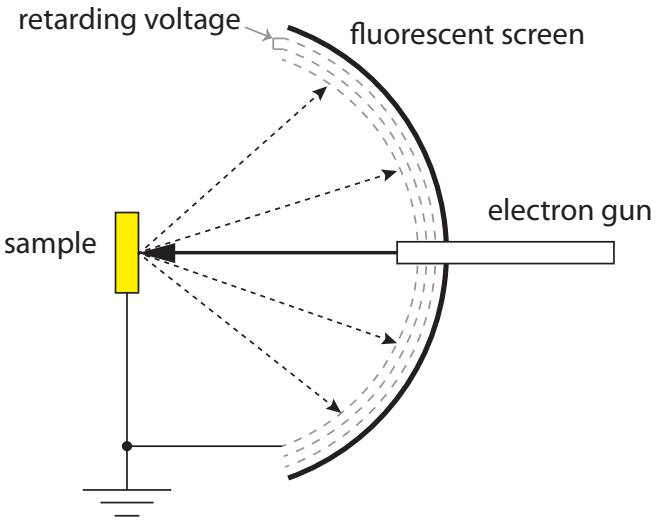

Figure 2.14: Representation of the LEED setup. The electron gun provide a current beam of ~ 1 μA and kinetic energy range 20-500 eV. The fluorescent screen is usually set at 6 kV. The retarding voltage grids are set at -V_E + Δ.

detector. The first grid is connected to earth to provide a field-free region for the electrons to travel in. The "retarding voltage" grids ensure that only the elastically backscattered electrons reach the sample. These grids are biased to a slightly lower voltage than the initial voltage (V_{grid} = -V_E + Δ). Finally, those electrons which have crossed the grids (only the elastically scattered ones) are accelerated to the fluorescent screen by setting its potential at high positive voltage ($\sim$ 6 kV). This is necessary to provide the electron with enough kinetic energy to cause light emission from the detector.

The diffraction pattern observed on the detector consists of a series of spots which are the reciprocal of the unit cell of the surface with a magnification determined by the incident electron energy. The analysis of the spot positions yields information on the size, symmetry and rotational alignment of the adsorbate unit cell with respect to the substrate unit cell. LEED can be measured in a qualitative or a quantitative way. In a qualitative way, the spots are just analysed via visual inspection of the screen. This is the mode used in this work, and it was useful in order to check the periodicity of the clean surface (to estimate the presence of possible contaminants) and also of the dosed surface (to determine the new unit cell formed by the reconstruction of the adsorbates). If the objective of the experiment is to extract structural information (e.g. interatomic bond lengths and/or the location of an adsorbate on the sample), quantitative LEED is necessary. In this case, the

intensities of the various diffracted beams are recorded as a function of the incident electron beam energy to generate the so-called I-V curves which, by comparison with theoretical curves, may provide accurate information on atomic positions.

Like photoelectron diffraction, this technique is surface sensitive. The low energy of the incident electrons ensures that they will only travel a few Å into the sample (the mean free path for these energies is $\sim$ 5 - 10 Å), and therefore all the information will come from the first atomic layers. Another characteristic of this technique, and a disadvantage in comparison to photoelectron diffraction, is the necessity of an ordered surface. This means that if the surface has no long range periodicity, no diffraction spots will be observed.

2.5 Near edge X-ray absorption fine structure

Near edge X-ray absorption fine structure (NEXAFS), also known as X-ray absorption near edge structure (XANES), is the third complementary technique used in this thesis. This technique exploits the absorption of electromagnetic radiation by excitation of core level electrons into unoccupied bound or continuum states [12]. The energy region studied with this technique ranges from slightly below to a few eV ($\approx$ 50 eV) above the absorption edge. The use of the near edge region is appropriate for the study of molecular adsorbate species, and in particular, information on the intramolecular bond lengths or bond angles can be obtained. As the photon source for NEXAFS has to be intense, monochromatic, linearly polarised, and tunable, synchrotron radiation is an ideal light source for NEXAFS. All the NEXAFS experiments presented in this thesis have been carried out in BESSY.

If a photon impinges on the surface with energy greater than the binding energy of a core level [10], this photon can be absorbed, resulting in the excitation of a photoelectron from the core level and the creation of a core hole. The annihilation of the core hole created can be filled in two different ways. The first possibility is that the core hole is filled by an electron from another energy level, causing the emission of an Auger electron, as depicted in Figure 2.15*b*. The second way is by filling the core hole with an electron of a different energy level, and emission of a fluorescent photon. The probability of these two events to occur depends on the type of atom that is probed. For atoms with atomic number $\leq$ 31, Auger electron yields are large for the K edges [10]. In this work, only light elements are probed (C, N), so the NEXAFS experiment shown here has been performed by measuring the Auger emission. A NEXAFS spectrum shows the (photon) energy dependence of the photoabsorption cross-section by measuring the Auger intensity [12].

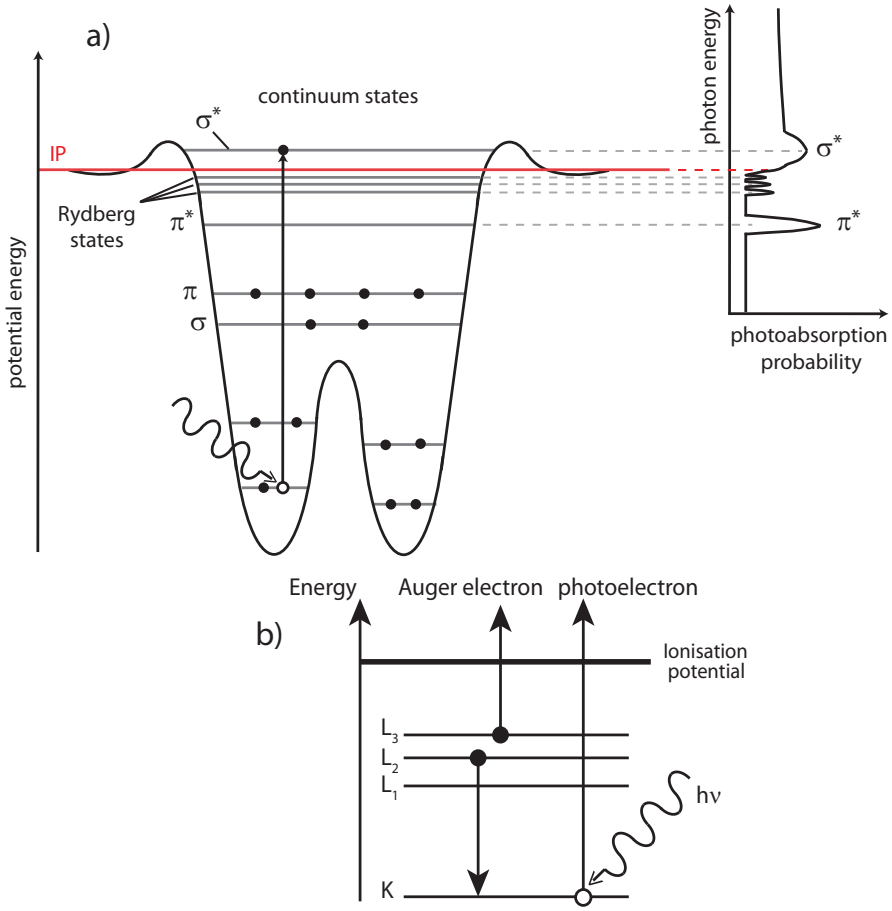

Figure 2.15: On the top, *a*, schematic diagram of the effective potential (left) and the corresponding NEXAFS K-shell spectrum (right) of a diatomic molecule adapted from [12]. On the bottom, *b*, example of the Auger process, where a photon of energy $h\nu$ impinges into a core level of an adsorbate atom and creates a hole. This hole can be annihilated via Auger emission. One electron of an outer shell can fill the hole, and in this process the electron loses energy. This energy appears as kinetic energy given to another electron from the outer shell.

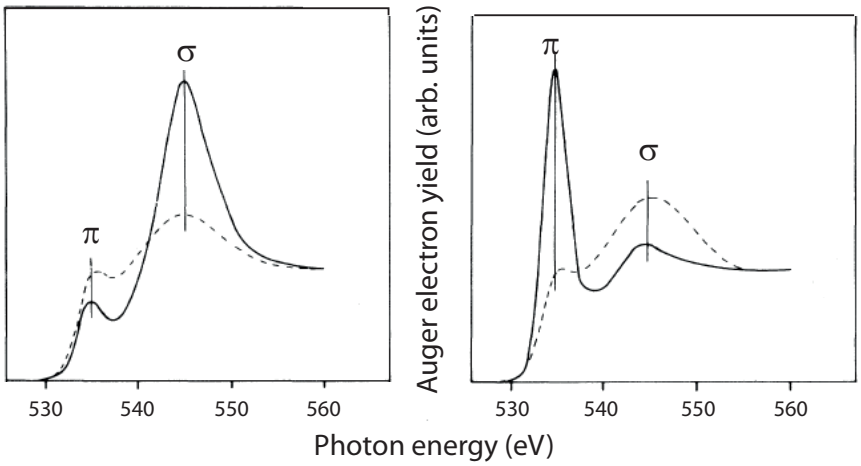

Figure 2.16: Example of O 1s NEXAFS spectra of formate on Cu(110), taken from [40]. The spectra in the left are taken in the [1 $\bar{1}$ 0] azimuth, and the ones in the right in the [0 0 1] azimuth. The full lines represents the spectra taken at normal incidence, and the dashed lines taken at grazing incidence.The features appearing at lower kinetic energy correspond to the π features and at higher kinetic energy appear the σ features.

In a molecule, the occupied and unoccupied electronic states are discrete; therefore, if the sample is irradiated with X-rays with energy slightly less than the photoionisation energy, discrete excitations to unoccupied bound states will occur [3, 9–12]. The probability for these transitions to occur depends on the incoming photon energy. If this energy is exactly the energy difference between the initial state and an unoccupied molecular state, the transition will occur. This process and the origin of the NEXAFS peaks are depicted in Figure 2.15*a* for a diatomic molecule. At energies below the ionisation threshold transitions to π^* (i.e., lowest unoccupied molecular orbital) can occur, whilst at higher energies transitions into the σ^*-orbitals can be observed. The σ^*-orbitals can be found at energies slightly above the ionisation potential (quasi-bound state) whereas the π^*-orbitals are pulled to lower energies by the electron-hole Coulomb interaction [12]. Only molecules with a π-bonding (double and triple bonds) can exhibit π-transitions. Thus, NEXAFS is very useful to obtain information on the electronic structure of an adsorbate on a surface, e.g., it is useful to check whether a double bond is still intact (see subsection 6.2.1).The width of the features depends on the lifetime of the resonances. The lifetime for the σ-resonances (transitions into σ^*-orbitals) is very small due to the large overlap of these states with the continuum. Therefore, the σ features are much broader than the π features, as can be seen in Figure 2.16. Figure 2.15*a* also

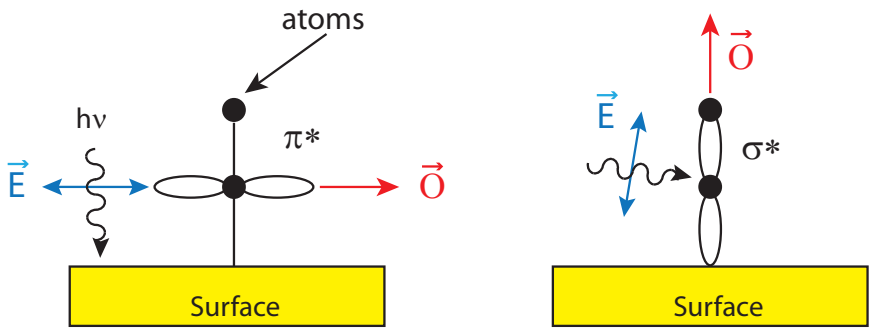

Figure 2.17: Diagram of near edge X-ray absorption fine structure based on an example of [12] for a π-bonded diatomic molecule. The molecular axis is normal to the surface. $\boldsymbol{E}$ denotes the polarisation vector of the incident light, $E_{phot}=h\cdot\nu$, and $\boldsymbol{O}$ denotes the direction of the final state orbital. In this case, the π-resonance is maximised at normal incidence (left) while at grazing incidence (right) the σ-resonance is maximised.

depicts the Rydberg orbitals. These are generally located between the ionisation potential and the highest occupied molecular orbital, π^*. The Rydberg orbitals result in sharp resonances at energies slightly below the σ-resonances, but they are usually too weak to be observed [12].

Not only electronic information can be extracted from NEXAFS, but also spatial information about the molecules can be obtained. The fact that bonds and molecular orbitals are highly directional is exploited to determine the orientation of a molecule on a surface (see Figure 2.17). The transition intensities in a NEXAFS spectrum depend on the orientation of the electric field vector $\boldsymbol{E}$ with respect to the orientation of the molecule [12]. For the case of linearly polarised light and for an initial *1s* state, the intensity of the transition is proportional to the cosine squared of δ, where δ is the angle between $\boldsymbol{E}$ and the direction of the final state orbital, $\boldsymbol{O}$:

$$I \propto |\mathbf{E}\cdot\mathbf{O}|^2 \propto cos^2\delta \tag{2.19}$$

From this equation, is easy to see that the intensity of a resonance is largest when the electric field vector is parallel to the direction of the final state molecular orbital and zero when they are perpendicular. It is important to note that the σ^*-orbitals have their maximum molecular orbital amplitude along the bonding direction and the π^*-orbitals have the maximum amplitude in the direction perpendicular to the bond axis. Therefore, by measuring two or more different geometries, for example, grazing and normal incidence, it is possible to determine the spatial

orientation of a molecule on a surface.

One problem in the NEXAFS experiment is the possibility that a photoemission peak appears in the window at the same energy as the Auger peaks, hiding any of the NEXAFS features. This can complicate the analysis of the NEXAFS spectra.

Chapter 3

The methoxy species on Cu(110)

3.1 Introduction

The objective of this experiment was to unravel the local structure of the methoxy species on Cu(110). This system was studied under ultra high vacuum conditions and, in order to get closer to more realistic conditions, it was also studied under higher pressures (see chapter 5). The importance of the methoxy species relies on its role as the main intermediate product in the synthesis of formaldehyde from the oxidation of methanol.

Methanol (CH_3OH, also abbreviated as MeOH) is the simplest alcohol and is produced naturally in the anaerobic metabolism of a few varieties of bacteria. The name methanol is the short version of methyl alcohol, and methyl comes from the Greek word "methy", meaning wine. It was isolated for the first time in the XVII century, although it had been used, mixed with other substances, already by the ancient Egyptians. It was in the 1920s when it was commercially synthesized for the first time by BASF, Germany, from synthesis gas (syngas, a gas comprising carbon monoxide, carbon dioxide and hydrogen). Methoxy refers to a methyl group bound to an oxygen atom. It forms from the dehydrogenation of methanol (CH_3O^-) (Figure 3.1).

Methanol has many industrial applications. The most important one is perhaps the synthesis of other chemicals. 40% of the total methanol production is used, for instance, to produce formaldehyde, which is the main component of many chemical products, as paints, plastics, disinfectants, biocides, etc... Another important application is using MeOH as fuel.

Figure 3.1: Scheme of the methanol (left) and methoxy (right) molecules. The red balls correspond to the oxygen, the grey to the carbon and the white to the hydrogen atoms.

There are several studies on methanol oxidation over copper surfaces [41–63]. The first studies of methanol oxidation on Cu(110) were reported at the end of the 1970s. The first study, done by Wachs and Madix [41], is the base for all the following works on this topic.

In 1978, Wachs and Madix [41] reported for the first time on the oxidation of methanol, CH_3OH and also CH_3OD, to formaldehyde (CH_2O) on a copper surface, specifically on Cu(110) by "flash decomposition spectroscopy". The goal of this work was to investigate the mechanism and kinetics of the oxidation of methanol to formaldehyde on a molecular level and to determine the function of oxygen in this catalytic reaction. The scheme suggested here for the basic steps of the formation of formaldehyde from methanol has been accepted since then:

$$CH_3OH_{(g)} \longrightarrow CH_3OH_{(a)}$$
$$CH_3OH_{(a)} + O_{(a)} \longrightarrow CH_3O_{(a)} + OH_{(a)}$$
$$CH_3OH_{(a)} + OH_{(a)} \longrightarrow CH_3O_{(a)} + H_2O_{(g)}$$
$$CH_3O_{(a)} \longrightarrow H_2CO_{(g)} + H_{(a)}$$
$$2H_{(a)} \longrightarrow H_{2(g)}$$

The first conclusion obtained by this work was that the sticking probability of methanol, dosed at 180 K, on the clean surface was almost zero. The partial oxidation of the surface enhanced the adsorption of methanol on it. The maximum formaldehyde yield was obtained for an oxygen pre-covered surface with a coverage of 0.25 ML. The second conclusion was the formation of a surface methoxy species by the interaction between deuterated methanol and surface oxygen through the hydroxyl end of the molecule; the methoxy decomposes at about 365 K, desorbing as formaldehyde and hydrogen. The methoxy species was probably formed at 180 K, when water already started to desorb. This species was the most abundant surface intermediate. Another surface intermediate was also present, although in a much

smaller amount. This intermediate, formate (HCOO), was the most stable one and decomposed above 400 K, leading to desorption of CO_2, H_2O, and H_2 at 470 K.

In 1980, Bowker and Madix [42] published the first spectroscopic study of methanol on Cu(110) using different techniques, namely ultra-violet photoemission spectroscopy and X-ray photoemission spectroscopy, and also temperature programmed reaction spectroscopy (TPRS). In this publication, it was claimed that at low temperatures the intact methanol molecule adsorbed on the clean copper sample, and dissociated at 270 K, forming the methoxy species. On the oxygen pre-covered surface, this work reproduced the results obtained by Wachs and Madix, except that in these experiments formate production was not observed.

The first vibrational-spectroscopy study was performed by Sexton et al. [43], using EELS, and also temperature programmed desorption (TPD) and UPS. As in the previous work, Sexton and coworkers found the Cu(110) surface to be relatively unreactive. They observed the formation of methoxy on the surface pre-adsorbed with oxygen at 240 K.

The first structural study of methoxy on Cu(110) was done in 1985 by Holub-Krappe et al. [44] using low energy electron diffraction and angle-resolved X-ray photoelectron diffraction (XPD). This technique, in contrast to scanned-energy photoelectron diffraction, is much more sensitive to forward scattering, leading to a broader understanding of the intramolecular structure, for instance, the bond lengths in the molecule and its orientation. In this work, methoxy was formed following the steps given by Wachs and Madix and they observed that the molecular axis of the methoxy species was not perpendicular to the surface. Due to the large difference in the data for the two azimuthal directions they claimed that the tilt of the molecule was not azimuthally isotropic. The tilt in the [1 $\overline{1}$ 0] direction reported in this work was about 18 $\pm$ 3°, and 40 $\pm$ 5° in the [001] azimuth. Based on this result and on the (4x2) LEED pattern observed, they proposed a model to explain the methoxy data, which involved two different 3-fold coordinated adsorption sites. This proposed model can be seen in Figure 3.2.

In 1994, Bowker and coworkers published a series of investigations of methoxy on Cu(110) based on scanning tuneling microscopy (STM), combined with many other techniques, namely molecular beam reaction measurements, TPD and LEED [48–50]. In the first publication [48] they found three different temperature regimes: at temperatures below 330 K the methoxy species was stable on the surface and the stoichiometry of the reaction of methanol and the pre-adsorbed oxygen was 2:1. Between 330 K and 450 K the stoichiometry was the same, but the methoxy was unstable, decomposing to formaldehyde and hydrogen. At temperatures higher than

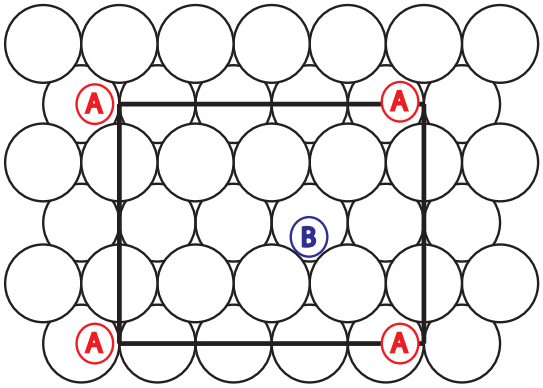

Figure 3.2: Structure model proposed by Holub-Krappe et al. [44]. The close-packed direction is the [1 $\bar{1}$ 0] and the perpendicular one is the [001] direction. This (4x2) model involves two different low-symmetry three-fold coordinated adsorption sites, A and B. Large circles represent copper atoms and the small circles represent the methoxy molecules. The molecules in A correspond to the species tilted 18° in the [1 $\bar{1}$ 0] direction and the molecule in B is tilted by 40° in the [001] direction.

450 K there is a change in the stoichiometry of the reaction. The ratio is 1:1 and there was no more hydrogen production. The second important result of this work was the observation of a (5x2) ordered phase formed by methoxy, which was seen both with STM and with LEED. In the second publication [49], the (5x2) methoxy-induced reconstruction was further explored. Sequential STM images showing the methoxy formation were taken. In these images, the reaction of methanol with the ends of the O-Cu-O-Cu added rows was observed, resulting in the formation of the (5x2) methoxy reconstruction, which incorporated Cu adatoms from the (2x1)-O reconstruction. The last paper of this series [50] pursued the study of the (5x2) methoxy reconstruction. The important report of this publication was the proposal of four different models, which would be consistent with the LEED and the STM data. These four models combined different low-symmetry adsorption sites and all of them included Cu adatoms.

Another study done by Carley et al. [51] revealed for the first time large amounts of formate on the surface at 295 K and above, coming from a different reaction pathway. This study was carried out with X-ray and electron energy loss spectroscopies, combined with many other techniques. This formate species originated from a mixed $CH_3O_{(a)}/O_{(a)}$ adlayer, which was left overnight in UHV. The mechanism of formate production from further oxidation of methoxy to its final combustion to carbon dioxide and hydrogen follows this path:

$$CH_3O_{(a)} + O_{(a)} \longrightarrow HCOO_{(a)} + H_{(a)}$$

$HCOO_{(a)} \longrightarrow CO_{2(g)} + H_{(a)}$

However, they were not able to distinguish between methoxy and formate in STM. The decrease of methoxy concentration at 295 K and the production of formate leveled off at a initial coverage of methoxy of 10 %. Not all the methoxy molecules reacted to produce formate, and the remaining methoxy molecules desorbed at 350 K. The fact that these molecules do not desorb at 295 K led them speculate that there were two different adsorption sites for methoxy, as was already proposed in previous works. A second work performed by the same group [52] also reported the production of formate at room temperature studied by TPD. In this other paper, they remarked that the formation of formate depended strongly on the reaction conditions. For example, a slow heating rate allowed the methoxy to further oxidise to formate, whilst if the heating rate was faster, the methoxy desorbed before it could be further oxidised.

Further STM work by the Bowker group studied the formation of formate via methanol oxidation [53–55]. The main difference of this study from the previous ones was the method of dosing. In this case, methanol and oxygen were co-dosed on Cu(110) at room temperature instead of a sequential dosing. The key to formate formation was the ratio between methanol and oxygen. A methanol-rich gas-phase mixture generated formate production, whilst an oxygen-rich mixture suppressed it. This happened because the excess of oxygen triggered the growth of (2x1)-O islands in the [001] direction, which were very unreactive. On the other hand, if the concentration of oxygen was lower, (highly reactive) oxygen adatoms were adsorbed on the sample, enhancing the formate production. Different ordered phases were identified on the sample: oxygen was ordered in (2x1) islands, methoxy in (5x2) islands and finally formate was identified in (2x2) islands. This last assignment was the starting point for a new series of publications of the Leibsle group [56–59]. Leibsle and coworkers disagreed with the assignment of the (2x2) islands to formate and proposed a new interpretation, namely that corresponded to a different methoxy phase. The main arguments of this work was that the formate molecules created by sequential dosing experiments were too mobile on the surface to be imaged by the STM, and also that codosing experiments of methanol and oxygen, while simultaneously using the STM, could damage the topography of the sample, resulting in an unrepresentative surface.

Sakong and Groß published a density functional theory study of the total oxidation of methanol on Cu(110) [63]. In this paper the dependence of the selectivity on the mixing ratio between methanol and oxygen is also mentioned. The most relevant part of this work to the present study is the search for the minimum-energy

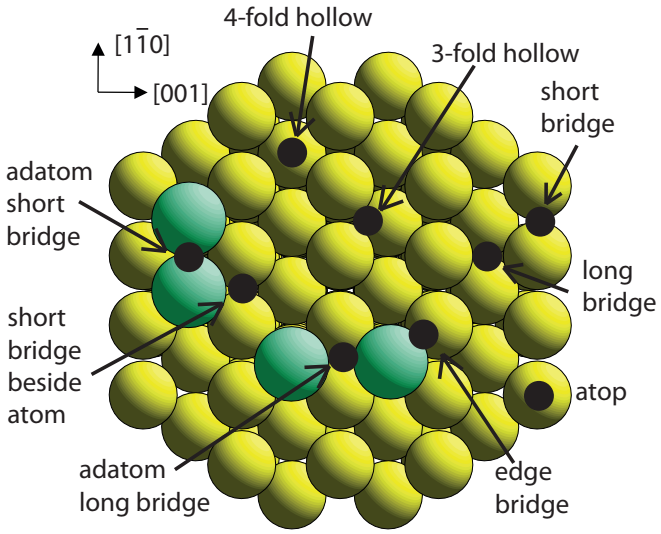

Figure 3.3: Summary of all the possible adsorption sites on a Cu(110) surface including Cu adatoms.

structure of the different (5x2) models proposed by Leibsle et al. [50], which also incorporated copper adatoms from the Cu-O chains. They found the energetically most favourable structure to be a p(5x2) model with the methoxy species (4 methoxy species per unit mesh) located at low-symmetry sites, namely, at a three-fold hollow site, at an edge site and at two long bridge sites. These adsorption sites, together with all other possible adsorption sites, are illustrated in Figure 3.3.

As can be seen in this introduction, there are many studies which tried to understand the reaction mechanism. The reaction pathway is well understood and accepted, however, there is still not a clear picture of the local structure of the reaction intermediate methoxy on Cu(110). The only attempts to unravel the adsorption site of this molecule on the surface experimentally were the XPD study [44] and the STM study [50] already mentioned here.

In the work reported here, the local structure of methoxy on Cu(110) has been experimentally studied using scanned-energy photoelectron diffraction. The use of this technique, in contrast to other techniques mentioned before such as STM and XPD, permits the determination of the surface structure in a quantitative fashion. Also the bond length between adsorbate and substrate can be determined quantitatively. STM does not provide quantitative information and XPD is mainly sensitive to the intramolecular orientations. Thus, this is the first quantitative structural study of the adsorption of methoxy on Cu(110).

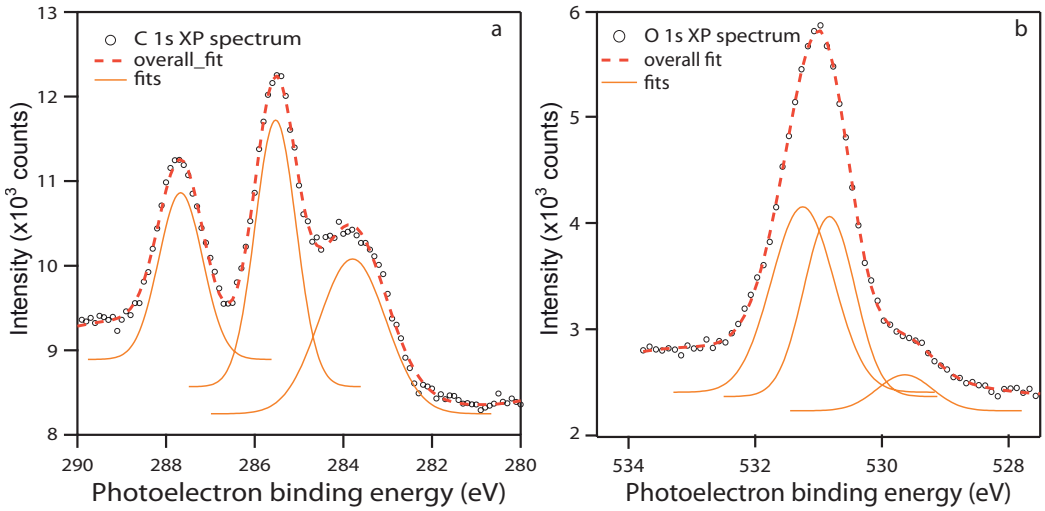

Figure 3.4: a) C 1s and b) O 1s XP spectrum of the "bad" preparation, which led to large amounts of formate.

3.2 The adsorption site of the methoxy species on Cu(110)

These experiments were carried out at the beamline UE56-2_PGM-2 (see section 2.1) at BESSY II in July and in December of 2008 and in January 2009.

The Cu(110) crystal was cleaned *in situ* by several cycles of argon sputtering and annealing. The sample was sputtered for 30 minutes in a background pressure of 1x10^{-4} mbar Ar. The acceleration voltage was 5 keV, resulting in a sample current density of $\approx 11\ \mu A/cm^2$. These ion bombardments were followed by brief annealings to $\approx$ 840 K. The cleanliness of the sample was checked by sXPS and LEED (see section 2.2 and section 2.4, respectively). LEED showed the (1x1) pattern characteristic for a clean crystal, and no contamination was observed with XPS. The azimuthal directions of the crystal were determined with the help of LEED.

The standard procedure to prepare Cu(110) with a high coverage of methoxy is, as learned from the literature, to pre-dose the sample with molecular oxygen at room temperature to a coverage of 0.25 ML. An excess of oxygen decreases the reactivity of the sample, until, at a coverage of 0.5 ML, the surface is completely covered with a (2x1)-O "added-row" reconstruction, which leads to a quite unreactive surface [41]. STM studies showed that methanol reacts with the ends of the (2x1)-O islands, specifically at the ends of the Cu-O-Cu added rows [49, 50]. After dosing oxygen, the second step is to dose methanol to react with the oxygen to produce methoxy.

However, the first attempts to prepare the surface methoxy species following

C 1s	ΔBE (eV) CH_3O - HCOO	ΔBE (eV) CH_3O - CH_x
This work	2.1	1.7
Carley [51]	2.5	
Günther [62]	2.3	1.2 - 2.5

Table 3.1: Summary of the chemical shifts between carbon-containing species on the Cu(110) surface.

this procedure failed, and resulted in significant amounts of co-adsorbed formate species. Also another carbonaceous species was found on the sample, CH_x (following the nomenclature used by Günther et al. [62]). The sXPS data from this "bad" preparation can be seen in Figure 3.4.

In the C 1s XP spectrum, three different features can be seen in Figure 3.4a (methoxy, formate, and a carbonaceous species), whereas Figure 3.4b shows two different features in the O 1s spectrum (pre-adsorbed oxygen, and a combination of the methoxy and the formate species). The peak at 285.5 eV was assigned to the methoxy species. At higher binding energies, shifted by 2.1 eV, the formate species was identified, and at lower binding energies, 1.7 eV shifted from the methoxy peak was the CH_x species. A summary of the chemical shifts between different carbon-containing species can be seen in Table 3.1. In order to be sure that the carbon-containing species at higher binding energies was formate, formic acid was dosed on the clean sample. Figure 3.5 shows the C 1s XP spectrum of formic acid dosed on a clean Cu(110) surface, which results in the adsorption of formate, and the spectrum corresponding to a "good" preparation where formate was almost completely removed from the sample. These spectra were shifted $\approx$ 1.9 eV from each other, which is similar to the chemical shift observed in the "bad" preparation between the formate and the methoxy species. The peaks in these spectra were identified following the labeling of several previous studies [42, 51, 62]. These studies agreed in the assignments of the peaks; only one other study seemed to disagree with this result, and gave quite different assignments, but it failed to explain why all the other authors' assignments were believed to be incorrect [64].

From the C 1s XP spectrum, the relative concentrations of formate and methoxy could be established. This was very helpful to constrain the fit of these two species, methoxy and formate, in the O 1s spectrum. The chemical shift between these two O 1s components was $\approx$ 0.45 eV (see Table 3.2). Extra confirmation that the peak at higher binding energies in the O 1s XP spectrum corresponded to formate was to compare the normal emission O 1s PhD spectra measured from this

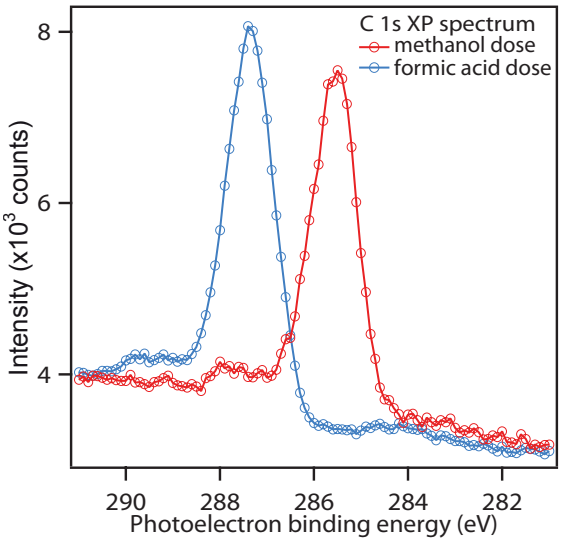

Figure 3.5: Comparison of a C 1s XP spectrum taken from a good preparation of methoxy-covered Cu(110) surface, as a result of the exposure to methanol and oxygen, and the spectrum from a formate-covered Cu(110) surface, as a result of a formic acid dosing. The red line depicts the methanol experiment and the blue line depicts the formic acid experiment. The peak corresponding to methoxy and the one corresponding to formate are separated ≈ 1.9 eV, a characteristic chemical shift for these two species.

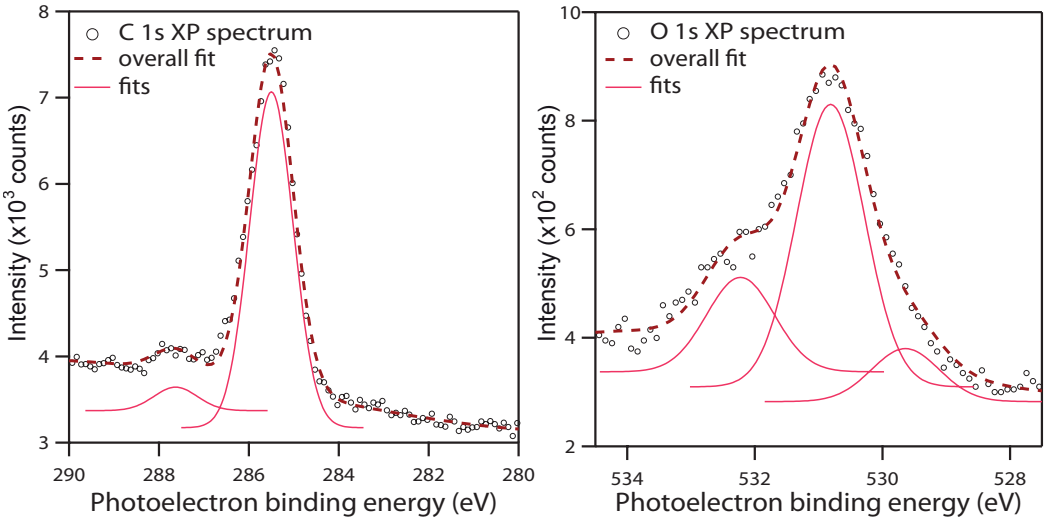

Figure 3.6: Fit of the a) C 1s and the b) O 1s XP spectra of the "good" formate-free preparation.

component with the PhD modulations found for the formate species on Cu(110) [65, 66]. This comparison showed the same PhD modulations for both experiments. It is important to mention that, due to the difficulties to identify the exact location of the Fermi level in photoemission spectra recorded at the high photon energies used here, the binding energy scales shown in Figure 3.4 and in Figure 3.6 were fixed by setting the value for the O 1s peak of atomic oxygen to be 529.6 eV, and that for the C 1s peak of adsorbed methoxy to be 285.5 eV. These values are taken from the earlier publication mentioned above [62].

As noted in Figure 3.4, the concentration of formate on the sample was very significant. This fact was surprising, since the "recipe" followed to adsorb methoxy on Cu(110) was well-proven, and only small amounts of formate had been reported previously. Further test experiments demonstrated that beam damage from the incident synchrotron radiation, combined with the temperature at which beam exposure was used, were the source of the production of formate. The tests showed that at room temperature, the incident beam induced the dissociation and desorption of methoxy. The dissociated products were CH_x and co-adsorbed atomic oxygen. This latter one reacted with the adsorbed methoxy and created formate. In order to avoid this problem, the preparation methodology was slightly modified. The oxygen procedure was carried out as mentioned before, but now the methanol dosing was done at low temperatures, taking a special care not to expose the sample to the incident beam at room temperature. Since this kind of photoinduced surface

O 1s	ΔBE O_a - CH_3O	ΔBE O_a - HCOO	ΔBE CH_3O - HCOO
This work	1.2	1.7	0.5
Bowker [42]	0.8		
Carley [51]	1.1	1.8	0.7
Günther [62]	0.6	1.4	0.8

Table 3.2: Summary of the chemical shifts between oxygen-containing species on the Cu(110) surface. The chemical shifts are given in eV.

reaction can be strongly suppressed at low temperatures, the sample was exposed to methanol at ≈ 140 K, heated to ≈ 240 K to help the reaction to occur and cooled back again to ≈ 140 K, before exposing it to the beam. The exact dosing procedure, that led to a formate-free preparation was as follows: the surface was first exposed to 1x10^{-8}mbar·150s of oxygen at room temperature, followed by a dosing of methanol of 5x10^{-8}mbar·100s at 140 K. Afterwards, the sample was heated to ≈ 240 K to remove the excess physisorbed methanol and initialize the methanol-oxygen surface reaction.

As a result of holding the sample at low temperatures during the experiments, a small amount of contamination of water from the ambient vacuum (background pressure ≈ 5x10^{-10} mbar) was always observed on the sample. In order to reduce the effect of this water contamination, the sample was briefly heated after every PhD scan to ≈ 240 K to desorb the water.

XP spectra of the formate-free preparation can be seen in Figure 3.6. In contrast to the bad preparation, now only two features can be seen in the C 1s XP spectrum. These peaks correspond to methoxy and a small amount of formate. In the O 1s XP spectrum, three different peaks can be seen: a methoxy peak at 530.8 eV, at 529.6 eV a peak corresponding to the pre-adsorbed oxygen which has not reacted with methanol, and finally at 532.2 eV a peak corresponding to a contamination of water. Table 3.2 shows a summary of the chemical shifts between the different species containing oxygen that are present on the sample.

LEED patterns from the methoxy-covered Cu(110) surface were recorded only after PhD spectra were taken, due to the problems associated to beam damage. However, no LEED pattern was then observed. This could be caused by the rapid destruction of a possible ordered structure by the LEED beam, as reported in [44, 49, 50].

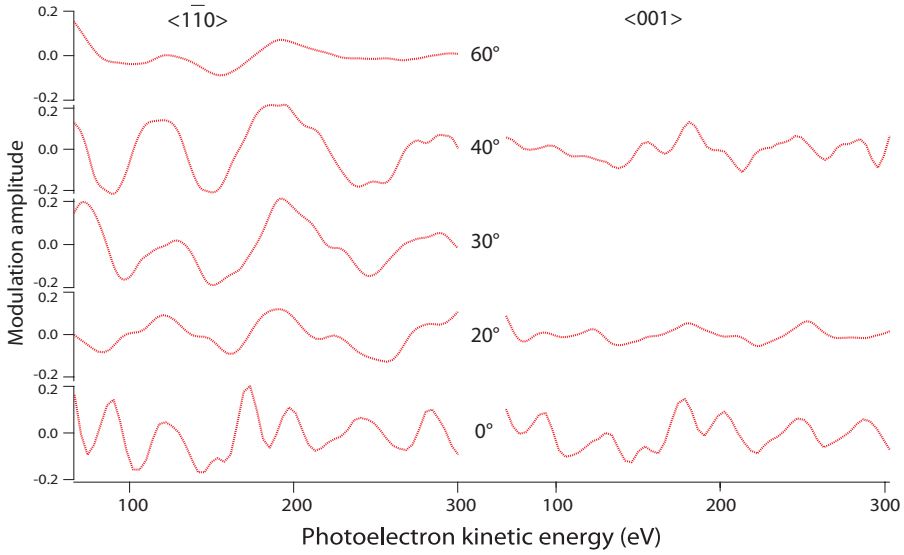

Figure 3.7: Summary of all the experimental data taken in the two different azimuths, [1$\bar{1}$0] and [001]. The spectra taken at 30° and 40° in the [1$\bar{1}$0] show the largest modulations, up to ± 20%.

3.2.1 PhD Results

Experimental O 1s PhD spectra were taken at different polar angles and in two different azimuthal directions. In the [1$\bar{1}$0] direction spectra were taken at 0°, 20°, 30°, 40° and 60°, and in the [001] azimuth they were taken at 0°, 20°, 40° and 60°. A summary of these spectra is shown in Figure 3.7. A preliminary qualitative analysis of the data showed that the largest modulations occur in the spectra of 30°, 40° in the [1$\bar{1}$0] azimuth; all other directions, especially the ones taken in the [001] azimuth showed very weak modulations. This implies that the oxygen atom of the methoxy molecule probably occupies a bridge adsorption site along the close-packed [1$\bar{1}$0] direction on the Cu(110) surface. Three data sets were chosen to pursue the analysis: the two showing the largest modulations, and also the high-symmetry normal emission direction, 0°, also recorded in the [1$\bar{1}$0] azimuth.

Multiple scattering simulations were performed for five different geometries on the unreconstructed Cu(110) surface to be compared with the experimental data. The five different geometries are: an atop site (R = 0.98); a short bridge site (R = 0.24), where the oxygen atom of the molecule is bridging two Cu atoms along [1$\bar{1}$0]; a long bridge site (R = 0.31), with the oxygen atom binding two copper atoms along the [001] direction; a three-fold hollow site (R = 1.36), next to the [1$\bar{1}$0] atomic "troughs"; and the most-symmetric four-fold hollow site (R = 0.96),

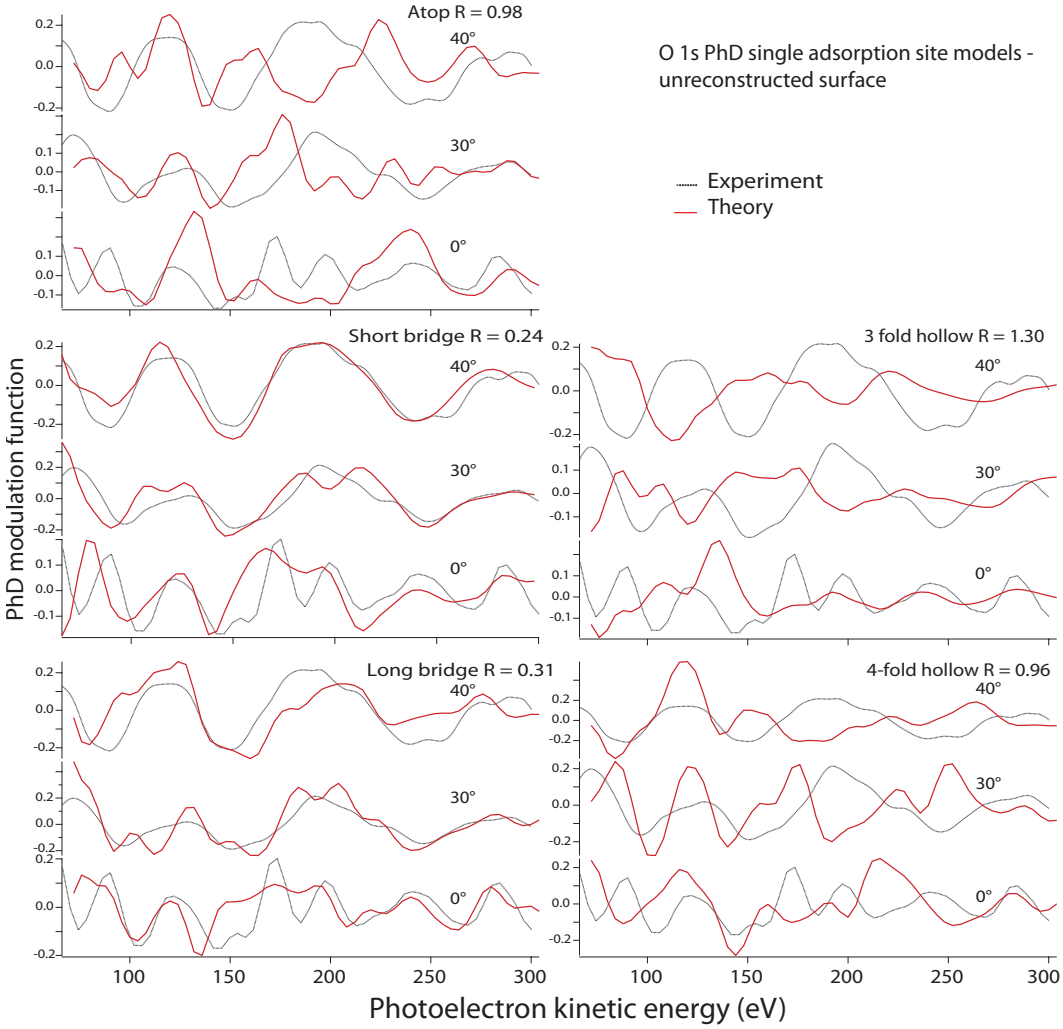

Figure 3.8: Comparison of experimental O 1s PhD spectra with theoretical simulations for five different local adsorption sites on an unreconstructed Cu(110) surface.

which is equivalent to an atop site on the second layer (see Figure 3.3). The fits to the experimental data shown in Figure 3.8 were obtained by optimising the height of the oxygen atom above the Cu surface independently for each geometry. As shown in the figure, the best fit was obtained for a short bridge site, as expected from the qualitative analysis. The R-factor for this geometry is 0.24, far better than for almost all other models. This can also be seen in the fit, where the hollow sites and the atop site failed to reproduce the experimental data. However, the R-factor obtained for a long bridge (R= 0.31) is unexpectedly low, and this corresponds to quite a good fit as can be seen in the figure. However, this good result is obtained for a structure with a very short Cu-O bond length, 1.82 Å, which is unrealistic for such a bonding (e.g. the Cu-O bonding of methoxy on Cu(111) and formate on Cu(100) and Cu(110) is ≈1.97 Å [67]). Using a more realistic value (1.97 Å) for the theoretical simulations, a much worse R-factor was obtained (R = 0.71); therefore, this adsorption site could also be excluded. The fact that the theoretical modulations (see Figure 3.8) of the long bridge site with the short bond length are so similar to the modulations for the short bridge is due to one weakness of the photoelectron diffraction technique. It is important to note that the long bridge site presented here is also a short bridge site on the second copper layer. As PhD modulations are dominated by the scattering of nearest-neighbour atoms lying behind the emitter relative to the detection direction, for angles close to the normal, the near-neighbour atoms that are close to coplanar with the emitter are almost "invisible" and contribute very little to the PhD modulations.

Therefore, in the case of the molecule in the long bridge site, the scattering coming from the copper atoms of the second layer would be stronger than the scattering from the outermost copper atoms. If the height of the molecule above the second layer in the long bridge site was similar to the height of the molecule in the short bridge above the outermost copper layer, the resulting modulation functions would be very similar. This is indeed the case for the long bridge site geometry with the short bond length. Thus the oxygen atom of the methoxy molecule in the short bridge site was found to be 1.49 Å above the outermost layer of the surface, resulting in a Cu-O bond length of 1.97 Å, and for the case of the long bridge site, the oxygen atoms are placed 1.48 Å above the second layer, resulting in a Cu-O bond length of 1.96 Å. However, this oxygen atom was only 0.20 Å above the copper atoms of the first layer, resulting in the unreasonable short nearest-neighbour bond length discussed before (1.82 Å).

One surprising fact is the poor agreement between experimental data and theoretical modulations for the three-fold hollow site. This site had been proposed

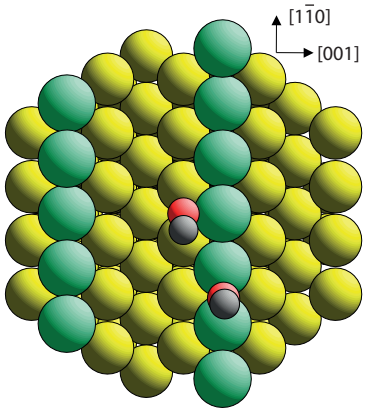

Figure 3.9: Representation of a two-site model of a methoxy-covered Cu(110) with an added row reconstruction. The yellow balls depict the Cu surface, the green ones depict the Cu added row atoms, the red ones are the oxygen atoms of the methoxy molecule and the grey balls are the carbon atoms from methoxy. One methoxy molecule is occupying a short bridge site on the added row, and the second methoxy molecule is occupying a short bridge on the underlying unreconstructed surface beside the added row. The hydrogen atoms of the methoxy molecule are not represented here, since PhD is not sensitive to them.

in previous publications as one of the possible adsorption sites, but the agreement is so poor that it can be discarded. It is also very unlikely that the methoxy molecule occupies this 3-fold hollow site, even in a model with multiple site occupation.

At this point, it was fairly clear that the methoxy molecule preferred to occupy a short bridge site. However, the agreement between experiments and theory was not yet good enough. In order to improve the fit, models with multiple site occupation were simulated, since multiple occupation was indicated in previous studies. For the two-sites models consistent also Cu adatoms, and Cu added rows have been taken into account. Cu adatoms arise from the initial (2x1)-O structure formed by the previous adsorption of atomic oxygen. According to STM studies, most of these Cu adatoms are accommodated into the methoxy surface phase instead of diffusing to surface steps [50]. First of all, new calculations for models with single sites that include these extra copper atoms were performed. The best fits were again obtained for a short bridge site on a Cu added row reconstructed surface (R = 0.23), and for a short bridge site beside a Cu added row on the first layer (R = 0.25). The added rows in these two structures were lying along the [1$\bar{1}$0] direction. The next step was to simulate two-site models, and the best fit was indeed found for a combination of the short bridge sites mentioned before (see Figure 3.9). In both cases the methoxy molecule is slightly tilted in the [1$\bar{1}$0] direction. However, as the scattering from

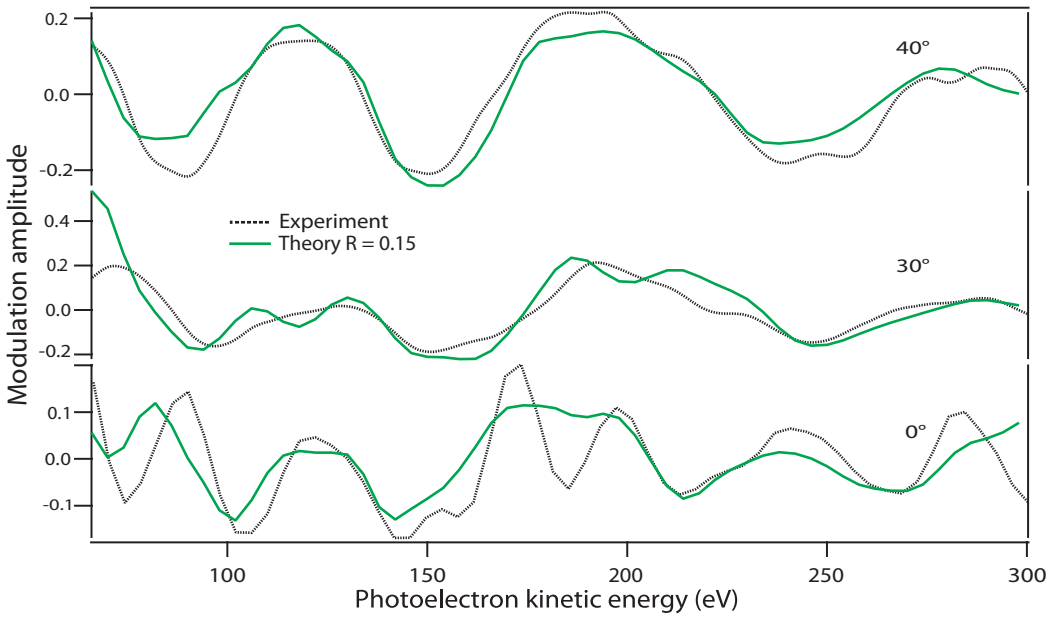

Figure 3.10: Comparison of the experimental (black) and simulated (green) PhD spectra of the best fit for methoxy on Cu(110) surface. The model simulated here is a two short bridge site, on the Cu added row reconstructed surface, as shown in Figure 3.9.

the carbon atoms is very weak, no conclusion about the exact tilt of the molecule could be obtained. The R-factor for the two short bridge site model of Figure 3.9 was 0.15. The comparison between experimental data and theoretical simulations is depicted in Figure 3.10. The individual R-factors for each angle were 0.35 for 0°, 0.13 for 30°, and 0.08 for 40°. The agreement between experiments and theory for 30° and 40° is very good, however it is still poor for the normal emission. The Cu-O bond length for the methoxy binding to the added row is 1.92 Å and the height of the oxygen atom above the copper atoms is 1.47 Å. The methoxy binding to the unreconstructed surface is 1.49 Å above the underlying copper atoms, which results in a Cu-O bond length of 1.98 Å to the atoms underneath, but a bond length of 1.82 Å to the adjacent added-row Cu atoms. Following the discussion above regarding acceptable values of the Cu-O bond lengths, this adsorption site should also be rejected. In order to get a better understanding about this, and also to try to reconcile this work with previous studies suggesting a (5x2) model, DFT calculations were performed by Matt Bradley [68, 69].

Density functional theory (DFT) calculations were performed using the Cambridge Serial Total Energy Package (CASTEP) pseudopotential plane wave code [70]. The Revised Perdew-Burke-Ernzerhof edition of the Generalized Gradient Ap-

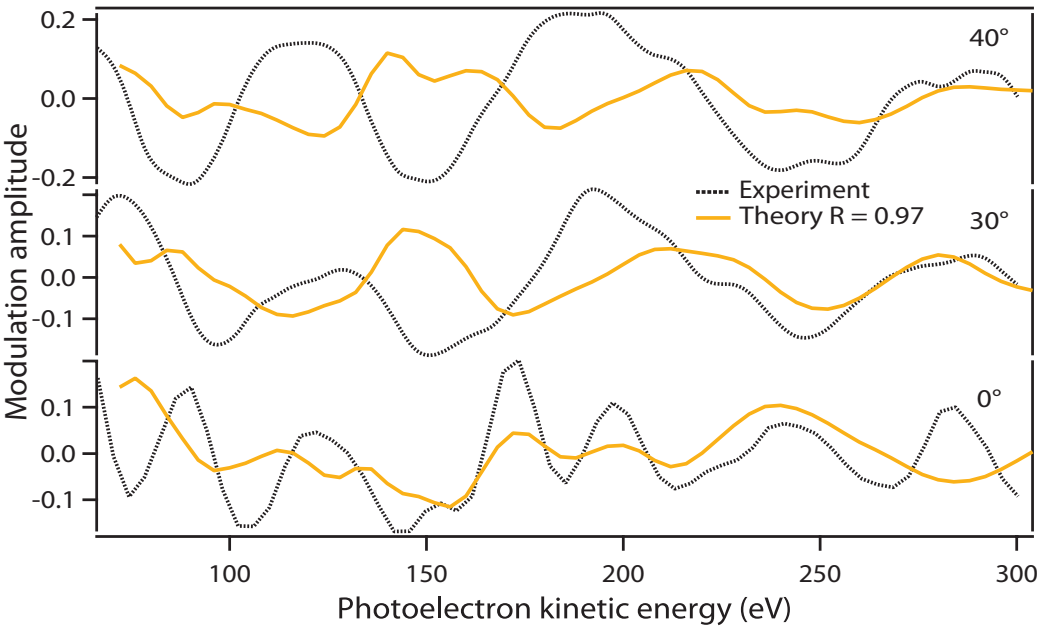

Figure 3.11: Comparison of the (5x2) model proposed in the literature with PhD simulations. The black lines are the experiments, the yellow ones are the theoretical simulations. The overall R-factor is 0.97.

proximation (GGA-RPBE) exchange-correlation functional was used, with ultrasoft pseudopotentials. A plane wave cutoff energy of 380 eV was found to provide adequate convergence. Seven-layer slabs were used to represent the Cu(110) substrate with a lateral periodicity defined by the calculated bulk Cu fcc lattice constant with a supercell height of 20 Å, sufficient to leave a vacuum gap of at least 7.5 Å in all the adsorbate phases. Initial calculations were conducted using a (2 x 2) mesh with 5 x 7 Monkhorst-Pack k-point sampling (18 inequivalent points). For structures involving a single methoxy species on an unreconstructed surface in this (2 x 2) mesh, the lowest-energy configuration corresponded to adsorption in short bridge sites with an O-C tilt in [001] of 36°. This conclusion, and the associated adsorbate geometry, are essentially identical to those of previous DFT calculations [63, 71]. Also consistent with this previous work is the result that increasing the coverage to two methoxy species per (2 x 2) mesh [in a c(2 x 2) structure] leads to a slightly more strongly-bound methoxy (by 41 meV) in the short bridge sites. One further result from the DFT study was that the $[1\bar{1}0]$ pairs of nearest-neighbours adatoms are likely to be favoured over more isolated adatoms in any model of the (5x2) structure that includes Cu adatoms. Calculations for two different (5x2) models were performed. The first model was the one previously favoured in the literature

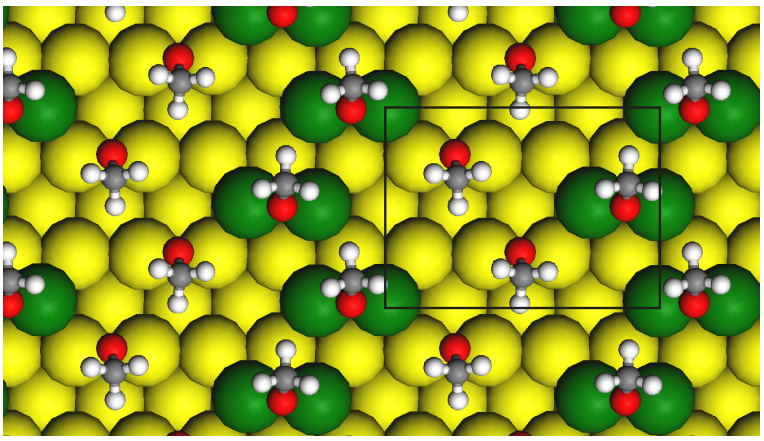

Figure 3.12: (5x2) model structure proposed by DFT. The box delimits the unit mesh, which contains 4 Cu adatoms and 4 methoxy species. The green balls are the copper adatoms, the yellow balls correspond to the underlying unreconstructed Cu surface, the red balls are the oxygen atoms, the grey ones are the carbon atoms and the white ones are the hydrogen atoms.

([50, 54, 63]), which combines 6 Cu adatoms and 4 methoxy species per unit mesh, with two methoxy species in long bridge sites, one in a three-fold hollow adjacent to the adatoms, and one in an edge bridge site. The adsorption energy per methoxy species including the adatom reconstruction was much less favourable than the short bridge site on the unreconstructed surface. PhD simulations were also performed for this model, obtaining very bad agreement with experiment (Figure 3.11).

The other models tested were a combination of short bridge sites, and short bridge sites adjacent to copper adatoms, as suggested by PhD. The most energetically favourable model was a (5x2) unit mesh containing 4 Cu adatoms and 4 methoxy molecules (Figure 3.12), two methoxys on the Cu adatoms and the other two methoxys binding to the underlying unreconstructed surface. The methoxy species are tilted in the [001] direction, in such a way that the molecules bonding to the Cu adatoms are pointing in one direction and the other two methoxy species are tilted in the opposite direction. This alternated tilt of the methoxy species creates a "zig-zag" pattern. This model structure was strongly favoured energetically over the previously proposed model. Comparisons of simulations for this "zig-zag" structure with the PhD experimental data were also performed and the structure was optimised to obtain the best fit. The best fit is shown in Figure 3.13. The resulting structure from the PhD analysis was very similar to the DFT model. The Cu-O bond length found by DFT was 1.98 Å for both adsorption sites, the same value (1.98 ± 0.03 Å) as that found for the Cu-O bond length for the methoxy species on

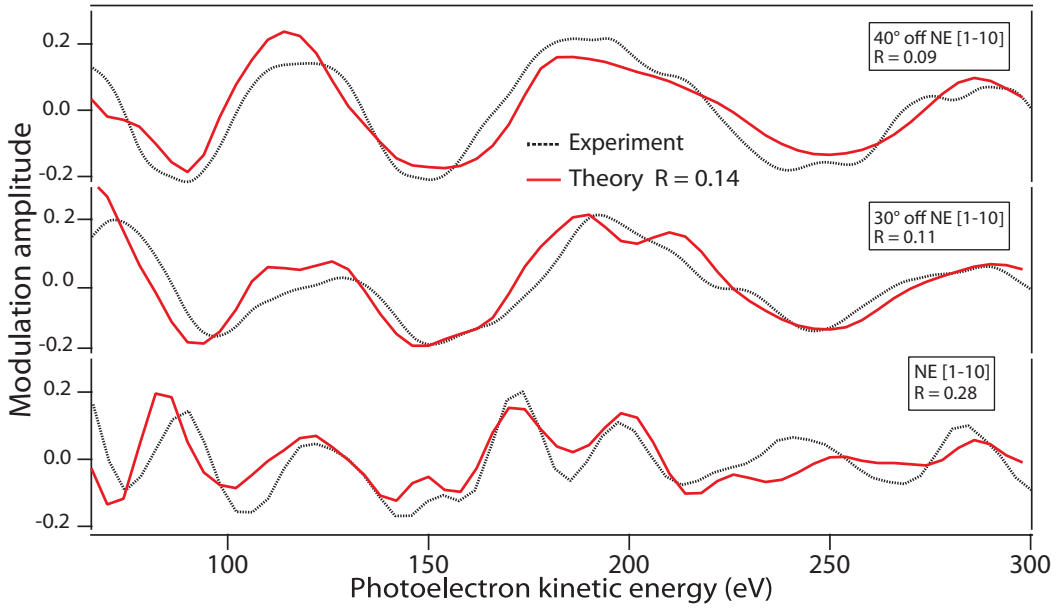

Figure 3.13: Comparison of the experimental data (black) and the theoretical simulations (red) of a methoxy-covered surface. The model simulated here is the so-called "zig-zag" structure, a (5x2) reconstruction including Cu adatoms. This model was optimised by DFT and afterwards reoptimised by PhD to find the best fit. The overall R-factor is 0.14. The individual R-factors are 0.28 for normal emission, 0.11 for 30° and 0.09 for 40°.

the copper adatoms. However, the Cu-O bond length for the methoxy species on the underlying unreconstructed surface by PhD was found to be 1.90 ± 0.03 Å. In the case of the tilt of the molecule, the value found by DFT was 36-37°, differing only slightly from the result obtained by PhD, which also favoured a tilt in the [001] direction of 33 ± 14°. This error value is relatively large due to the insensitivity of photoelectron diffraction to the rather distant carbon atom.

The overall R-factor for this structure is only slightly better than the R-factor for the two short bridge site model (0.14 vs 0.15) described before (see Figure 3.9), but by contrast to this previous model, the new (5x2) model does not involve any unreasonably short bond length. Moreover, the partial R-factor for normal emission was reduced from 0.35 to 0.28, which can be very clearly appreciated in Figure 3.13. In particular, the fine structure between 150 and 200 eV is much better reproduced than in the previous models.

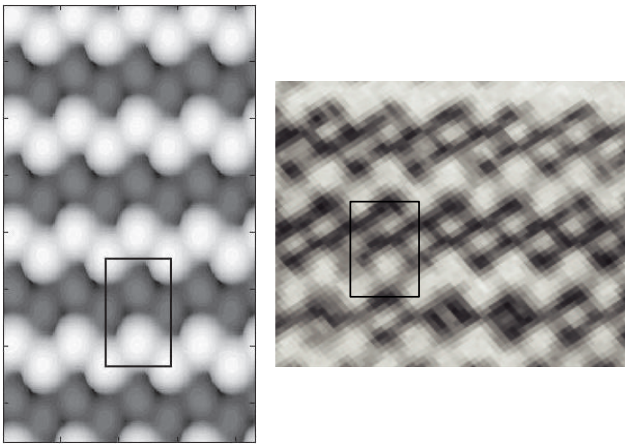

Figure 3.14: Comparison of the simulated STM image of the (5x2) methoxy-covered Cu(110) surface (left) obtained from the DFT calculations based on the (5x2) model corresponding to the "zig-zag" structure found here, with an experimental image (right, [49]). The rectangle superimposed in the image depicts a (5x2) unit mesh.

3.3 Discussion

One important issue to discuss is the possible influence of the co-adsorbed water and atomic oxygen on the copper surface, identified in the O 1s XP spectra. As mentioned above, the chemical shift between these two species and methoxy species allows us to resolve the different components, and so the O 1s component of the PhD spectra associated to the methoxy species has been analysed independently without any influence of the other two species. Nevertheless, this leaves open the possibility that the coexistence of these two species on the sample influences the adsorption site of the methoxy species. However, as is known from STM [49, 50], the unreacted co-adsorbed oxygen remains in (2x1) islands, spatially separated from the methoxy. This indicates that any remaining atomic oxygen on the sample would not influence the adsorption of the methoxy species. In the case of water, this species is easily removed by a short annealing, indicating that it is weakly adsorbed to the sample. Since the methoxy species is strongly bound to the Cu surface, it is unlikely that water influences its adsorption site. However, it is possible that the weak methoxy-water interactions influence the orientation of the methoxy species, but the O 1s PhD spectra are very insensitive to this tilt.

Another important issue is whether the structure obtained in this work is consistent with previous structural studies, by XPD and STM. Figure 3.14 compares a simulated STM image of the (5x2) phase obtained from the preferred DFT

structure and based on the Tersoff/Hamman description of STM (calculations of Matt Bradley) to an experimental image obtained from reference [49]. It is obvious that the DFT image reproduces the main features of the experimental image, in particular, the "zig-zag" row of bright protrusions coming from the methyl groups of the methoxy species on the Cu adatoms, and the darker "zig-zag" row of weaker protrusions.

Regarding the XPD study [44], two different tilts of the methoxy species were observed, as mentioned in section 3.1, and from this result a model structure involving two different O-C bond orientations was proposed. These different bond orientations implied two different adsorption sites, although another model involving a single species, tilted in the $[1\bar{1}0]$ azimuthal direction was also considered. In this work, a tilt of 33 $\pm$ 14° in the opposite directions of the [001] direction is found. This value is consistent with the value obtained by XPD of 40 $\pm$ 5°. The apparent tilt in the other direction can be explained on first order diffraction, as explained in [69].

3.3.1 Conclusions

The local structure of the methoxy species on Cu(110) has been determined using energy-scan photoelectron diffraction and density functional theory calculations (these latter ones performed by Matt Bradley). PhD found the short bridge on the unreconstructed surface and also on Cu adatoms to be the most preferred adsorption sites. DFT proposed a model based in the short bridge occupation which was a (5x2) reconstruction containing 4 Cu adatoms and 4 methoxy species. This reconstruction involved two different short bridge sites: one bonding to the Cu adatoms and one bonding to the underlying unreconstructed surface. This model structure was further fitted by photoelectron diffraction to obtain the best fit between experiment and theory. The copper-oxygen bond lengths are consistent with those of different systems. A tilt of the carbon atoms in the [001] direction was also observed . This tilt created a "zig-zag" structure, which fits with the previous STM [50] images and also with the XPD [44] study mentioned before.

Chapter 4

The formate species on Cu(110) and Cu(111)

4.1 Introduction

The goal of this experiment was to understand the dependence of the bond length between a molecule and a metal surface on the structure of the underlying metal surface. Previous studies imply that the presence of the many neighbouring metal atoms in the solid surface does not influence the bonding, and therefore that the molecular bonding is similar to organometallic bonding [72] (i.e. the bonding between a metal atom within an organic molecule in the gas phase). In order to investigate this, the chemisorption bond length of a molecule in the same local adsorption site on two different surface terminations was studied. The molecule chosen for this purpose was formate and the substrates were Cu(110) and Cu(111).

Formate ($HCOO^-$) is the simplest carboxylate anion and it is formed by the deprotonation of formic acid over copper surfaces. The importance of formate stems from its participation in many chemical reactions. It is, for example, the most stable and abundant surface intermediate product in methanol synthesis and it is also involved in the oxidative dehydrogenation of methanol [73]. Formic acid (HCOOH) is the simplest carboxylic acid. It occurs naturally and it can be found in the venom of a bee or in ant stings. Its name is due to this latter property, since formic comes from the Latin word for ant, formica. Figure 4.1 shows the molecular structure of formic acid and formate.

The structure of the surface formate species on copper has been studied since the 1980s [40, 65, 74–76]. However, although these studies seem to agree on the local adsorption site of formate, which is a bridge site along the close-packed

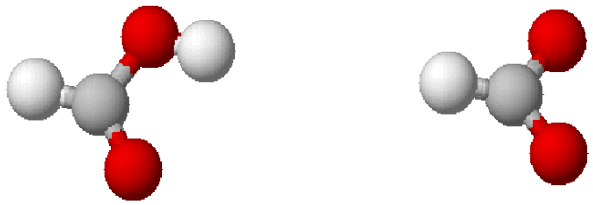

Figure 4.1: Scheme of the formic acid (left) and formate (right) molecules, where red corresponds to oxygen, grey to carbon and white to hydrogen

direction with the oxygen atoms in identical off-atop adsorption sites, there are some differences in the measured bond length between copper and oxygen.

One of the first studies was done by Stöhr et al. in 1985 [74]. Here the chemisorption of formate on Cu(100) was studied using SEXAFS, complemented by the use of NEXAFS. In this work it was claimed that the formate chemisorbs via the two oxygen atoms in adjacent fourfold hollow sites, as is shown in Figure 4.2a, with an average O-Cu nearest neighbour bond length of 2.38 ± 0.03 Å. This value is surprising if it is compared with the bond length value, for instance, of atomic oxygen on Cu(100) [77] or of O and Cu in a bulk compound [78], which are normally ≈ 0.4 Å shorter. This unusual bonding was attributed to a steric effect involving the carbon atom in a bridge position between two copper surface atoms. The non-bonding C-Cu interaction counteracts the O-Cu bond and pushes the molecule away from the surface. This leads to the unusually long O-Cu distance.

Puschmann et al., also in 1985, studied the local structure of the formate species on Cu(110) also using x-ray-absorption fine-structure techniques [40]. In this study the analysis is separated in two steps. The first one exploited the dependence of the NEXAFS intensities on the direction of the polarization vector of the incident radiation to determine the orientation of the formate species on the surface. In the second step the periodicity of the SEXAFS oscillations was used to determine the nearest-neighbour Cu-O bond length, whereas the dependence of the SEXAFS amplitude on both polar and azimuthal angles of the polarization vector allows the directions of these neighbours to be determined. The results showed that the formate species lies with its molecular plane perpendicular to the surface, aligned along the [1 $\bar{1}$ 0] azimuth direction. The adsorption of the molecule was concluded to occupy an atop site on the copper atoms of the outermost layer, with the oxygen atoms close to bridge sites, as is shown in Figure 4.2b. For this adsorption site the bond length between oxygen and copper was found to be 1.98 ± 0.07 Å, a value

Substrate	Adsorbate	Technique	Cu - O bond length (Å)
Cu(100)	Formate	SEXAFS	1.99 ± 0.10 [74, 75]
	Formate	PhD*	1.98 ± 0.04 [65]
Cu(110)	Formate	SEXAFS	1.94 ± 0.10 [40, 75]
	Formate	PhD*	1.98 ± 0.04 [65]
	Acetate	PhD	1.91 ± 0.04 [79]
	Benzoate	PhD	1.91 ± 0.02 [80]
Cu(111)	Formate	NIXSW	1.92 ± 0.04** [76]
	Acetate	NIXSW	1.86 ± 0.04** [81]

Table 4.1: Summary of previous determinations of the Cu-O bond length for carboxylate species on Cu surfaces. PhD* indicates that these studies used a simplified theoretical modeling that may involve some systematic error. NIXSW does not measure the bond length directly and these ** values rely on certain assumptions about the surface relaxation.

almost identical to that in bulk copper formate [78]. This adsorption site differs significantly from the one proposed by Stöhr.

One year later Crapper et al. [75] did a reanalysis of the previous SEXAFS studies using a multishell simulation procedure on Cu(100) and also on Cu(110). The results obtained in this report led to the interpretation that the previous results were incorrect. They found for both surfaces an adsorption site with the formate atop a copper atom, although the orientation was different for both surfaces. For Cu(110) the best fit was obtained for the molecule oriented along the [1 $\bar{1}$ 0] azimuth

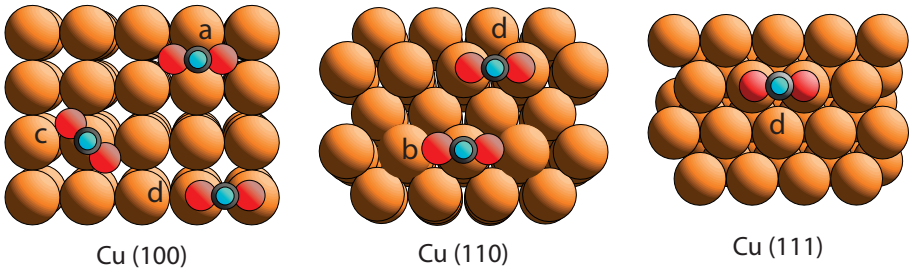

Figure 4.2: Summary of all the proposed adsorption sites for formate on the three low-index copper surfaces, where "a" represents a bridge site with the oxygen atoms in four-fold hollow sites, "b" represent an atop site with the oxygen atoms in bridge sites, "c" represents an atop diagonal site and "d" represents a short bridge site.

direction, as reported in [40] (Figure 4.2b) , with a Cu-O bond length of 1.94 ± 0.10 Å. On the other hand, the formate molecule was concluded to be bound on the Cu(100) in the so-called "diagonal atop" site, as is shown in Figure 4.2c. The Cu-O bond length for this surface was 1.99 ± 0.10 Å. The differences between this work and the previous studies were explained as a consequence of the mismatch of the Cu-Cu nearest neighbour distance (2.55 Å) and also the mismatch of the O-O distance in formate which is ∼ 2.20 Å. It was shown that in the O K-edge SEXAFS, when the measurements were taken at normal incidence, the modulations coming from the backscattering by Cu substrate atoms were very similar in amplitude and periodicity to the modulations coming from the backscattering O atoms. This would lead to misleading interpretations of the adsorption sites and the bond lengths.

Nevertheless, in 1988, a new publication for formate on Cu(100) and Cu(110) proved all the previous results to be wrong [65]. Woodruff et al. used photoelectron diffraction in energy-scan mode to obtain a quantitative analysis of the adsorption site and near-neighbour distances. The PhD modulations of formate on Cu(100) and Cu(110) were very similar, indicating the same adsorption site for formate on both surfaces. This result is inconsistent with the two different sites proposed before. PhD data revealed the adsorption site of the formate to be a bridge site along the close-packed direction, with the oxygen atoms lying in identical off-atop sites (see Figure 4.2d). The calculations showed that the Cu-O nearest neighbour distance was 1.98 ± 0.04 Å, similar to the value obtained by Puschmann. One of the reasons given to explain the disagreement with the other publications was the sensitivity of the techniques. While SEXAFS is more sensitive to the nearest-neighbour bond length, PhD is sensitive to both the bond length and the adsorption site. These two have to be determined simultaneously. For this reason the PhD technique is expected to be more incisive than SEXAFS in this case. Another complication is the similarity between the O-O distance and the Cu-Cu, already explained above.

The first structural study of formate on Cu(111) was done more than ten years later, in 2000, by Satiropoulos and coworkers [76]. The local structure of formate on this surface was determined using normal incidence X-ray standing wavefield absorption (NIXSW). The goal of this work was to use this technique to determine the local registry of simple organic molecules. This method had been used traditionally to study the adsorption of heavier elements. The disadvantage of the technique is the high energy of X-rays that comprise the standing wavefields, which are typically between 2 and 3 keV for transition metals. At these energies, the cross-sections for photoemission from light elements are very small. Using a second-generation storage ring this problem could be solved. The results showed that the

adsorption site of formate on Cu(111) is identical to that found on both Cu(100) and Cu(110) (see Figure 4.2d), the formate binding in a bridge site along the close-packed direction with the oxygen atoms almost in atop sites. This similarity with the previous published results implies that this technique using a second-generation storage ring succeeds in determining the local registry of oxygen. However, it was not possible to collect data from the carbon, in order to get further insight into the intramolecular distances. The oxygen-(111) plane separation determined in this work was 1.89 Å. It was found that the oxygen atoms could be statically displaced from exact atop sites by up to 0.33 Å in the direction parallel to the surface, leading to a Cu-O bond length of up to 1.92 Å.

Although there are many studies of formate on copper surfaces and all seem to agree about the local adsorption site (see Table 4.1), it is difficult to extract any meaningful information about the dependence of the bond lengths on the underlying metal substrate. In all cases the Cu-O bond length is found to be in the range between 1.91 Å and 1.99 Å, very similar to the values in Cu_2 formate complexes in which formate species bridge the two Cu atoms (e.g. 1.98 Å [82] and 1.96 Å [83]). However, these different surface measurements were carried out with different experimental methods and under different conditions. Hence, it is impossible to derive a reliable conclusion regarding any possible face-dependence of these bond lengths. In order to obtain a better understanding of the behaviour of this metal-atom/molecule bonding, a new study of two of the low-symmetry copper surfaces is presented here. In this work, both systems were measured with the same technique and under almost identical conditions.

4.2 Formate on Cu(110)

This experiment was carried out at the beamline UE56-2_PGM-2 (see section 2.1) at BESSY II in 2009 and in 2010.

The copper sample was cleaned by carrying out a few argon sputtering and annealing cycles. The Cu(110) surface was sputtered for 30 minutes in a background pressure of 1x10^{-4} mbar Ar. The acceleration voltage was 5 keV, resulting in a sample current density of $\approx$ 5 μA/cm^2 . The sample was then heated to $\approx$ 900 K for 2 - 3 minutes. To check the cleanliness of the sample XPS and LEED were performed. After the cleaning cycles a sharp (1x1) LEED pattern was observed, and no contaminants were observed with XPS. The azimuthal directions of the crystal were determined with the help of LEED.

Prior to the dosing, the sample was cooled down to $\approx$ 140 K. Previous dosings

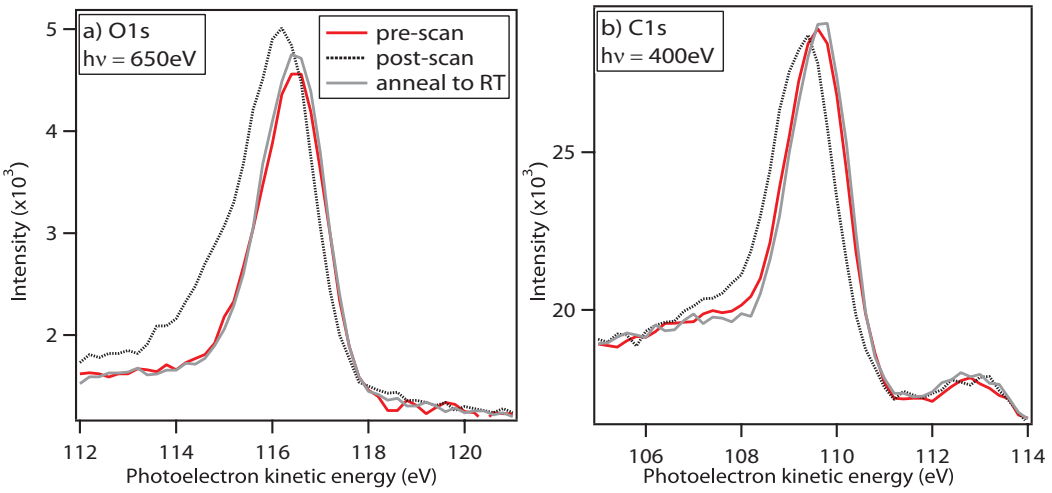

Figure 4.3: O 1s a) and C 1s b) XP spectra of the dosed sample (red), after PhD scan (black) and after annealing (grey). This spectra are taken at 140 K. An extra feature shifted 1.2 eV from the main peak towards higher binding energies appears after the PhD scan. This new peak corresponds to a small contamination of water and formic acid. These spectra are taken at 20° of polar angle.

at room temperature (carried out in February 2009) had been performed, but the PhD data obtained from these measurements showed very weak modulations. To overcome this problem, in January of 2010 the measurements were repeated at low temperatures. All the data shown here were taken during this last beamtime. The sample was not only held at $\approx$ 140 K during the dosing, but also during the measurements. Formate was dosed by filling the chamber with a pressure of $5\text{x}10^{-8}$ mbar of formic acid for 100 seconds, corresponding to a dose of 5L. Formic acid was obtained from FLUKA (purity of 98%). It was prepared by freeze-pump-thaw cycles to improve its purity. In contact with copper surfaces formic acid dehydrogenates and adsorbs on the sample as formate. No LEED pattern was observed after the dosing, indicating that the formate did not arrange with long-range periodicity.

XPS measurements were also taken after the dosing to characterise the sample. Figure 4.3 shows the O 1s (a) and the C 1s (b) spectra. These spectra were taken at a polar emission angle of 20° in the [1 $\bar{1}$ 0] azimuth direction. The photon energy used to take the O 1s spectrum was hν = 650 eV . The photon energy used to take the C 1s spectrum was hν = 400 eV . In both graphs there are three XP spectra depicted, corresponding to the spectrum immediately after the dosing and before the PhD scan (red), a spectrum taken after the PhD scan (black), and finally a spectrum taken after heating the sample to room temperature (grey) after the

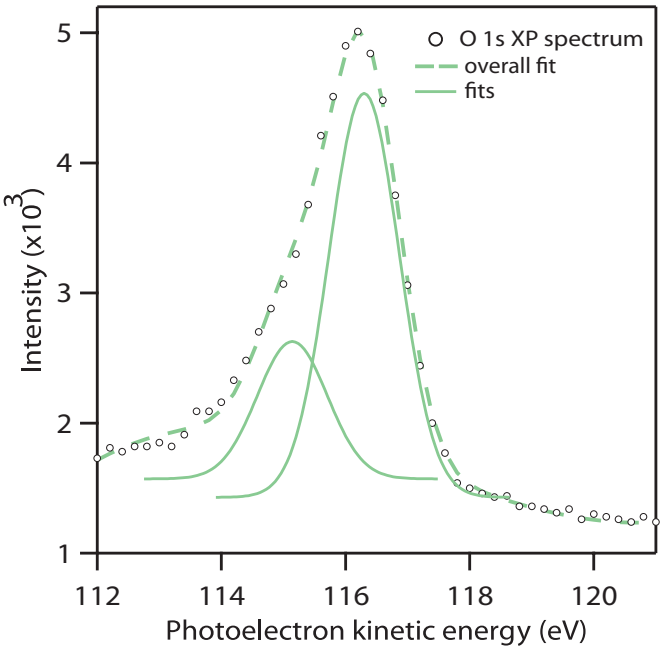

Figure 4.4: Fit of the O 1s XP spectrum taken immediately after the PhD scan. The peak at 116.4 eV corresponds to formate, whereas the peak at 115.2 eV is associated with a contamination by water and formic acid.

PhD scan.

One of the problems of dosing formate at low temperatures was the risk of adsorbing the intact formic acid molecule on the copper sample instead of creating formate. To avoid this problem, the sample was briefly heated to room temperature after every dosing. A second problem was the adsorption of background water on the sample, as we could see in the XP spectrum (Figure 4.4). Also to get rid of this water contamination a brief heating to room temperature was performed after every PhD scan. During these short annealings an increase of the water background pressure in the chamber was observed with the mass spectrometer, attributed to desorption of water from the sample and the sample holder.

In the O 1s spectrum taken before the PhD scan only one oxygen-containing species can be observed. The fact that there is no chemical shift between the two oxygen atoms of the formate molecule implies that both oxygen atoms have the same or very similar chemical environments, suggesting that they occupy equivalent adsorption sites. In the spectrum taken after the PhD scan, however, there is an extra peak shifted 1.2 eV towards lower kinetic energies. In Figure 4.4 the fit of these two peaks is shown. This second peak was increased gradually with time.

A similar effect was observed in the C 1s spectrum. The main peak (E_k = 116.4 eV in the O 1s spectrum and E_k = 109.4 eV in the C 1s spectrum) was assigned to formate. The adsorption of water on the sample due to the low temperatures would explain the peak at lower kinetic energy in the O 1s XP spectrum. However it can not explain the feature observed at lower kinetic energy in the C 1s spectrum. Adsorption of intact formic acid from the background or the sample holder could create an overlayer and would explain the C 1s peak at 109.4 eV. Annealing the sample briefly to room temperature was necessary to remove the excess of formic acid and water, as is shown in the spectra. This process was performed regularly.

These two peaks in the O 1s spectrum can easily be resolved, and therefore, the PhD modulation spectrum corresponding to the formate species alone can easily be extracted.

4.2.1 PhD Results

Experimental O 1s PhD spectra were obtained at polar angles of 0° (normal emission), 10°, 20° and 60° in the [1$\bar{1}$0] azimuthal direction and 0°, 10° and 20° in the [001] direction. Most of those spectra were repeated for different preparations. Also a few scans were taken at room temperature. As mentioned before, the modulations were significant weaker than at low temperature. In particular, the PhD scan taken at grazing angle, 60°, showed no modulation at all. This and the fact that the scans taken at normal emission, 0°, showed the largest modulations, suggest that the oxygen atoms of the formate sit atop the copper atoms, or very close to atop, so many other local adsorption sites could already be rejected. Only three of the PhD scans were chosen to pursue the analysis, 0°, 10° and 20° in the [1 $\bar{1}$ 0]. These three scans were chosen because they showed the largest modulations. Also, the choice of only three spectra reduces the computational time required for the analysis. These data sets were processed following our general PhD methodology, as described in subsection 2.3.4. PhD spectra were simulated for different local structures, namely the atop site, the short bridge site (along the [1 $\bar{1}$ 0] azimuthal direction) and the long bridge site (bridge along the [001] azimuthal direction), and these were compared with the experimental data.

Figure 4.5 shows the comparison between the experimental spectra and multiple scattering simulations for a short bridge site. The χ(E) functions observed in the figure show modulations weaker than 20%. These rather small modulations made the analysis of the PhD data difficult, since it is difficult to distinguish between noise and real structure. Also, differences in the relative intensities between the experimental curves and the simulated curves for these weak modulations can

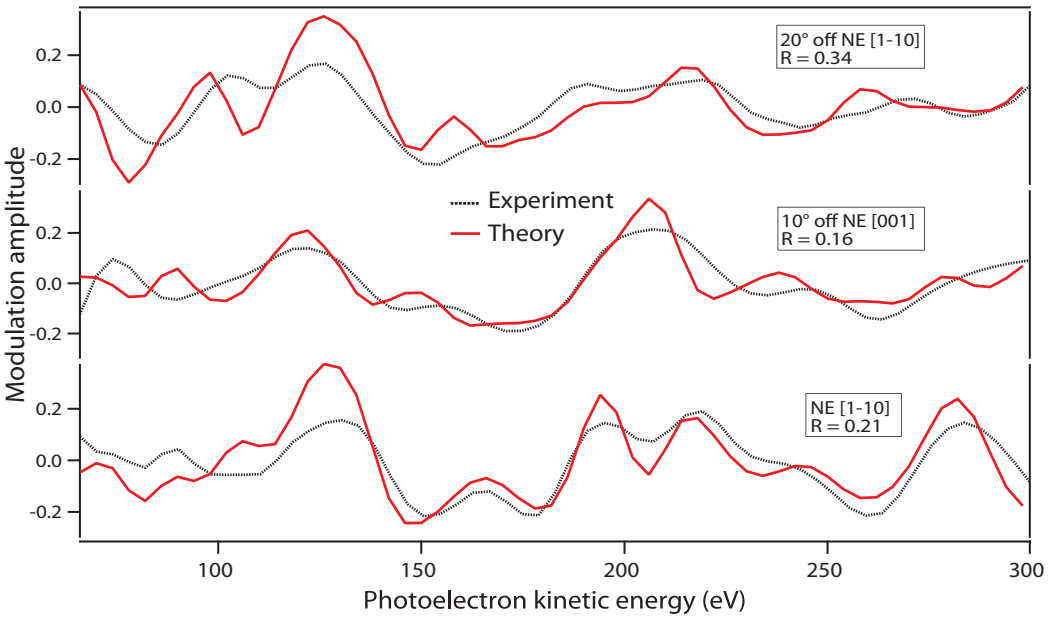

Figure 4.5: Comparison of the experimental (black) and simulated (red) PhD spectra of the best fit for formate on Cu(110). The simulation curves are for a short bridge site along the [1 $\bar{1}$ 0] with the oxygen atoms sitting off-atop the copper atoms.

lead to a poor R-factor, even if the simulations reproduce all the main features of the χ functions. The best agreement was obtained for the formate molecule sitting on a short bridge site along the [1 $\bar{1}$ 0] direction with the oxygen atoms slightly off atop the copper atoms. The partial R-factors for individual spectra are 0.21 for normal emission, 0.16 for 10° and 0.34 for 20°, as shown in Figure 4.5. The overall R-factor is 0.23. The variance of this value is 0.05, therefore all structures with R-factor greater than 0.28 (0.23+0.05) can be dismissed. This fit was obtained for a copper-oxygen bond length of 1.90 ± 0.03 Å. The oxygen atoms are sitting in equivalent symmetrical sites. The oxygen carbon bond length obtained was 1.44 (-0.9/+1.4) Å and the bond length between oxygens was 2.35 (-0.16/+0.11) Å. This structure is shown in Figure 4.6. In this figure the hydrogen atom of the formate molecule is not represented, as PhD is not sensitive to its position. The molecule is standing up, with the molecular plane perpendicular to the surface.

Figure 4.7 shows the comparison between the experimental spectra and the result of the multiple-scattering simulations for atop position and long bridge sites. On the left side, the simulations are for formate on top of a copper atom with the oxygen atoms occupying short bridge sites (blue lines). The experimental curves are represented in black. There are a few similarities between experiments and

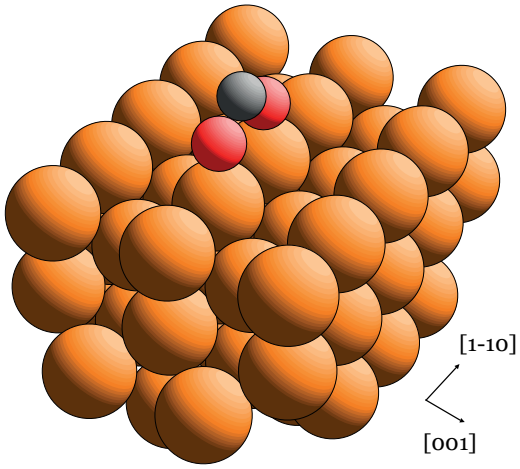

Figure 4.6: Representation of a formate molecule bonding to the Cu(110) surface in a short bridge site along the [1 $\bar{1}$ 0] direction. The orange balls represent the copper atoms, the red ones represent the oxygens and the grey one represents the carbon atom. The hydrogen atom of the molecule is not represented since the PhD technique is not sensitive to it.

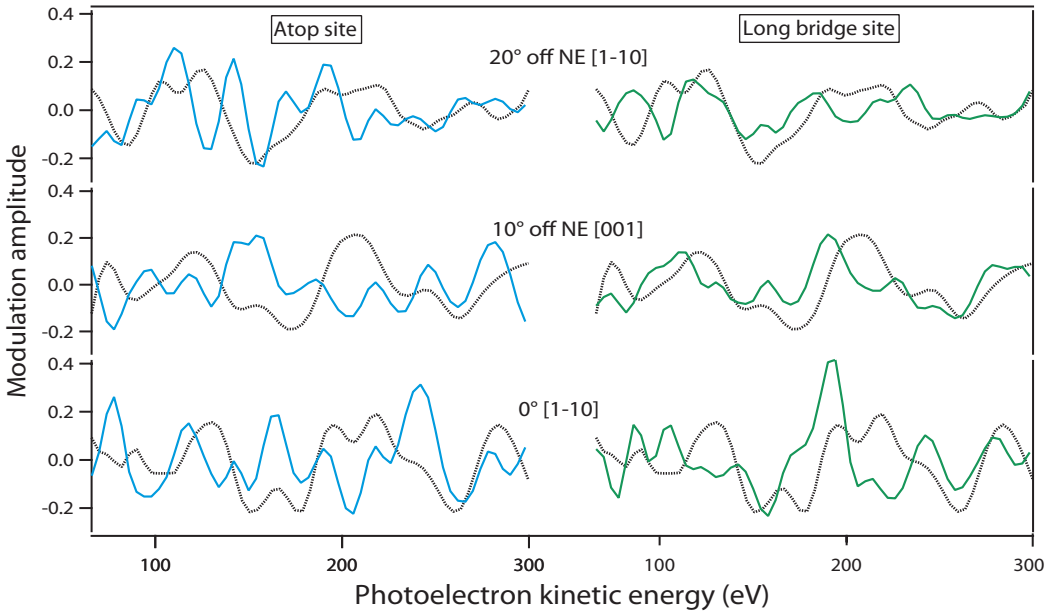

Figure 4.7: Comparison of the experimental and theoretical curves for two different adsorption sites. The black dotted curves lines are experimental curves. In the left the blue curves are the simulations for an atop site with the oxygen atoms in short bridge sites. On the right, a long bridge adsorption site is simulated (green). Here the molecular plane is parallel to the [001] azimuthal direction.

simulations for 0° and 20°, but the relative intensities are completely wrong. This poor agreement seen in the figure is confirmed by the high R-factor value obtained (1.0). For this geometry, the oxygen atoms were located 1.53 Å above the copper atoms, and the bond length between copper and oxygen atoms was 2.0 Å. The separation of the oxygen atoms was 2.55 Å, and between oxygen and carbon was 1.50 Å. For the long bridge adsorption site the same distance between oxygen atoms, and between the carbon and oxygen atoms, were obtained. The height of the molecule above the copper surface was 1.90 Å resulting in a bond length of 1.98 Å. As shown in the figure, the agreement for this adsorption site between experiment and simulation for 0° is quite poor, but it is much better for 10° and 20°, albeit the R-factor is 0.67 which is still quite bad. Of course, a better R-factor can be achieved by increasing the O-O distance. If the O-O distance of the formate is increased from its expected value of 2.33 Å to a value closer to the Cu-Cu distance in the [001] direction of 3.61 Å , the R-factor can be reduced to ≈0.3. However, this would lead to a physically very improbable long bridge adsorption site, because of the unreasonably long O-O distance.

4.3 Formate on Cu(111)

This system was measured at the same beamline as that used for experiments on formate on Cu(110) in January of 2010, and the same procedure was carried out to clean and prepare the sample. The surface was cleaned by argon sputtering and annealing cycles, using the same sputtering cycles as for the previous system. The cleanliness of the sample was checked using XPS, which showed no contaminants. A sharp (1x1) LEED pattern was observed after the cleaning. The sample was exposed to 5L of formic acid were dosed with the sample maintained at ≈ 140 K. As for the previous system, neither the (1x1) nor any other LEED pattern were observed after the dosing. The XP spectra of the O 1s and C 1s from the dosed sample are shown in Figure 4.8. These spectra were taken at 0° of polar emission angle in the [1 $\bar{1}$ 0] azimuthal direction. The photon energies used were hν = 650 eV for O 1s and hν = 400 eV for C 1s. Three different spectra are shown, one immediately after the dosing (red), one after a PhD scan (black), approximately 2 hours after the dosing, and one after a short annealing to room temperature following the PhD scan (grey).

The same effect as for formate on Cu(110) in the XP spectrum was observed for this system. In the spectrum taken after a PhD scan, the peak appears to shift to lower kinetic energy. This shift, as in the previous case, was assigned to increased intensity at higher binding energy due to contamination of water and formic acid.

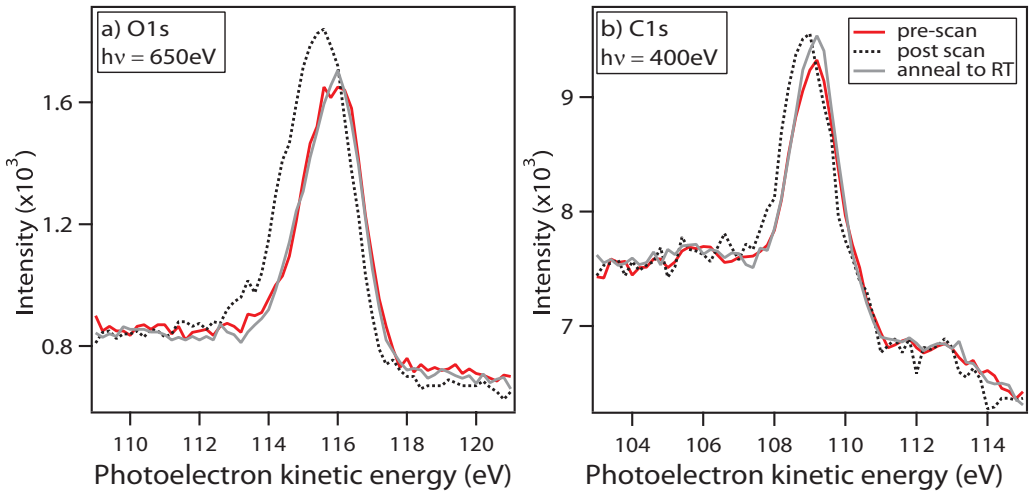

Figure 4.8: a) O 1s and b) C 1s XP spectra of the dosed sample immediately before the PhD scan (red), after the PhD scan (black), and after a short annealing to RT (grey), taken at normal emission. The same effect as for formate on Cu(110) was observed: increased intensity at higher binding energy can be seen, but this vanishes after a short annealing to room temperature.

Hence, this system was also briefly heated to room temperature after dosing and at the end of every PhD scan. These short annealings were performed to avoid the accumulation of these two contaminant species on the sample. A fit of the O 1s spectrum from the contaminated surface in terms of two components is shown in Figure 4.9.

4.3.1 PhD Results

In this case, many O 1s PhD data sets were taken, namely at polar angle of 0°, 5°, 10°, 15°, 20°, 40° and 60° in [1 $\bar{1}$ 0], and 0°, 5°, 10°, 20°, 40° and 60° in [$\bar{2}$ 1 1]. Figure 4.10 shows a summary of all these data. Many of them were repeated to check the reproducibility, as was the case. A qualitative analysis of these data shows that the χ functions with the largest modulations correspond to those closer to normal emission. The χ functions for angles beyond 20 degrees show very little modulation. Since the largest contribution to the PhD comes from atoms in a 180° backscattering geometry with respect to our emitter (in this case oxygen) and here the largest modulations appear at normal emission, this implies that the adsorption site of the oxygen atoms is probably on top of copper atoms. This means that the formate again occupies a short bridge adsorption site. Three of these PhD spectra were chosen to pursue the quantitative analysis. The method of selection of these

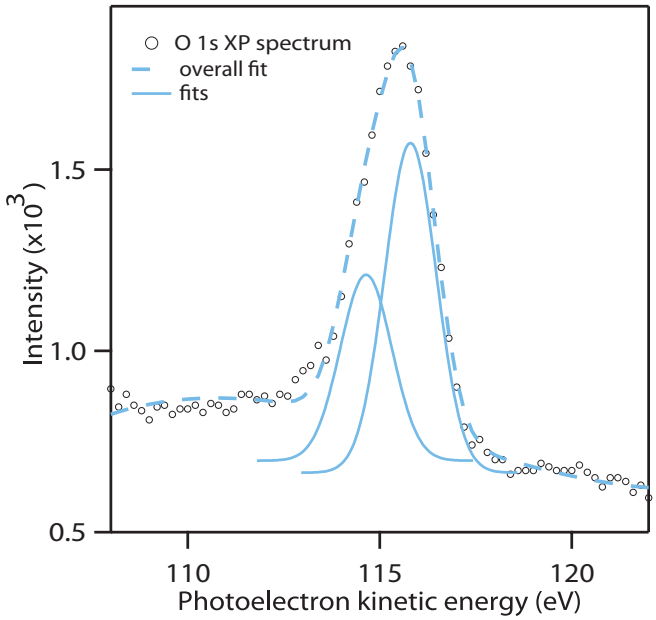

Figure 4.9: Fit of the O 1s XP spectrum taken after the PhD scan. The peak at 115.8 eV corresponds to formate, whilst the peak at 114.6 eV is assigned to a contamination of water and a multilayer of formic acid, as in the case of formate on Cu(110).

three spectra was the same as mentioned in subsection 4.2.1.

The best fit was obtained, as expected, for a formate in a bridge site along the close-packed direction, [1 $\bar{1}$ 0]. As on Cu(111) there are three equivalent domains, three formate molecules along the symmetrically equivalent azimuthal directions were simulated in the unit cell. The comparison between the multiple scattering simulations and the χ functions can be seen in Figure 4.11, where the black curves are experimental and the red curves are the result of the simulations. For this best fit structure, the molecule is situated 1.99 Å above the copper surface, resulting in a bond length between oxygen and copper atoms of 1.99 ± 0.04 Å. The bond length between carbon and oxygen atoms for the best fit was 1.44 (-0.50/+1.30) Å and the separation of the two oxygen atoms was 2.32 (-0.41/+0.59) Å. This geometry is shown in Figure 4.12. The individual R-factors for the three different data sets are shown in Figure 4.11. As it is obvious from the graph the agreement is quite good, though the R-factor for the spectrum at 15° polar angle looks far from perfect. However, in this spectrum the modulations are less than 15%; poor R-factors often arise for spectra with such weak modulations. The global R-factor obtained for this geometry was 0.26. The variance found for this structure was 0.056, so all geometries

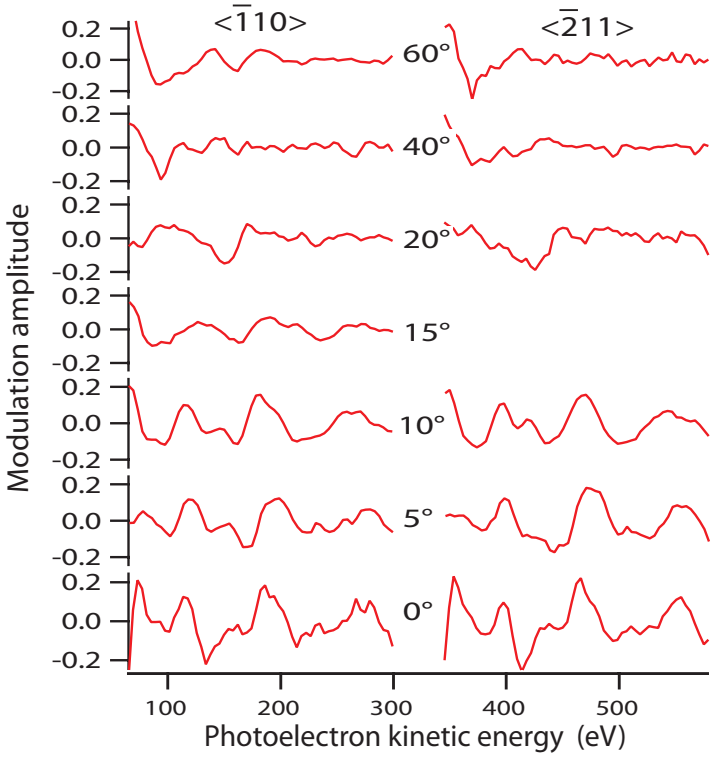

Figure 4.10: Summary of all the modulation functions, χ(E,) taken at different polar angles at two different azimuthal directions, [1 $\bar{1}$ 0] and [001]. For angles bigger than 15° the modulations are very small.

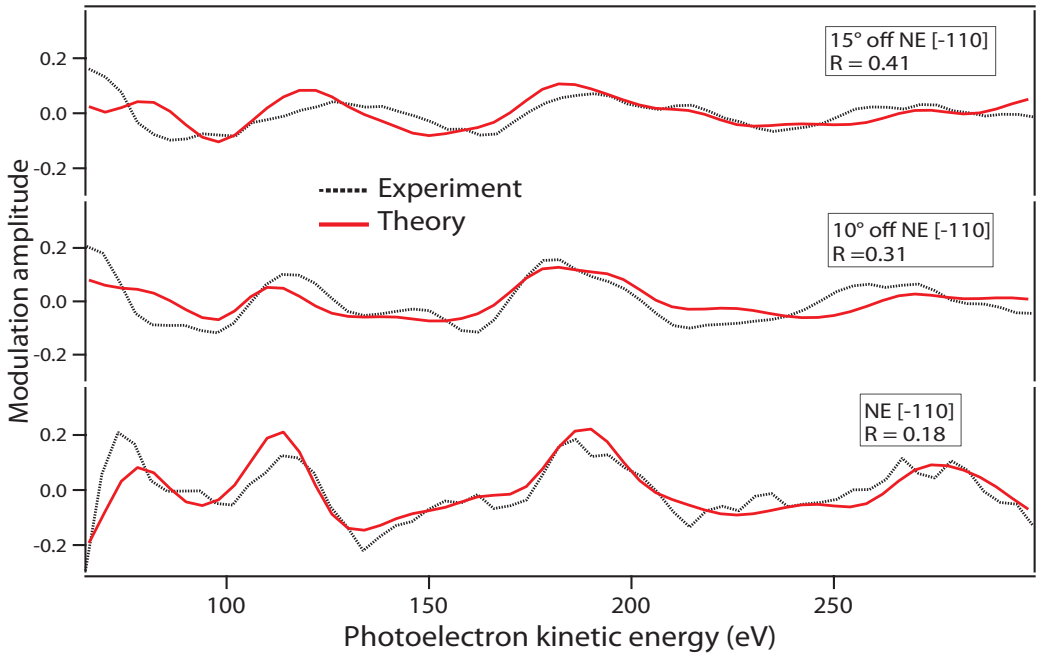

Figure 4.11: Comparison between the multiple scattering simulations and the χ functions at three different angles, all of them in the $[\overline{2}\ 1\ 1]$. The black lines correspond to experiments and the red ones to the theoretical curves.

with an R-factor larger than 0.316 can be rejected.

Another high symmetry adsorption site was also simulated in order to confirm the bridge site as the correct local structure of this system. This adsorption site was an atop position with the oxygen atoms in bridge sites. The comparison between the χ functions and the theoretical simulations of this geometry is shown in Figure 4.13. The parameters obtained for this fit were an oxygen-oxygen distance of 2.33 Å, 1.44 Å between oxygen and carbon atoms and 2.11 Å between the oxygen emitter and the copper atom underneath the molecule. For this geometry the global R-factor obtained was 0.67. As can be seen in the figure, the agreement is not as bad as one might expect. However, this fit was obtained for a relatively large oxygen-copper bond length (2.11 Å). The bond length between the oxygen atom and the second nearest neighbour is even larger, 2.25 Å. These large values are physically unlikely, so this adsorption geometry could probably have been excluded even if the R-factor had been much smaller. A more realistic bond length, for example 2.0 Å, gives a much higher R-factor (≈ 1.0).

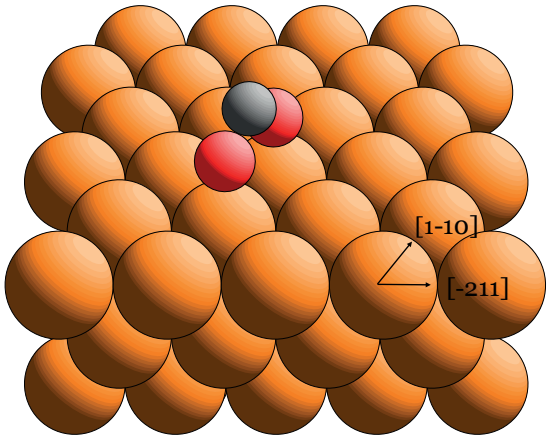

Figure 4.12: Representation of a formate molecule bonding to the Cu(111) surface in a bridge site along the [1 $\overline{1}$ 0]. The orange balls represent the copper atoms, the red ones represent the oxygens and the grey one represents the carbon atom. The hydrogen atom of the molecule is not represented since the PhD technique is not sensitive to it.

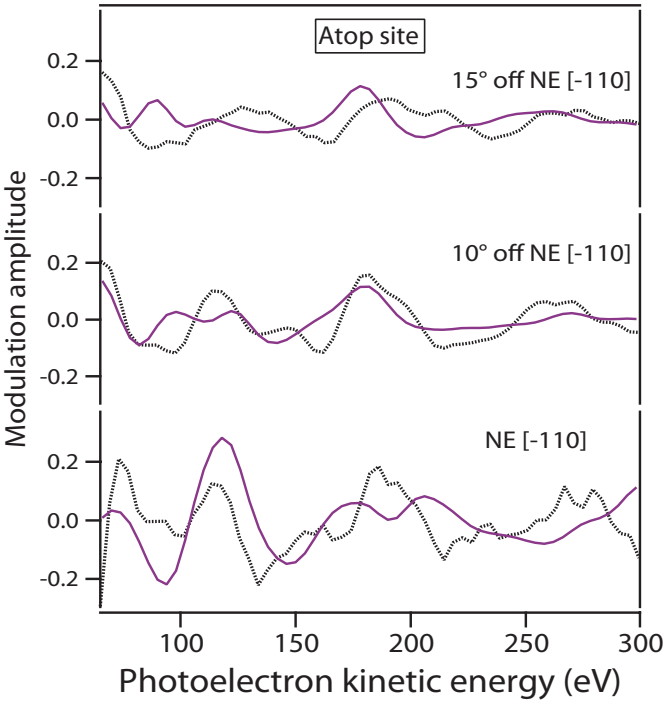

Figure 4.13: Comparison between the χ functions (dotted black) and the theoretical curves (purple) for a formate on an atop position with the oxygen atoms in bridge sites. The R-factor for this geometry is 0.67.

4.4 General discussion and conclusions

As mentioned in the introduction of this chapter, the purpose of this experiment was to establish how surface-atom/molecule bonding depends on the underlying solid. Many studies had already reported on the local structure of this molecule on the three low-symmetry copper surfaces. However, all these measurements were carried out under different conditions. In order to minimize a possible systematical error and to get almost identical conditions these two systems were studied here with the same technique.

Exactly the same adsorption site was found for two different crystallographic orientations of the same metal, namely a short bridge site with the oxygen atoms in slightly off-atop sites (distance between the oxygen atoms is 2.33 Å and between the copper atoms is 2.55 Å). This adsorption site is in agreement with the one reported in other work [65, 76]. There are however some differences between the bond lengths found in this work and in previous reports (listed inTable 4.1).

For Cu(110) the copper-oxygen bond length obtained in this work is within the error of the values listed in the table. Only the value obtained by the PhD study [65] differs a little bit more. It is important to remark that the simulations in the analysis of this PhD were done with a different code, not using multiple scattering.

For the Cu(111) surface the values of the Cu-O bond length showed in Table 4.1 are smaller than the value obtained in this work. The two values shown in the table were calculated with NIXSW, so the inconsistency between the bond lengths could be attributed to any systematic error in the method.

While there are obviously potential problems in establishing the exact absolute bond length values using these different techniques, the primary interest of this work is in the difference in bond lengths for the Cu(110) and Cu(111) surfaces. The use of a single technique means that the measured difference of 0.09 ± 0.05 Å between the oxygen-copper bond length in Cu(110) and in Cu(111) reported here is significant, and implies that the underlying metal solid does indeed influence the bonding.

Two related differences between Cu(110) and Cu(111) surfaces are proposed to explain this chemisorption bond length difference. The first one is the difference in the coordination number of the surface atoms. For the case of Cu(111) the surface atoms are 9-fold coordinated, whereas for Cu(110) they are only 6-fold coordinated. The second difference between these two surfaces would be the Smoluchowski smoothing of the metal valence electron density at the surface of the more

atomically-corrugated Cu(110) surface that leaves surface Cu atoms depleted of valence charge, relative to those on the atomically smooth Cu(111) surface. This depletion of charge consequential reduces the screening of the copper nuclear charge and would lead to a shorter bond length.

Photoelectron diffraction has proved to be very effective to determine the distance between a substrate and a molecule (O-Cu bond length). However, the significant error values for the O-O distance, and in particular, the much larger error values for the C-O bond length reveal an insensitivity to the direction parallel to the surface and to the atoms "far away" from the surface.

Density functional theory calculations were performed also on these two systems by M. Bradley to get extra information. The CASTEP 5.0 pseudopotential plane-wave [70] code was used with the following parameters: 5-layer slabs to represent the Cu substrates, one formate species per (3x2) mesh, ultrasoft pseudopotentials, 6x6 ((110)) and 6x8 ((111)) Monkhorst-Pack k-point sampling, and 420 eV energy cut-off. These DFT calculations reproduce qualitatively the effect shown in the experiments: both RPBE and PBE (Perdew-Burke-Ernzerhof) functionals yielded Cu-O bond lengths that are 0.04 Å longer on the (111) surface than on (110). However the absolute values of the bond lengths in DFT are larger than the experimental values (e.g. for (111) the RBPE and PBE values are 2.04 Å and 2.01 Å , to be compared with the experimental value of 1.99 Å), but discrepancies between experiment and theory of up to 0.1 Å are common in molecular adsorption systems. Checks using doublesided slabs showed that these calculated bond lengths are not influenced by surface dipole-derived fields in the supercell. DFT-D calculations showed no influence of dispersion forces, also thus confirming that the bond length difference can be attributed entirely to changes in the metallic and covalent bonding at the two surfaces. A difference in adsorption energy, with the value being $\approx$ 0.4 eV/molecule larger on Cu(110), was also observed.

4.4.1 Conclusions

The structure of a molecular species (formate, HCOO) has been determined on two different crystallographic surface orientations of the same metal (Cu) that differ in their atomic corrugation, namely the more open-packed Cu(110) and the close-packed Cu(111). The local molecular bonding geometry is found to be the same for both terminations, namely a bridge site with the oxygen atoms in off-atop positions. To compare the values of the bond lengths it was important to minimize the influences of systematic error in the measurements. This was achieved by using the same technique for both surfaces of energy-scanned photoelectron diffraction.

A small chemisorption bond length difference on the two different crystal faces was indeed observed. This result was qualitatively reproduced by density functional theory calculations, which also show a significant difference in adsorption energy on the two surfaces. this appears to be the first clear and quantitative evidence that the surface-atom/molecule bond is influenced by the underlying bulk metal, and therefore, that this bonding is not entirely equivalent to organometallic bonding.

Chapter 5

Reaction intermediates of methanol oxidation under steady-state conditions

5.1 Introduction

The local structure of the two main intermediate products of methanol oxidation in ultra high vacuum have been presented in chapter 3 and chapter 4. However, the interest in the oxidation of methanol to formaldehyde relies on its applications in heterogeneous catalysis, usually performed at much higher pressures than in surface science. In the last few years, it has been shown that many surface reactions behave differently at UHV and at higher pressures. XPS under "high pressures" (up to a few millibar) has been studied successfully since the 1970s [84, 85]. Methanol oxidation over copper is one of the most studied systems under these more realistic conditions using XPS, but also using other techniques such as LEED and temperature-programmed reaction spectroscopy [60–62, 86, 87].

In two papers published by Zhou, Günther and Imbihl [60] and [61], steady-state methanol oxidation in the pressure range between 10^{-7} mbar and 10^{-3} mbar was studied by TPRS, LEED, Auger electron spectroscopy, photoelectron emission spectroscopy, and reaction rate measurements. In the first paper [60], a high selectivity for the product formaldehyde was found at lower pressures. The reactivity of the surface at low and intermediate oxygen coverage was high, whereas a high oxygen coverage inhibited the reaction. The reactivity showed two different maxima at low pressures, one at 400-520 K, which vanished at higher pressures, and a second one at 900 K, which persisted at higher pressures. A hysteresis in the reaction

kinetics depending on whether the temperature is increased or decreased to reach the reaction conditions was also observed. The low-temperature reactivity peak shifted by $\approx$ 20 K to a higher temperature for each order of magnitude difference in pressure. In the second paper [61], two different surface structures were found with LEED. The first one was a (5x2) reconstruction, which was assigned to the intermediate product methoxy. This structure was observed after sequential dosing of oxygen and methanol with a ratio of 1:0.6. The base pressure was 1x10^{-7} mbar. Also a c(2x2) pattern was observed, which was related to the formate species. This structure was found after co-dosing at 300 K with the partial pressures increased by two orders of magnitude. These two structures were only stable up to $\approx$ 380 K, the surface being unreactive. Longer exposures led to the formation of a (2x1) pattern, which coexisted with the (5x2) and the c(2x2) structures.

Bluhm et al. [87] also reported on this system, but under different reaction conditions. At pressures as high as 0.6 mbar and 400°C they did not observe any surface intermediates of the reaction and found that the copper surface was only active when oxygen was coadsorbed. The presence of a subsurface oxygen species embedded on the copper substrate was also reported, and the abundance of this species was correlated with the amount of formaldehyde that was created.

The fourth publication that is relevant for MeOH oxidation under high-pressures is the one by Günther et al. [62]. In this work, XPS and rate measurements were used for the study of the adsorbate coverages and surface reactivity of methanol oxidation over Cu(110). The system was studied in the 10^{-5} mbar range and the two reaction intermediates, formate and methoxy, were observed on the sample. The first one dominated on the inactive surface (300 K - 350 K), forming a c(2x2) structure, as observed by LEED. Methoxy was almost absent in this range. The coverage of methoxy was always small, but it was present up to $\approx$ 600 K. Two different oxygen states were also found: one chemisorbed species, and another unidentified species, which dominated at high temperatures.

However, despite the numerous publications on high-pressure surface science, there is no quantitative structural study of this system under high-pressures, and in general, there are no structural methods that can be used under high-pressures for surfaces with no long range order. The objective of the present work was to establish whether it is possible to use photoelectron diffraction to determine the local structure of the intermediate species of a reaction (methanol oxidation) under steady-state conditions. In this thesis, the study of methanol oxidation over Cu(110) in a pressure range from 1x10^{-5} to 1x10^{-3} mbar at different temperatures using photoelectron diffraction is reported.

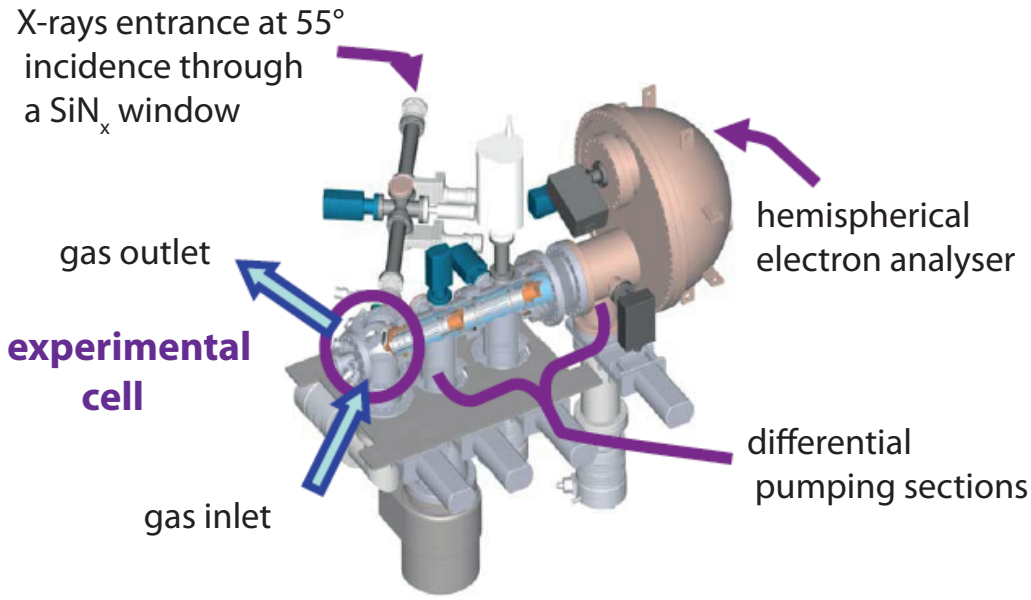

Figure 5.1: Sketch of the experimental chamber at the ISISS beamline at BESSY II taken from [88]. The setup consists of an experimental cell connected to the beamline through a SiN_x window and a hemispherical analyser attached to the cell through a system of differential pumping stages. The experimental cell can be filled with gases up to the mbar range.

5.2 Results

This experiment was carried out in November 2008 at the beamline *Innovative Station for In Situ Spectroscopy* (ISISS) at BESSY II.

The ISISS beamline exploits the synchrotron radiation from a bending magnet, with photon energy from 80 eV to 2000 eV. Although the flux of the SR from a bending magnet is lower than the radiation of an undulator, it was still possible to perform photoelectron diffraction. The experimental station (see Figure 5.1) placed at the ISISS beamline consists of a preparation chamber, and the experimental cell connected to a mass spectrometer, an infrared laser to heat up the sample, and a hemispherical electron analyser. The X-ray beam enters the chamber through a SiN_x window at an incidence angle of 55°. In these high-pressure chambers, the light from the X-ray source usually passes through a window (e.g., Al, Si, Be) in order to protect the beamline. Unlike the experimental chamber used for the study of PhD under ultra high vacuum, in this chamber the sample could not be rotated, neither in the polar nor in the azimuthal angle. Therefore, all the PhD scans were measured at or close to normal emission. In order to avoid the strong scattering of

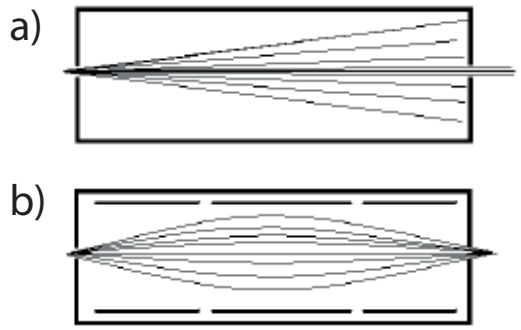

Figure 5.2: Schematic diagram taken from [88] showing the electron trajectories inside a differentially pumped aperture system a) without electrostatic lenses, b) with electrostatic focusing lenses included. In this diagram, the electron are traveling from the left to the right.

the photoelectrons in the gas phase, which reduces the signal at high-pressures, the sample is located very close ($\leq$ 1 mm) to an aperture which leads to a differential pumping system. In this way, the distance that the photoelectrons need to pass under high-pressure is minimised. This pumping system consists of three differential pumping stages (from 1x10^{-4} to 1x10^{-8} mbar) connected to the electron analyser (P $\approx$ 1x10^{-9} mbar). In each of those pumping stages, the photoelectrons are focused through an electrostatic lens system, thus increasing the acceptance and the electron collection [88]. This lens system is depicted in Figure 5.2.

The Cu(110) sample was cleaned *in situ* by several cycles of argon sputtering and annealing, as described in section 3.2. The sample was sputtered for 30 minutes in a background pressure of 1x10^{-4} mbar Ar. The acceleration voltage was 5 keV, resulting in a sample current density of $\approx$ 3 μA/cm^2. The sample was then annealed to $\approx$ 800 K. XPS revealed a small amount of carbon contamination that only disappeared by annealing the sample in a background pressure of 1x10^{-6} mbar O_2 to 800 K, switching off the gas after turning down the temperature to 300 K.

The chamber was filled with a mixture of methanol and oxygen with a ratio of 3:2, varying the total pressure from 1x10^{-5} to 1x10^{-3} mbar. The different preparations led to significant variations of the surface coverage. A large number of scans taken with different temperatures and pressures were measured. Since Zhou and coworkers [60] had seen a hysteresis in the formaldehyde production depending on whether the temperature was increased or decreased to reach the reaction conditions, different dosing procedures were performed to identify the temperature at which formaldehyde production was initiated. As PhD spectra show larger modulations at lower temperatures, it was more interesting to reach the reaction conditions

by decreasing the temperature. Figure 5.3 shows the most interesting data sets, when formaldehyde production was observed, measured with XPS at different temperatures and pressures. The procedure followed for these data sets to reach the reaction conditions was to dose the gases initially at 770 K, and then to decrease the temperature to $\approx$ 500 K. On the left, the C 1s spectra of the different data sets, measured with a photon energy of 400 eV, are shown. On the right, the O 1s spectra, measured with $h\nu = 650$ eV, are shown. The first data set, (Figure 5.3 *a1,a2*), was measured at 510 K at a total pressure of 1x10^{-3} mbar. Under these conditions, the production of formaldehyde was observed with the mass spectrometer and the amount of formaldehyde was stable indicating steady-state conditions. Three different carbonaceous and five oxygen-containing species can be distinguished. Correctly identifying all these peaks in the absence of a reliable absolute binding energy calibration proved quite difficult, but eventually a consistent scheme was established to fit all the data obtained under a wide range of conditions. Following the peak assignment used in section 3.2, the large feature at 116.9 eV in the C 1s spectrum was assigned to CH_x, *C1*, the methoxy peak, *C2*, was shifted 1.5 eV towards lower kinetic energy and the formate peak, *C3*, appeared at 113.8 eV. These shifts, however, are slightly smaller than those observed in UHV (see Table 3.1). This was also one of the difficulties found to establish the nature of the peaks. Differences in the shifts between different surface species measured in different studies have already been reported by Günther et al. [62].

In the O 1s spectrum, the adsorbed atomic oxygen, *O1*, appeared at a kinetic energy of 121.4 eV. The feature shifted $\approx$ 1 eV toward higher binding energy was assigned to methoxy, *O2*, and the peak shifted $\approx$ 0.65 eV from the methoxy also towards higher binding energy was assigned to formate, *O3*, as in UHV. The O 1s peaks for methoxy and formate are very difficult to resolve, as shown in section 3.2. In order to confirm the nature of these oxygen-containing species, the relative concentrations of formate and methoxy were established from the C 1s spectrum. Since formate and methoxy have the same amount of carbon, but formate has two times more oxygen than methoxy, the ratio obtained from the carbon spectrum allowed the peaks from these two species in the oxygen spectrum to be fitted. For example, in Figure 5.3*a1*, the ratio between the concentration of carbon from methoxy and the concentration of carbon from formate was 5. Therefore, the ratio for the oxygen components of these species had to be 2.5, and thus, the fit of the oxygen peaks was constrained to fulfill this condition. This fitting procedure was performed for every preparation.

Two other oxygen-containing species appeared at lower kinetic energies, *O4*

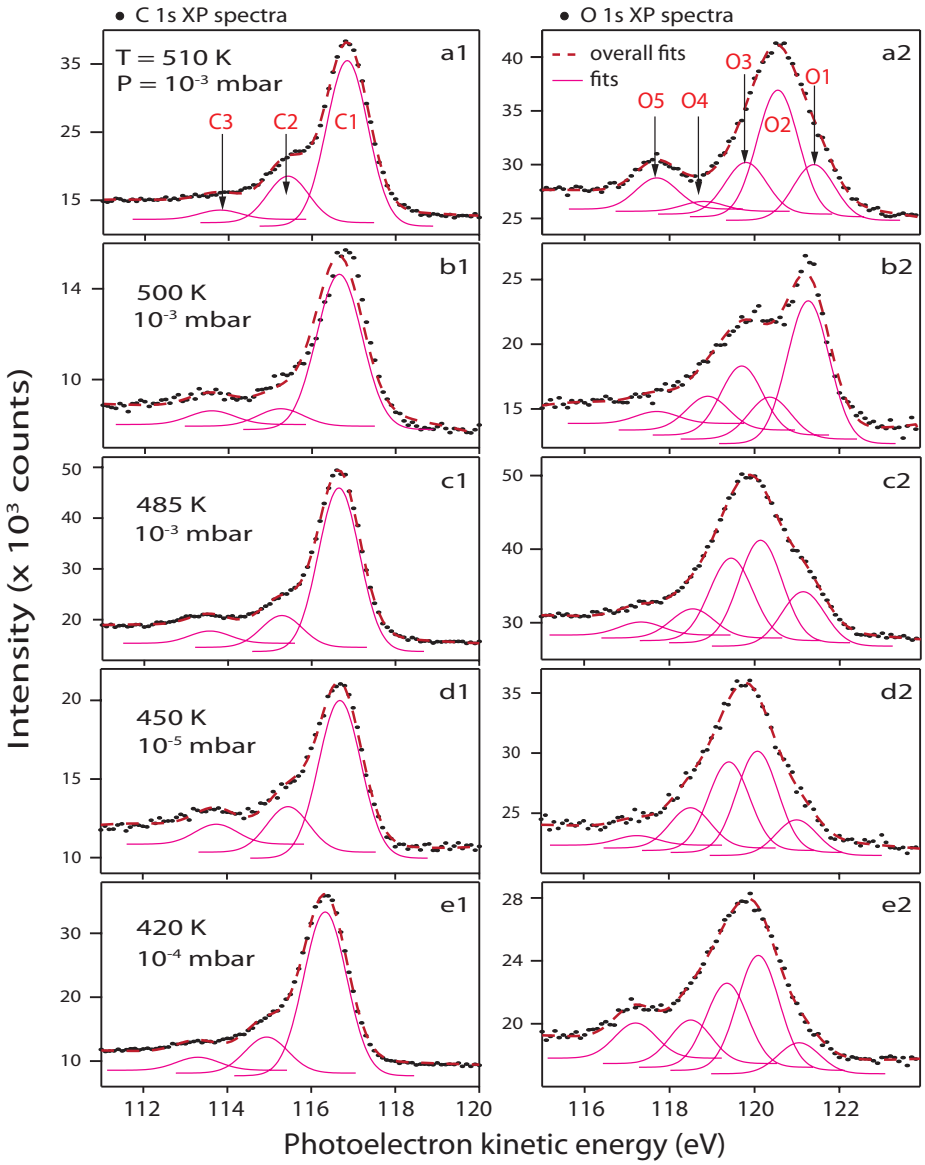

Figure 5.3: XP spectra of five different methanol and oxygen on Cu(110) data sets, recorded at different temperatures. On the left, the C 1s spectra measured at $h\nu$ = 400 eV are represented, and on the right, the O 1s spectra measured at $h\nu$ = 650 eV. The different temperatures and pressures are also shown.

and *O5*, significantly shifted with respect to the adsorbed oxygen. In the study of Bluhm et al. [87] the O 1s XP spectra showed additional peaks related to gas-phase species in front of the sample, that were also irradiated by the synchrotron light. Some of these peaks appear at kinetic energies shifted from the adsorbed oxygen by similar chemical shifts as in the spectra shown in this thesis. Following their assignment, *O4* would be attributed to methanol in the gas phase, and *O5* to water in the gas phase. However, the results presented by Bluhm and coworkers were measured at a pressure of 0.6 mbar, three order of magnitude higher than the results presented in this thesis, so their presence in our spectra is surprising.

In order to check how stable the preparation method was, the experiment was repeated. The corresponding XP spectra are shown in Figure 5.3 *b*. At this temperature, formaldehyde production was observed. The amount of adsorbed oxygen (*O1*) was larger than in the other data sets. The goal in this experiment was to achieve steady-state conditions under the lowest temperature possible. As mentioned before, it is preferable to perform PhD experiments at lower temperatures, due to the large vibrational amplitudes at high temperatures. As the reaction was still not at steady-state conditions, and the oxygen peak was still higher than the methoxy and formate peak, indicating that it had not completely reacted yet with methanol, we waited for 10 minutes. After this time, the height of the oxygen peak was reduced and methanol and formate had increased. Formaldehyde production was not yet stable. After that, the temperature was reduced to 485 K, where formaldehyde production was still observed. After 15 minutes, XPS scans were taken, showing how the oxygen peak was decreased and the amount of the other intermediate products was increased (Figure 5.3 *c*). The production of formaldehyde was then stable, indicating that the reaction had reached the steady-state.

The last two data sets, (Figure 5.3*d*, *e*), were taken at different background pressures and at lower temperatures, but the number of species on the sample was the same as for higher temperatures and pressures. However, at temperatures lower than $\approx$ 440 K, the formaldehyde production was significantly reduced, until finally the formaldehyde masses were no longer observed in the mass spectrometer. Note that there were oscillations in the partial pressures of both gases, methanol and oxygen. This could be the reason to variations in the relative coverage of the different surface species. The conditions under which formaldehyde production was observed are in agreement with references [60, 61].

Note also that Figure 5.3 shows how all the peaks in the O 1s and in the C 1s spectra shift towards lower binding energy with increasing temperature. The shift between a scan of the same species taken at 340 K and another one taken at 820 eV

was of 2 eV. This effect was more noticeable at temperatures higher than 550 K and it was observed also during other experiments in that chamber. The origin of this shift remains unknown but has been seen by other users of this instrument. This shift does not affect the PhD measurements, but the whole modulation function will be shifted a few tenths of eV to higher kinetic energies with respect to the UHV scans taken at $\approx$ 140 K.

5.2.1 PhD results

PhD scans were measured at normal emission in the [1 $\bar{1}$ 0] azimuth at different temperatures and pressures. Figure 5.4 shows a comparison of the PhD scans for formate and methoxy under different conditions at the same geometry. Specifically, there are two UHV measurements (shown in subsection 3.2.1 and subsection 4.2.1), four taken at 1x10^{-5} mbar at 310 K and 450 K, and two scans taken at 1x10^{-3} mbar at 510 K. The spectra assigned to formate at 310 and 450 K look very similar to the data from formate in UHV. Although the modulations are weaker and not all the fine structure can be resolved, the main features are present in both scans (blue and red) with their maxima appearing at the same energies, implying that the adsorption site is the same in UHV and at higher pressures. In particular, this is also true for the data recorded at 450 K under conditions corresponding to a steady-state reaction producing formaldehyde. The methoxy data are much noisier than those from formate. Note that in UHV, the modulations are weaker at normal emission than for larger angles close to 30°, due to the methoxy binding to copper in a bridge site. However, as mentioned before, it was not possible to rotate the sample to this more favourable geometry. Although noisier, the PhD scans at 310 K and 450 K show large enough modulations to be compared with the UHV data, revealing strong similarities amongst the experiments. Only the one peak at kinetic energies lower than 100 eV is missing from the scans measured at higher pressures.

The PhD scan in the upper part of Figure 5.4 (yellow) shows very weak modulations, comparable with the noise amplitude. The most important factor for these weak modulations was the temperature rather than the pressure. At temperatures higher than $\approx$ 470 K, none of the PhD scans showed significant modulations. In part, this effect can be attributed to the Debye-Waller factor at the higher vibrational amplitudes [32].

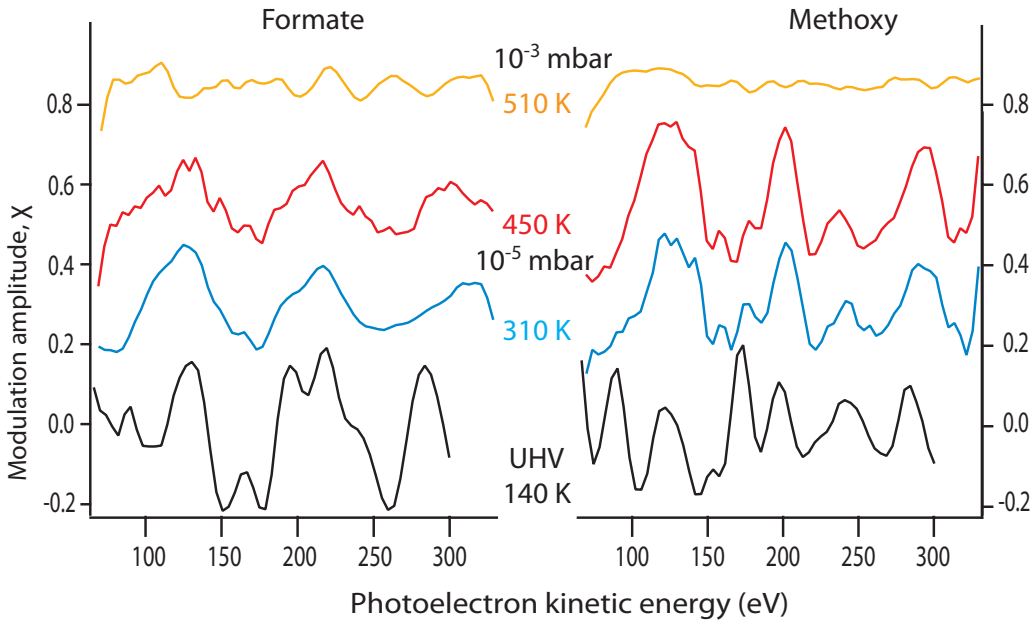

Figure 5.4: Comparison of PhD scans taken under ultra high vacuum (black line), at 1x10^{-5} mbar (blue and red lines) and at 1x10^{-3} mbar (yellow line). On the left, the PhD scans associated to the peak assigned to formate are shown. On the right, the PhD scans associated to the methoxy peak. The scan measured in UHV was taken at 140 K. The scans at higher pressures were taken at 310 K, 450 K and 510 K.

5.3 Conclusions

Photoelectron diffraction was used to investigate the local structure of intermediates of a chemical reaction under steady-state conditions. Steady-state reaction conditions were achieved with enough stability to perform photoelectron diffraction scans. A high yield of formaldehyde production via methanol oxidation was observed for temperatures $\approx$ 500 K, although at temperatures lower than this, it was still possible to observe the reaction. PhD scans taken at the highest temperatures failed to show significant modulations. At lower temperatures, at which PhD works well, the PhD scans reproduce the results obtained for ultra high vacuum measurements. Therefore, it can be concluded that methoxy and formate bonds to the Cu(110) surface with the same adsorption site as under UHV conditions, as reported in subsection 3.2.1 and subsection 4.2.1.

PhD modulations at temperatures higher than $\approx$ 450 K were almost negligible. Of course, at high temperatures, the vibrational amplitudes are larger and the Debye-Waller factor smooths out slightly the modulations. This would show, however, a smaller effect than the one seen in the experiments. One possible reason is that, at these high temperatures, the mobility of the adsorbates also increases. It could be that the lifetime of the surface intermediates was shorter at these temperatures and thus, the adsorbates could hop from one site to the next one. This could reduce significantly the amplitude of the modulations. At temperatures higher than $\approx$ 570 K, the amount of the surface intermediates on the sample is much smaller. This can result on much worse signal-to-noise ratio, hindering the observation of the true modulations.

The XPS measurements revealed the presence of methoxy and oxygen, the main intermediate products in formaldehyde production, and also the presence of formate. This latter species usually poisons the reaction. In the experiment presented here, however, the rate of methoxy, and thus formaldehyde production, is higher than the formate production rate, hindering the contamination of the sample.

In this chapter, it has been proved that it is possible to perform scanned-energy photoelectron diffraction to determine the local structure of adsorbates on a sample under reaction conditions, but is particularly challenging at high temperatures.

Chapter 6

The local structure of the reaction intermediate phenyl imide on TiO_2

6.1 Introduction

The (110) face of the rutile phase of titanium dioxide, TiO_2, is the most studied metal-oxide surface [89]. In particular, its applications in heterogeneous catalysis (e.g., as a photocatalyst, as a gas sensor, as an optical coating, in solar cells for the production of hydrogen and electric energy, as white pigment, etc...) are the motivation for many investigations. The discovery of the properties of TiO_2-supported Au nanoparticles (Au/TiO_2) as a catalyst for the oxidation of CO at low temperature [90] gave rise to many new investigations to understand the role of these Au nanoparticles and the interaction between them and the surface [91–94]. Two publications by Corma and coworkers [95, 96] show the use of Au/TiO_2 as a high-yield catalyst for the synthesis of aromatic compounds. In the first one, they show the reduction of nitroaromatics to aniline and in the second one the synthesis of azobenzene by oxidation of aniline. In this latter work it is also shown that the same process is observed using TiO_2 without gold particles, but with a lower conversion efficiency. One of the advantages of Au/TiO_2 as a catalyst over other transition metal catalysts is that it is more "environmentally friendly".

A recent STM study performed by the Diebold group [97], based on the work reported in references [95, 96], claims that TiO_2 indeed shows a similar catalytic activity to Au doped titanium dioxide. In order to prove this, they studied the adsorption of two different aromatic molecules, aniline (C_6H_7N) and azobenzene

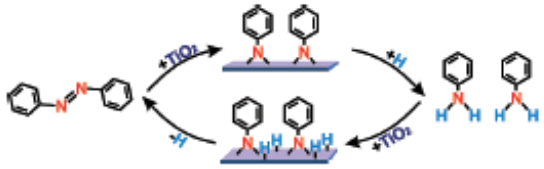

Figure 6.1: Reaction model of aniline and azobenzene proposed by Li and Diebold [97]. By dosing aniline on TiO_2, an intermediate phenyl imide species adsorbs on the sample via dehydrogenation and this species can further recombine to form azobenzene. In the same way, by dosing azobenzene on the TiO_2 surface, the same intermediate species is adsorbed on the sample, and via hydrogenation aniline is formed.

($C_{12}H_{10}N_2$), on two different TiO_2 surfaces. The adsorption of aniline resulted in the formation of a superstructure believed to be composed of a phenyl imide intermediate product. The adsorption of azobenzene resulted in the formation of the same superstructure, which would imply the cleavage of the N=N bond of the molecule in order to form the same reaction intermediate product (C_6H_5N). The reaction model proposed by Li and Diebold is shown in Figure 6.1.

The interest of the study presented in this thesis arose from this latter publication [97]. The goals of this experiment are:

1. to establish by other methods whether aniline and azobenzene do result on the same adsorbed species on TiO_2 and

2. to obtain quantitative structural information on the adsorbed species.

The adsorption of the two molecules, aniline and azobenzene, has been studied with photoelectron diffraction, and also with NEXAFS, as a support technique. Aniline, also known as phenylamine, is composed of a phenyl ring attached to an amino group. The importance of aniline relies on its applications in industry as important intermediates for pharmaceuticals, polymers, herbicides, etc [95]. The azobenzene molecule is composed of two phenyl rings bound to a N=N double bond. Azobenzene can be found in two different conformers: trans (the most stable one) and cis. The transition between these two isomers using ultra-violet light (photoisomerization) is one of the properties of this compound most studied. The aromatic azo compounds are also widely used in the industry, for example as dyes, pigments, food additives and drugs [96]. Both molecules are shown in Figure 6.2.

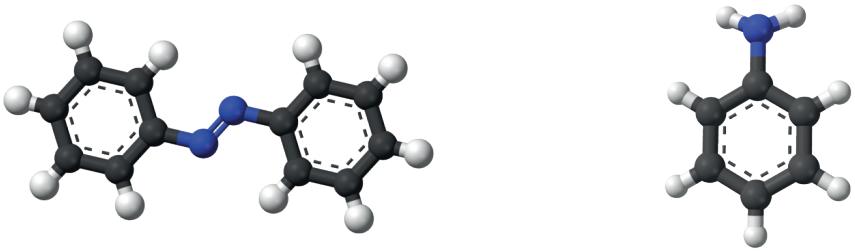

Figure 6.2: Representation of the azobenzene (left) and aniline (right) molecules, where the blue atoms correspond to nitrogen, the grey atoms correspond to carbon and the white atoms correspond to hydrogen.

6.1.1 The rutile TiO_2(110) surface

As mentioned before, titanium dioxide is the metal oxide most investigated [89, 98]. TiO_2 can be found in nature in different forms. The most known titanium dioxide minerals are rutile and anatase. Rutile TiO_2 is the most common form and is also the equilibrium phase at all temperatures [99]. In this work, a rutile TiO_2(110) crystal has been used, which is the most stable crystal face. An illustration of the clean surface structure is shown in Figure 6.3. The bulk-terminated surface consists of rows of oxygen atoms bridging six-fold coordinated titanium atoms (Ti^{4+}) below, rows of undercoordinated titanium atoms and rows of in-plane oxygen atoms, which are three-fold coordinated as in the bulk. The bridging atoms are undercoordinated (two-fold) and it is believed that due to this characteristic, they can be partially removed by high thermal annealing [89]. The unit cell is superimposed on the surface in Figure 6.3. The distance between neighbouring 5-fold coordinated Ti atoms in the [0 0 1] azimuth in the bulk-terminated surface is 2.96 Å , and the spacing between the bridging oxygen atoms in the [1 $\overline{1}$ 0] azimuth is 6.50 Å [100]. As at many surfaces, TiO_2(110) undergoes some relaxations, especially in the direction perpendicular to the surface [89, 101, 102]. The structure of the clean surface has been studied with surface X-ray diffraction (SXRD) [103–105], LEED [106], medium energy ion scattering (MEIS) [107] and more recently with PhD by Kröger et al. [101]. In this latter publication, a table summarizing all the relaxations proposed in the literature is shown.

In order to use this surface for electron scattering and spectroscopic experiments it is necessary that it is conducting. High conductivity is achieved by creating defects in the bulk via reduction, achieved by heating. The change in the conductivity is accompanied by a change of the colour of the crystal, which can be easily

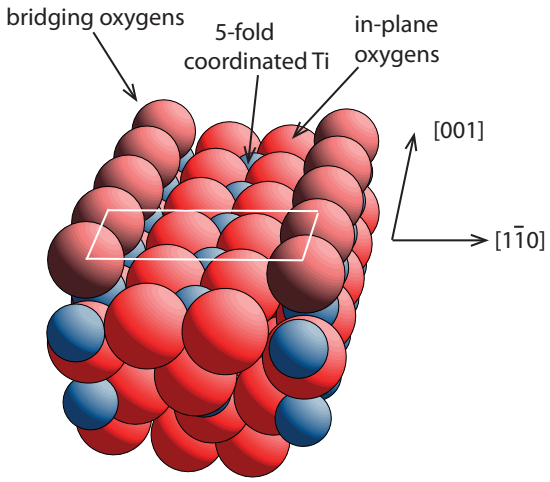

Figure 6.3: An illustration of a rutile TiO_2(110) (1x1) bulk-terminated surface. The blue atoms represent titanium and the red atoms represent oxygen. The light red atoms represent the bridging atoms characteristic of this surface. Following the usual chemical convention for oxides, the oxygen atoms are represented as the larger spheres. The unit mesh is represented by the white box.

observed. The initial colour corresponding to a non-conducting surface is transparent, changing to light and finally to dark blue [89]. There are various types of defects, but the most common ones are thought to be oxygen vacancies. Other defects in the surface are, for example, steps, vacancies produced by thermal annealing or electron bombardment, or impurities (e.g., Ca or H). The vacancies lead to undercoordinated Ti atoms (Ti^{3+}), which appear as a shoulder in the Ti 2p XP spectrum. Their concentration is usually a few percent and they are very important for the surface properties of TiO_2.

The procedure performed to prepare the sample was the following: sputtering the sample at a pressure of Ar of $1x10^{-4}$ mbar for 30 minutes, with the same parameters as used in section 3.2, followed by an annealing in ultra high vacuum (P $\approx$ $1x10^{-9}$ mbar) to $\approx$ 800 K for 10 minutes. The next step was to anneal the sample in an oxygen atmosphere of $2x10^{-7}$ mbar to $\approx$ 700 K for 10 minutes and finally a flash to $\approx$ 1000 K was performed. LEED and XPS were performed to check the cleanliness and periodicity of the surface. A LEED pattern of the clean TiO_2(110) (1x1) surface is shown in Figure 6.4.

No contaminants were observed in XPS and no extra shoulder was observed in the Ti 2p spectrum (see Figure 6.5), which implies that there were only a few oxygen vacancies in the surface. However, the colour of the sample after the preparation turned to dark blue, revealing the presence of a few percent of bulk defects,

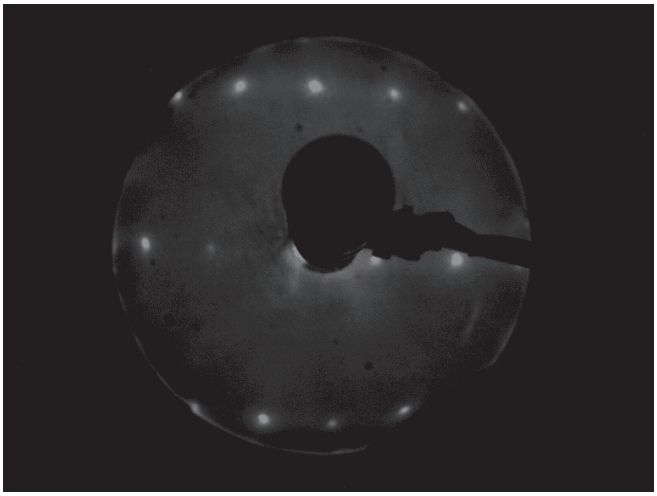

Figure 6.4: LEED pattern showing the (1x1) unit cell of a TiO_2(110) surface, taken at a kinetic energy of 100 eV.

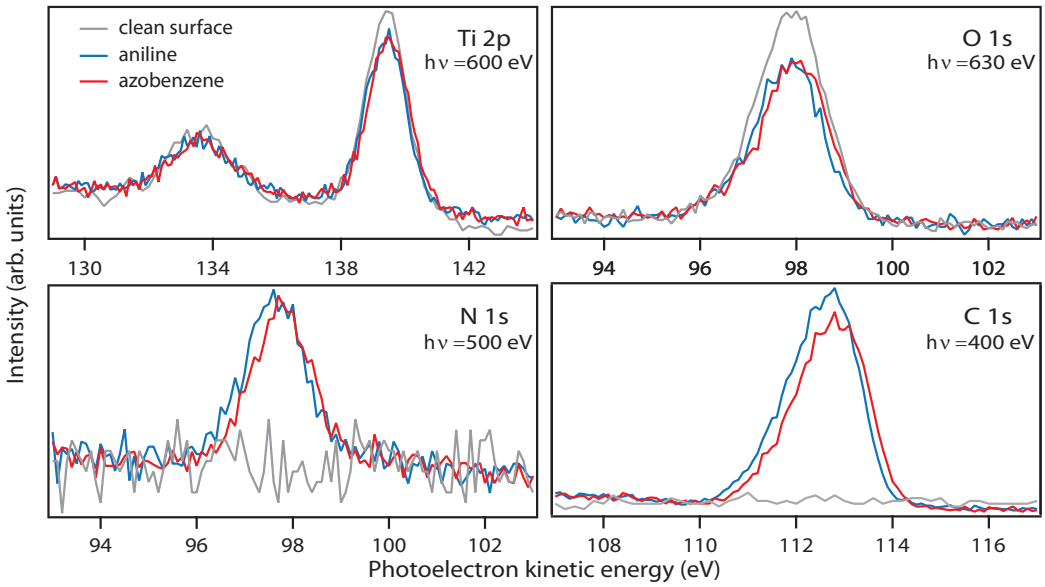

Figure 6.5: XP spectra for Ti 2p, O 1s, N 1s and C 1s. The grey lines represent the spectra taken on the clean surface, prior to the dosing. The red lines represent the sample after dosing azobenzene, and the blue lines correspond to the aniline spectra.

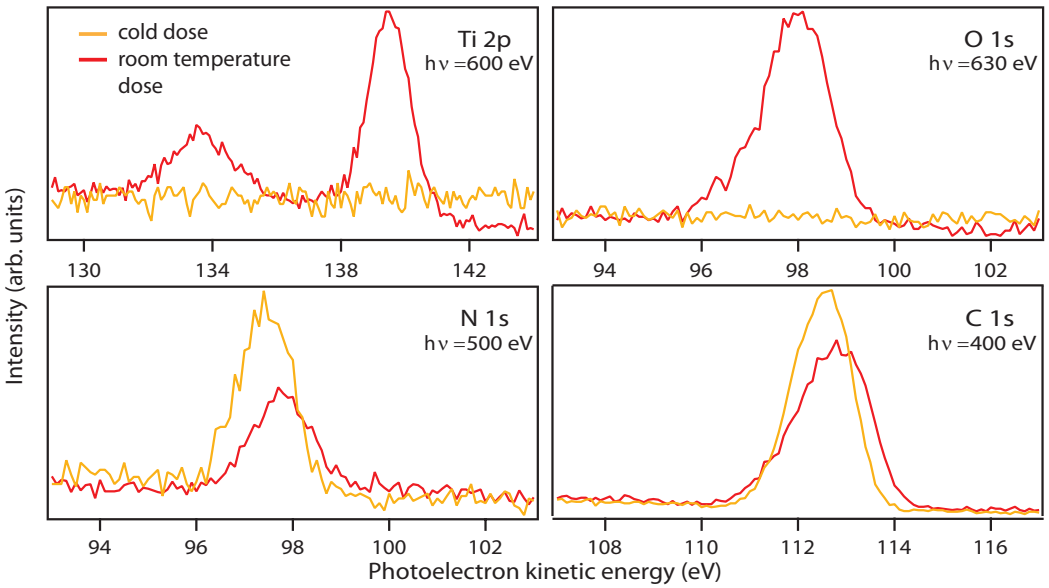

Figure 6.6: XPS for Ti 2p, O 1s, N 1s and C 1s of an azobenzene-dosed sample at room temperature and at 140 K. The red lines represent the spectra taken at room temperature, shown in Figure 6.5, and the yellow lines represent the spectra taken after a dose at 140 K. The cold spectra show the presence of nitrogen and carbon on the sample, but no titanium or oxygen can be seen anymore. This implies the presence of a multilayer on the sample. The C and N peaks are shifted towards higher binding energy with respect to the room temperature dose, characteristic of a multilayer.

characteristic of a conducting sample.

6.2 Results

This experiment was carried out at the beamline UE56-2_PGM-2 (see section 2.1) at BESSY II in November of 2010 and July of 2011. Aniline and azobenzene (Sigma-Aldrich, 99.5 % and 99 % purity, respectively) were dosed at different temperatures, in a range from 150 K to 300 K, to characterise the sample. All the PhD scans were taken at room temperature.

Figure 6.5 shows XP spectra corresponding to Ti 2p, O 1s, N 1s and C 1s, taken before and after the dosing of aniline and azobenzene. In both cases, the procedure for dosing was to open the gas line to the preparation chamber while controlling the mass spectrometer until the desirable masses appeared. It was necessary to heat the azobenzene to $\approx$ 370 K to evaporate it. Then the sample was placed in front of the gas line for 1 to 2 minutes. Freeze-thaw cycles of aniline and

azobenzene were performed prior to the dosing on both molecules in order to remove any possible contaminants. During the first experimental run in November 2010, it was difficult to adsorb azobenzene on the sample, and thus, the coverage was significantly smaller than desired. This problem was solved in the second experimental run by performing more freeze-thaw cycles on the azobenzene. The spectra shown in the figure were taken at normal emission and at room temperature. The O 1s and Ti 2p spectra did not show any impurity and no Ti^{3+} shoulder was observed after dosing the molecules, the same as in reference [97]. The only change seen in the substrate spectrum after the dosing of both molecules was that the Ti 2p and O 1s were slightly attenuated, due to the presence of the adsorbates on the sample. No N or C contaminants were observed on the clean surface. There was only one peak in the N 1s spectrum and it appeared at similar energies for aniline and azobenzene. However, all the XPS peaks for aniline were shifted by ~ 0.1 eV to higher binding energies. This effect was also observed by Li and Diebold in [97]. They explain the nature of this effect as a downward band-bending in the presence of aniline rather than a chemical shift due to different chemical surface species. There was no chemical shift between the two N atoms in the azobenzene. There are three possible explanations for this: first, the chemical shift between the two N atoms was so small that it was not resolved, second, there was no chemical shift if the chemical environment for both atoms was the same or the third possibility is that the N=N double bond was broken and therefore, only one N atom is bonded to the substrate. This would explain why the spectra for aniline and azobenzene look similar. Also in the C 1s spectrum there was a peak at the same energy for both molecules, but this peak was slightly broader than the N 1s peak.The reason could be that the six carbon atoms of the aromatic ring are all contributing to the C 1s spectrum, and not all of them have the same chemical environment. However, as the chemical shifts between the different C atoms can not be resolved, the C 1s peak is broadened.

6.2.1 NEXAFS results

In order to characterise the sample further, an annealing cycle on a sample dosed with azobenzene was performed and NEXAFS scans were taken at different temperatures. The idea was to use N K-edge NEXAFS to check if the nitrogen double bond was intact on the sample, (and if so, at which temperature it would break), and to use C K-edge NEXAFS to gain information on the orientation of the phenyl ring. As mentioned in section 2.5, the π-resonance is observed only if there is a double or a triple bond. Nitrogen K-edge spectra were taken at normal and grazing incidence (80°) in both azimuths ([1 $\overline{1}$ 0] and [0 0 1]). This was done by measuring

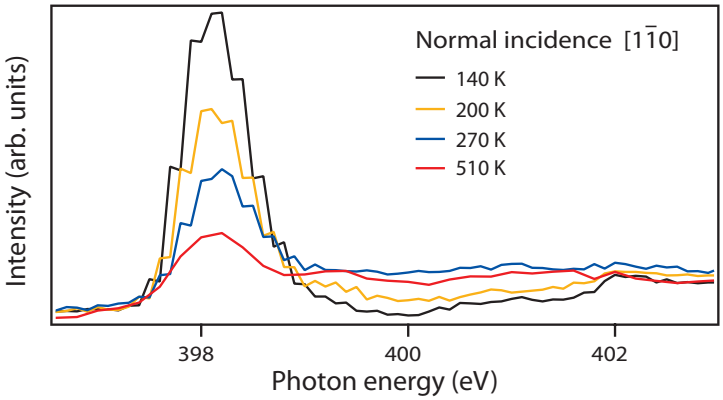

Figure 6.7: N K-edge NEXAFS spectrum of the TiO_2 sample dosed with azobenzene at 140 K (black), resulting in a multilayer. These spectra were taken at normal incidence in the [1 $\bar{1}$ 0] azimuth. The sample was then sequentially heated up. Spectra taken at 200 K (yellow), 270 K (blue), and at 510 K (red) are shown here. A π-resonance appeared at 398 eV. This feature decreased with increasing temperature.

in the Auger electron mode by setting the detector energy to 377 eV. In Figure 6.7, the scans taken at normal incidence in the [1 $\bar{1}$ 0] azimuth are shown. Azobenzene was dosed at 140 K. The XP spectra for N 1s and C 1s showed large peaks, and no Ti and O peaks could be observed (see Figure 6.6). The XPS results implied, as expected, that there was a multilayer on the sample. In the multilayer, the spectra taken at different geometries looked the same, since it is likely that the molecules will not be oriented in any preferential direction but rather be randomly oriented. A huge π feature dominates the 140 K spectrum, implying the presence of the intact azobenzene molecules. On heating to increasing temperatures, the π-resonance decreased, but it never disappeared, even at temperatures as high as 510 K.

The result of dosing azobenzene at room temperatures was very different. Figure 6.8 shows the N K-edge NEXAFS spectra of a sample dosed with azobenzene at normal and grazing incidence in the two azimuths mentioned before. Comparing the graph on the left with Figure 6.7, the most remarkable feature was that the π-resonance at 398 eV had vanished. This indicates that the N=N double bond was broken, and the azobenzene molecule was not anymore intact on the sample. Notice that the large peak at an energy $\sim$ 400.5 eV is not a true NEXAFS feature, but is due to photoemission from a valence state which happens to appear at an energy similar to that at which the σ-resonance should occur. The photoelectron nature of the peak was proved by taking spectra at slightly different detector energies (the

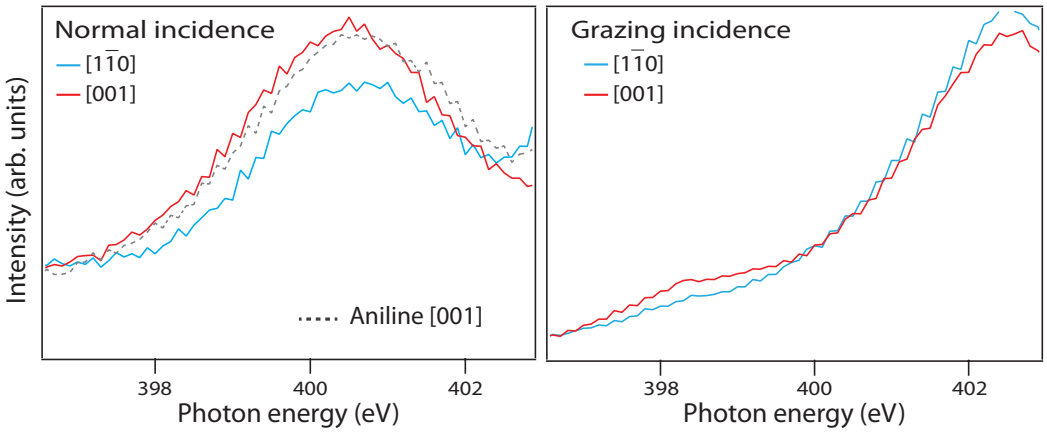

Figure 6.8: N K-edge NEXAFS spectra of azobenzene (full lines) and aniline (dashed line) on TiO_2 at normal (left) and grazing (right) incidence in the [1 $\bar{1}$ 0] (blue) and [0 0 1] (red) azimuths. No π-resonance is observed at 398 eV, and at higher energies a photoelectron peak is hindering the observation of the σ-resonance.

scans at the left were taken with the energy of the analyser set to 377 eV and for the scans at the right to 379 eV). Since this feature depends on the detected kinetic energy set up in the analyser, it was clear that it was a photoemission peak. On the right, the spectra taken at grazing incidence in both azimuths are shown. Also here, the π-resonance at 398 eV has also disappeared. However, a sharper absorption edge can be seen at 398 eV, consistent with the nitrogen double bond being broken in the great majority of the surface species, although a few intact molecules may still be present on the sample. On the left, the N K-edge spectrum for aniline on TiO_2 at normal incidence in the [0 0 1] azimuth is also shown. Note that this spectrum looks similar to the spectrum for the azobenzene-dosed sample.

Figure 6.9 shows the C K-edge NEXAFS spectra for the sample dosed with azobenzene at room temperature at both incidence angles in both azimuths. As in the case of nitrogen, a photoelectron peak, larger than the Auger signal, appeared in the C K-edge spectra at higher photon energies, hindering the observation of the σ-resonance. For a clearer picture of the π-resonance, a "zoom" into the region around the π-resonance is shown. Note that the π feature appears as a multiple peak. The splitting into two components, separated by $\approx$ 4 eV is characteristic for the benzene ring, and is seen in pure benzene in which it is attributed to different transitions into π^*-orbitals [108]. For the case of aniline, where the carbon atoms of the ring are not equivalent, there is a further splitting of the peak at 285 eV. This new peak is due to possible transitions for the different carbon atoms and appears at photon energy of 286.3 eV . The presence of the split peak is evidence that the

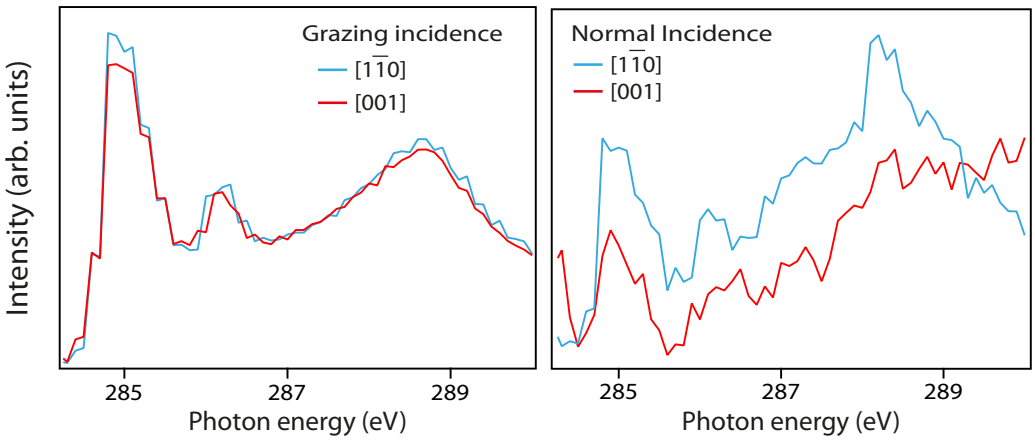

Figure 6.9: C K-edge NEXAFS spectra of azobenzene on TiO_2, at room temperature, at grazing and normal incidence in the two preferential azimuths. Here it is also obvious that the π features look very similar in every geometry, revealing a tilt of the molecule with respect to the surface normal and with no preferential azimuthal direction.

aromatic ring was still intact on the sample.

The fact that the spectra look very similar in both azimuths indicates that the aromatic ring is clearly not aligned along the low-index azimuths. The C K-edge spectrum can give information on the tilt of the molecule: if the spectrum at normal incidence shows the maximum amplitude for the π feature and minimum amplitude for the σ-resonance, the aromatic ring will have its molecular plane perpendicular to the plane of the surface, and vice versa. However, in the work presented here, the spectra show similar amplitudes of the π-resonance for normal and grazing incidence, implying that the molecular plane is neither parallel nor perpendicular to the surface, but tilted with respect to the surface normal. Another possibility is that not all the molecules adsorb on the sample with the same tilt: a molecule with the molecular plane parallel to the surface and other with the molecular plane perpendicular to the surface would result in similar NEXAFS spectra as for the tilted species. However, STM [97] shows only one identical molecule per c(2x2) unit mesh.

For comparison between the adsorbed species from azobenzene and aniline, the C K-edge spectra of aniline on titanium dioxide taken at room temperature is shown in Figure 6.10. The strong similarity between the C and N K-edge spectra at every geometry between the two adsorbed species, as in the XP spectra, is an indication of the adsorption of the same intermediate surface species with a similar

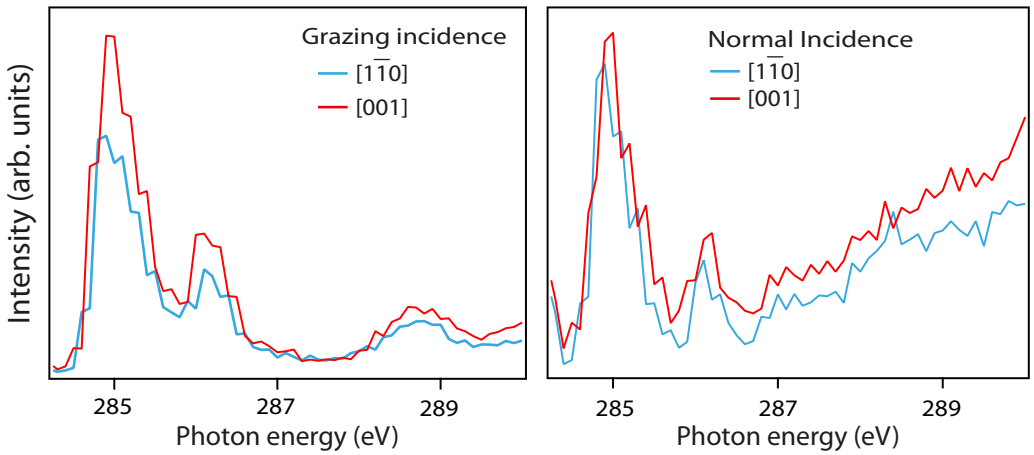

Figure 6.10: C K-edge NEXAFS spectra of aniline on TiO_2 taken at room temperature at normal and grazing incidence. The similarities of these spectra and also if compared with the azobenzene data confirm the adsorption of the same surface species, this being a phenyl imide with the molecular plane tilted with respect to the surface normal.

orientation on the surface.

6.2.2 PhD results

Experimental N 1s photoelectron diffraction scans for aniline and azobenzene were taken at room temperature at different polar and azimuth angles. Figure 6.11 shows comparisons of the modulation function, $\chi(E)$, for azobenzene and aniline at three different geometries, 0° in the [0 0 1] azimuth and 10° and 20° in the [1 $\bar{1}$ 0] azimuth. All the PhD spectra shown here were taken during the first experimental run at BESSY in November 2010. The signal for azobenzene was always much noisier than for aniline, as shown in the figure, due to the lower coverage of azobenzene observed during the first experimental run. Nevertheless, it is evident that the adsorption site of both species is the same, since all the main features are reproduced by both surface species. This result along with the results obtained from NEXAFS and XPS corroborates the conclusions of the previous STM publication [97], that the same superstructure at a phenyl imide surface species was formed.

Since the aniline data were less noisy than the azobenzene, five aniline modulation functions were chosen to pursue the analysis: 0° in the [0 0 1] azimuth, 10° in the same azimuth, 20° in the [1 $\bar{1}$ 0] azimuth and 30° in both azimuths. For the first three angles, two different data sets were taken for each geometry. In order not to lose any piece of information and also to smooth the noise, averages of the two

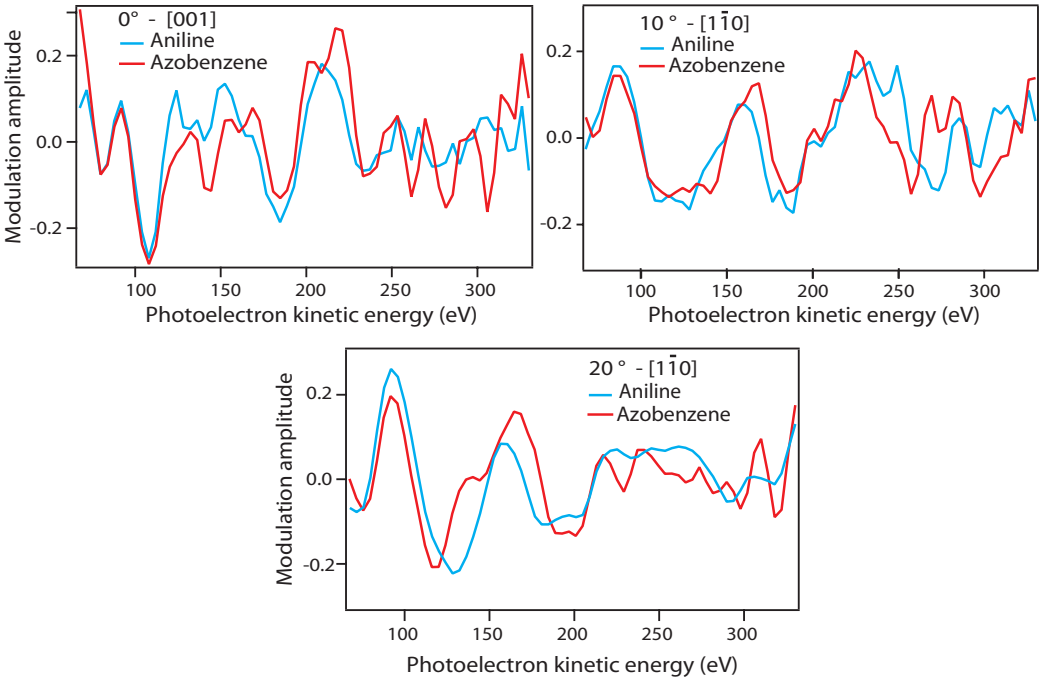

Figure 6.11: Comparison of the N 1s χ function for aniline (blue lines) and azobenzene (red lines) on TiO_2 at three different geometries. The main peaks are reproduced by both adsorbates although the modulations for azobenzene are noisier.

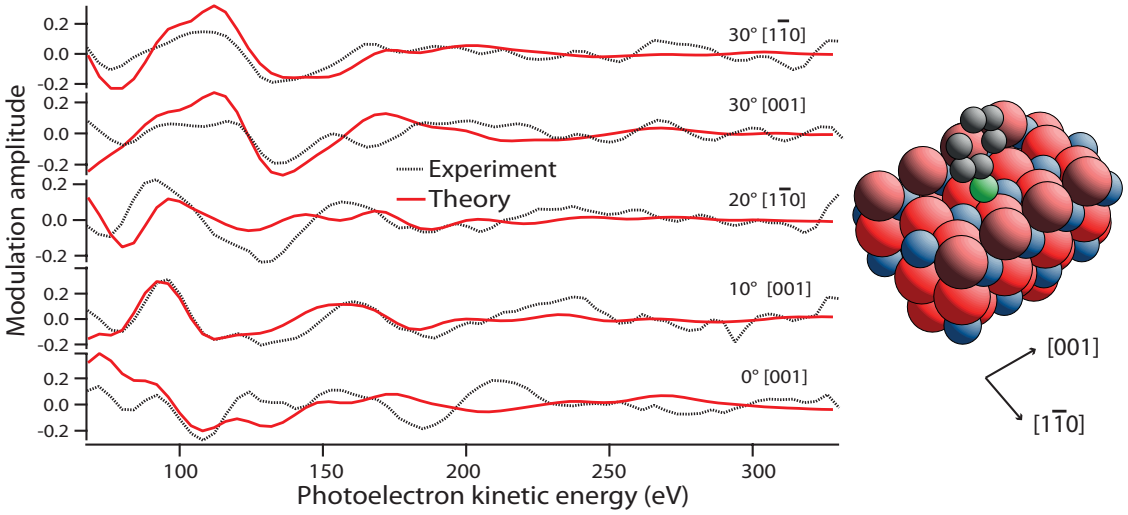

Figure 6.12: Comparison of the experimental χ functions (black) with the theoretical simulations (red) of a phenyl imide binding in a bridge site to two Ti atoms. The overall R-factor is 0.48. The adsorption site is shown on the right. The bond length between N and Ti is 2.14 Å and the phenyl ring is oriented along the [0 0 1] azimuth with a tilt of 11° from the surface normal.

scans were used in the analysis for these three angles.

All previous experiments showed clearly that the N=N bond is broken and that the aromatic ring is intact and tilted with respect to the surface normal, implying that the adsorbed species had to be a phenyl imide. However, various simulations of different adsorption sites, including the intact azobenzene molecule or a phenyl imide flat on the sample were performed. The lower R-factors were obtained for two different models: a phenyl imide species binding on a bridge site to two five-fold coordinated titanium atoms (see Figure 6.12) and for an atop site on top of the 5-fold coordinated Ti atoms (see Figure 6.15). For every adsorption site, different parameters were fitted, including also relaxations of the outermost layers of the surface. The overall R-factor for the five different geometries for the bridge site was 0.48. This number is much greater than 0.30, the value of the R-factor to be considered as a good fit (subsection 2.3.5), and it is much higher than the R-factor for the atop site.

The second model, for an atop site, as mentioned before, showed two different R-factor minima, related to different Ti-N bond lengths. For each of these local minima, the position of the atoms in the outermost layers was reoptimised using an automated fitting procedure based on a "particle swarm optimisation" algorithm [109]. Then, for these two new optimised relaxations, the N-Ti bond length

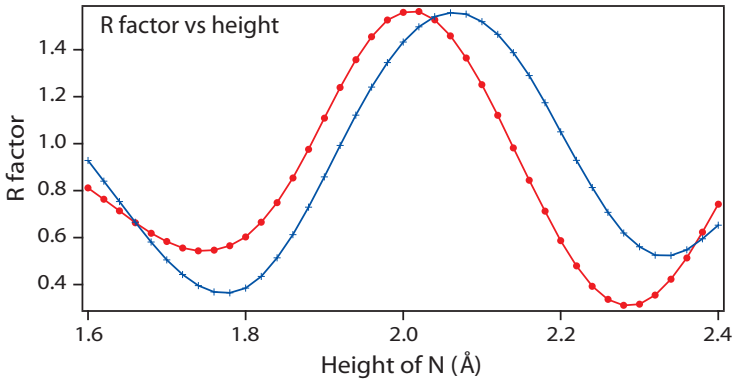

Figure 6.13: Representation of the dependence of the R-factor on the Ti-N bond length for the two different reoptimised models: in red, the surface relaxations were optimised for the longer bond length of 2.27 Å, and in blue the relaxations were optimised for the bond length between N and Ti of 1.77 Å.

was varied again and the resulting R-factors are shown in Figure 6.13. The first minimum was obtained for a bond length between N and Ti of 1.77 ± 0.05 Å with an overall R-factor of 0.36, whereas the second minimum was obtained for a longer bond length of 2.27 ± 0.04 Å. The R-factor for this second case was 0.31, slightly lower than for the shorter bond length. However, the variance of the lowest R-factor is 0.06, thus the model associated to the R-factor of 0.36 is within the error range, so either solutions are acceptable. Figure 6.13 shows the dependence of the R-factor on the height of the N atom above the surface (i.e., N-Ti bond length) for the two reoptimised models, and it shows how the relaxations favour either one or the other minimum. This multiple coincidence phenomenon is common in LEED and has also been reported previously on PhD [110]. This problem has been traditionally solved by measuring a larger data set.

Visual inspection of the modulations (Figure 6.14) reveals that both theoretical models show similarities with the experimental data. Structural studies of compounds containing Ti and N atoms [111–117] found different Ti-N bond length values, in a range from 1.77 Å to 2.40 Å. According to the literature, the shorter bond lengths are related to a double bond between the two atoms, whereas the longer bond lengths are related to a bond with bond order no more than one. In the present study, the two aromatic rings of the azobenzene molecule are linked to the N atoms, which are bonded through a double bond. It is then expected that when the molecule is cleaved by adsorption with the surface, the N atom forms also a double bond with the Ti atom, if this is bonding on an atop site. In this case, the bond length between N and Ti will be rather shorter, much closer to 1.77 Å than to

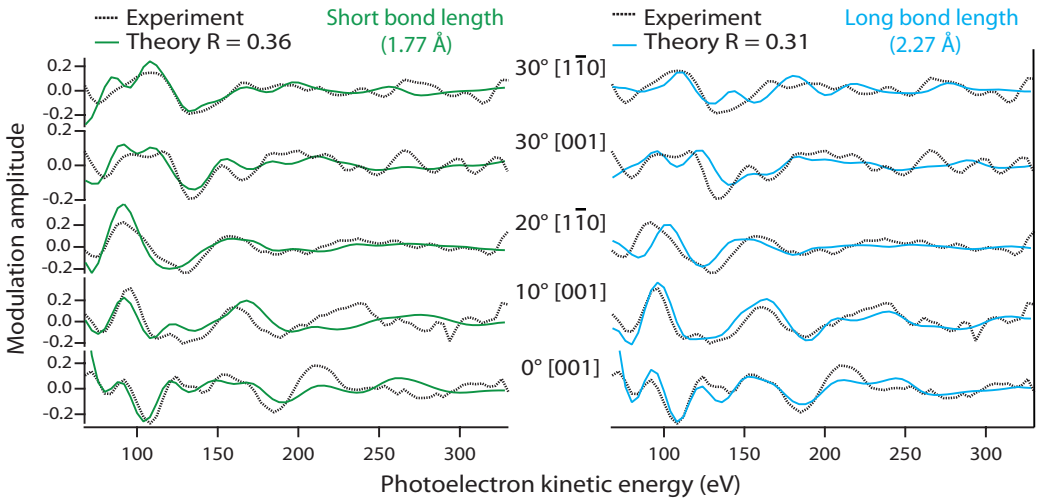

Figure 6.14: Comparison of the experimental data and theoretical simulations for a phenyl imide binding on an atop site to 5-fold coordinated Ti atoms for two different N-Ti bond lengths: on the left, the model corresponds to a N-Ti bond length of 1.77 Å and on the right, the theoretical curves simulate a model with a N-Ti bond length of 2.27 Å. The black lines represent the experimental data and the green and blue lines represent the theoretical simulations.

2.27 Å. Therefore, despite the slightly larger R-factor, the short bond length model seems more likely to be the right adsorption site.

Figure 6.15 shows the short bond length atop site model. In this model, the best fit was obtained for a tilt of the phenyl ring of 9° ± 16° with respect to the surface normal. This value is smaller than the value expected from the NEXAFS analysis, even considering the high error value. However, PhD is not very sensitive to the positions of atoms so far away from the surface. Also, a small rotation of the ring with respect to the [0 0 1] azimuth was obtained for the best fit, but the changes in the R-factor were very small.

6.3 Conclusions

Using NEXAFS and PhD, it was feasible to answer the two questions posed in the introduction. First, it was possible to demonstrate that at room temperature TiO_2 cleaves the nitrogen double bond of azobenzene, resulting in the same adsorbed species as for aniline, this being a phenyl imide species (C_6H_5N). Second, the adsorption site of this surface species was determined: the phenyl imide binds in an atop site to the five-fold coordinated Ti atoms with a bond length between N and Ti of 1.77 ± 0.05 Å. The phenyl ring is tilted with respect to the surface normal

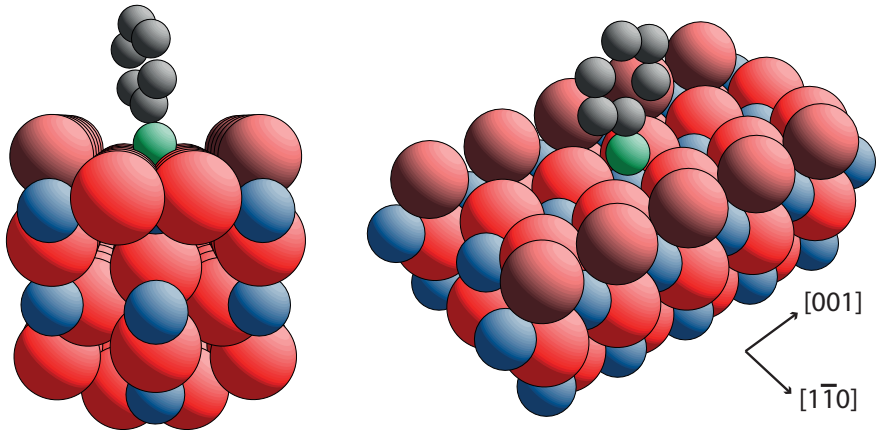

Figure 6.15: Representation of a phenyl imide species binding on an atop site on a 5-fold coordinated Ti atom, where the blue atoms represent the titanium atoms, the red ones the oxygens, the green one represents the nitrogen atom, and the grey atoms represent the carbon atoms of the aromatic ring. The hydrogen atoms are not represented, since PhD is not sensitive to them.

and is not azimuthally aligned.

An important key to solve the problem was the relaxations of the outermost layers of the surface. A comparison of the relaxations obtained for the best fit in this study and those from previous studies of the clean surface is shown in Table 6.1. Since photoelectron diffraction has an essentially local character, only the positions of atoms "close" to the emitter can be determined with precision. Positions of atoms in the deeper layers of the surface, however, can be determined with poor precision. Therefore, only relaxations for the outermost layers are shown in Table 6.1. On the other hand, the error values for the six-fold coordinated titanium atoms and for the bridging oxygens are huge, despite being rather "close" to the emitter. This can be explained by the fact that PhD is sensitive to atoms lying behind the emitter with respect to the analyser, and therefore, atoms which are almost coplanar with the emitter do not contribute as much to the PhD signal as atoms in a 180° scattering geometry. The relaxation values of the atoms for this study are within the error of the values proposed in the literature for the study of the clean surface, as shown in Table 6.1. Only the value of one parameter, the relaxation of the five-fold coordinated Ti atoms in the [1 1 0] azimuth, lies outside the error. In the case of molecules adsorbed on a metal, the relaxations are smaller than for the clean surface and the surface looks similar to the bulk. Since the phenyl imide species is actually bonded to these Ti atoms, the result is, thus, reasonable. The higher relaxation value for

Atom	LEED	MEIS	PhD	SXRD	This work
(1) Ti 6-fold	0.24±0.03	0.19±0.07	0.19±0.12	0.25±0.01	-0.15(-3.00,+2.77)
(2) Ti 5-fold	-0.19±0.03	-0.09±0.09	-0.26±0.08	-0.11±0.01	0.01(-0.05/+0.07)
(3) O bridge	0.08±0.05	0.13±0.16	0.17±0.15	0.10±0.04	0.20(-1.96/+1.60)
(4,5) O in-plane	0.19±0.08	0.05	0.00±0.25	0.17±0.03	0.24(-0.13/+0.10)
(4,5) O in-pl. in x	-0.17±0.15	0.00	-0.05±0.15	0.01±0.05	-0.09±0.20
(6) O lower bridge	0.07±0.10	0.10±0.13	0.15±0.15	0.07±0.04	0.10(-1.20/+1.90)
(9) O below 5-f.-Ti	0.00±0.08	-	-0.03±0.08	0.00±0.03	-0.01±0.10

Table 6.1: Relaxations of the near-surface Ti and O atoms in TiO_2 relative to the ideal bulk-terminated structure for the clean surface, according to the LEED [105, 106], MEIS [107], SXRD [104, 105] and PhD studies [101]. The final column corresponds to the values obtained in this study. The notation of the atoms follow the notation presented in Figure 6.16. All displacements are perpendicular to the surface except for the O in-plane atoms (4)(5), whose displacements are given also in the x direction, following the [1 $\overline{1}$ 0] azimuth. The values are given in Ångstrom; a negative value in the [1 1 0] azimuth indicates that the atoms move towards the bulk. The negative value of the relaxation in the [1 $\overline{1}$ 0] azimuth indicates that the in-plane oxygen atoms are moving further away from each other.

this surface structure is not in the [1 1 0] azimuth, but in the [1 $\overline{1}$ 0] azimuth, making the O-O distance (in-plane atoms) larger than in the bulk.

Figure 6.7 shows an issue that remains unclear. Dosing azobenzene at low temperatures led to a phase where not all the N=N bond were cleaved by TiO_2, even when the sample reached room temperature or even higher temperatures. When dosing at room temperatures, on the other hand, there is no hint of the complete azobenzene molecule. The mechanism of cleavage of the N=N bond occurs then in contact with the surface at room temperature. In the case of the multilayer at low temperatures, the molecules lie flat on the surface and a few of them remain stable on the sample even after heating it, resulting in this new phase. A similar phase where the azobenzene molecules were not dissociated on the sample was also observed by Li and Diebold [97] at low coverages.

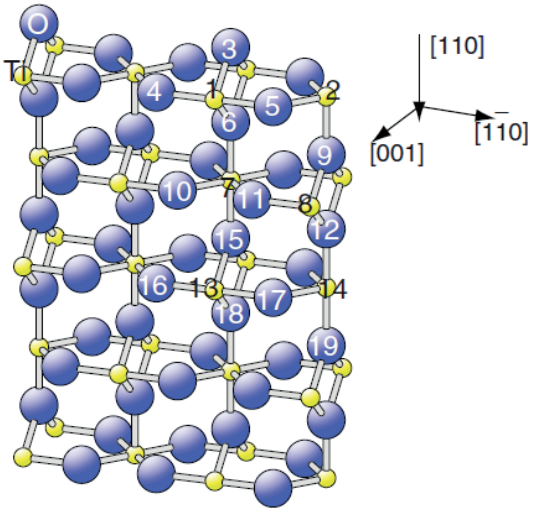

Figure 6.16: Schematic model of the clean TiO_2 surface showing atom number labels used in Table 6.1. The Ti atoms are the small yellow atoms and the blue atoms correspond to the oxygen atoms. This model is taken from [102] and the notation is following the convention of [89].

Chapter 7

Conclusions

In this thesis, the adsorption site of different adsorbates on transition metal surfaces have been successfully determined. It is known that energy-scanned photoelectron diffraction is a well-established technique in the determination of the local structure of molecules on surfaces under ultra high vacuum. Here, it has been demonstrated that it is also possible to perform structure determination with PhD at conditions much closer to "real life", as in higher-pressures (see chapter 5). However, the use of other techniques can help to solve some problems that can appear during the experiments. For example, due to its insensitivity for atoms relative "far away" from the surface, the use of NEXAFS was indispensable for the study of the phenyl imide species on titanium dioxide. DFT calculations have turned out to be very useful as a complementary tool to determine the exact adsorption site of methoxy on Cu(110), and also for this system, to reconcile the old STM results [50] with the PhD measurements. The combination of photoelectron diffraction with the mentioned techniques, and other techniques such as STM, has proved to be very successful.

PhD has been used to determine the adsorption site of the two most important surface intermediates of methanol oxidation, methoxy and formate, on different faces of copper. The local structure of methoxy on Cu(110) has been very controversial, and despite numerous studies of this system, no quantitative structural study had been yet performed. PhD found the adsorption site for this surface species to be a combination of short bridge sites along the close-packed [1 $\bar{1}$ 0] azimuthal direction with two different Cu-O bond lengths. This model includes copper adatoms, which can explain the presence of two different Cu-O bond lengths. However, inconsistencies between the PhD experimental data and the theoretical simulations for the normal emission direction led to a DFT study of this system. DFT calcu-

lations also found the short bridge site to be the most energetically favourable site and a (5x2) reconstruction model with a combination of two different short bridge sites was proposed. This (5x2) reconstruction is also in agreement with the STM study mentioned before [50]. This model was again reoptimised by PhD resulting in an overall R-factor between experiments and theory of 0.14. The model consists of a (5x2) reconstruction with 4 copper adatoms per unit cell and with 4 methoxy species. Two of these methoxy species are binding to the copper adatoms with a Cu-O bond length of 1.98 ± 0.03 Å , and the other two methoxy species are binding to the underlying unreconstructed surface with a Cu-O bond length of 1.90 ± 0.03 Å. For the determination of the final structural model, the help of DFT calculations proved to be essential.

The adsorption sites of formate on two different faces of copper, Cu(110) and Cu(111), have also been determined. Although the local adsorption site of this surface species was found to be the same for both surfaces, namely a bridge site with the oxygen atoms off-atop the copper atoms, it was surprising to find that the bond lengths between the oxygen and the copper atoms were different. The Cu-O bond length for formate on Cu(110) was found to be 1.90 ± 0.03 Å, and 1.99 ± 0.04 Å for formate on Cu(111). Thus, the difference between the two bond lengths is of 0.09 ± 0.05 Å . This significant difference implies that the underlying metal solid influences the bonding. To explain this bond length difference, two related differences between Cu(110) and Cu(111) surfaces are proposed in this thesis. First,the coordination number of the two surfaces is different: surface Cu atoms on Cu(110) are 6-fold coordinated whereas on Cu(111) they are 9-fold coordinated. The second difference between these two surfaces would be the Smoluchowski smoothing of the metal valence electron density at the surface of the more atomically-corrugated Cu(110) surface. This smoothing of the Cu(110) surface leaves its outermost surface atoms depleted of valence charge,with respect to those on the Cu(111) surface, which is atomically smoother. This depletion of charge reduces the screening of the copper nuclear charge and would be accompanied by a shorter bond length. Although there is an old study of formate on Cu(100), it would have been valuable to study the adsorption of formate on a Cu(100) surface with the same conditions as for the other two copper faces to complete the study. In the same way, it would be interesting to investigate this effect by measuring a different molecule also on different faces of a metal. However, it would be necessary that the molecule bonds in the same adsorption site on at least two different faces.

In order to investigate the possibility to perform PhD under conditions closer to "real life", the adsorption site of the surface intermediates of methanol oxidation

has been studied under reaction conditions. Whilst formaldehyde production was observed via methanol oxidation, PhD scans of the two main intermediate products, methoxy and formate, were taken. At temperatures lower than $\approx$ 450 K, the PhD scans looked very similar to those taken under UHV, implying that the adsorption site of these two surface species was the same, or at least, very similar, to the ones observed for the studies under UHV. However, at temperatures higher than $\approx$ 470 K, the PhD modulations were too weak to extract any information. Of course, at higher temperatures, the mobility of the atoms on the sample is also higher, such that the atoms are then able to hop from one site to the next one. This would decrease the amplitude of the PhD modulations. A suggestion for future investigations of PhD under reaction conditions would be to perform the experiments in a beamline equipped with an undulator, instead of a bending magnet. The intensity of the latter source, is, as mentioned in section 2.1, smaller than for beamlines equipped with an undulator, and therefore, the resolution that can typically be used is worse.

One problem in measuring this system was that it was not possible to rotate the sample, neither in the polar angle nor in the azimuthal angle. This is a particular problem for the study of molecules binding on bridge sites, where the larger modulations would appear close to polar angles of 40°. This is indeed the case for methoxy on Cu(110), as shown in chapter 3. Since the largest modulations for this system were shown for 30° and 40° of polar emission angle, tests were performed with a copper wedge mounted behind the sample in order to increase the polar angle to $\approx$ 10°. A few O 1s PhD scans were taken then for this new geometry, but the PhD scans showed no difference with the scans taken at polar angle of 0°. A possibility to improve this experiment in the future would be, therefore, to measure this system in a chamber with the appropriate capability to rotate the sample in the polar and azimuth angles. To conclude, it has been demonstrated that it is possible to perform PhD under reaction conditions, although it is very challenging, and probably, only a few chemical reactions could be successfully measured.

Finally, the adsorption of two different nitroaromatic molecules, azobenzene ($C_{12}H_{10}N_2$) and aniline (C_6H_7N), on titanium dioxide (110) were studied. A STM study performed by Li and Diebold [97] reported on the formation of the same superstructure after dosing either azobenzene and aniline. This superstructure was believed to be composed of a phenyl imide intermediate product. In order for this result to be possible, the N=N bond of the azobenzene molecule had to be cleaved by the surface. N 1s PhD scans and N and C K-edge NEXAFS spectra show that azobenzene and aniline indeed adsorb on rutile TiO_2(110) to produce the same surface species, namely a phenyl imide (C_6H_5N) binding atop on 5-fold

coordinated Ti atoms. However, two different R-factor minima, related to different Ti-N bond lengths were found. The first one is associated to a Ti-N bond length of 1.77 ± 0.05 Å and the second one of 2.27 ± 0.04 Å. The atop site model with a larger N-Ti bond length (2.27 ± 0.04 Å) resulted in a better agreement between experimental data and theoretical simulations, quantified by the R-factor (0.36 vs 0.31). However, the variance of the long bond length model is 0.06 and, therefore, both models are within the error range. Taking into account that the N atom is binding another N atom with a double bond, it is expected that the N-Ti bond length is closer to the value of 1.77 Å. Hence, the final adsorption site of the phenyl imide species is believed to be an atop site with a Ti-N bond length of 1.77 ± 0.05 Å. The multiple coincidence effect is shown in Figure 6.13. In the future, it would be interesting to measure a larger data set from this system at different emission angles, in order to overcome this ambiguity, as reported previously in a PhD investigation of PF_3 on Ni (111) by Dippel et al [110]. C K-edge NEXAFS spectra revealed information on the orientation of the aromatic ring. However, a photoemission peak appeared in the same window as the NEXAFS spectra, hindering the possibility of observing the σ-resonances and, thus, of comparing them with the π-resonances. By changing the energy of the detector, it may be possible to avoid the appearance of this photoemission peak.

Bibliography

[1] H. Rohrer, *Scanning tunneling microscopy - a surface science tool and beyond*, Surf. Sci. **299**, 956 (1994).

[2] F. Besenbacher, J. V. Lauritsen, T. R. Linderoth, E. Laegsgaard, R. T. Vang, and S. Wendt, *Atomic-scale surface science phenomena studied by scanning tunneling microscopy*, Surf. Sci. **603**, 1315 (2009).

[3] D. Woodruff and A. Delchar, *Modern techniques of surface science* (Cambridge University Press, Cambridge, UK, 1994), 2nd ed.

[4] D. Menzel, *The development of core electron spectroscopies of adsorbates*, Surf. Sci. **299**, 170 (1994).

[5] A. Jablonski, *Quantification of surface-sensitive electron spectroscopies*, Surf. Sci. **603**, 1342 (2009).

[6] B. Hayden, in [118], chap. 7, pp. 267–344.

[7] N. Avery, in [118], chap. 6, pp. 223–266.

[8] D. P. Woodruff, *Adsorbate structure determination using photoelectron diffraction: Methods and applications*, Surf. Sci. Rep. **62**, 1 (2007).

[9] J. Stöhr, *NEXAFS Spectroscopy* (Springer, Berlin, GER, 1992), 1st ed.

[10] D. Norman, *X-ray absorption-spectroscopy (EXAFS and XANES) at surfaces*, J. Phys. C Solid State **19**, 3273 (1986).

[11] J. Stöhr and D. Outka, *Determination of molecular orientations on surfaces from the angular-dependence of near-edge X-ray-absorption fine-structure spectra*, Phys. Rev. B **36**, 7891 (1987).

[12] G. Hähner, *Near edge X-ray absorption fine structure spectroscopy as a tool to probe electronic and structural properties of thin organic films and liquids*, Chem. Soc. Rev. **35**, 1244 (2006).

[13] J. Pendry, *Low energy electron diffraction* (Academic Press, London, UK, 1974), 1st ed.

[14] K. Heinz, *LEED and DLEED as modern tools for quantitative surface-structure determination*, Rep. Prog. Phys. **58**, 637 (1995).

[15] D. Woodruff, *Photoelectron and Auger electron-diffraction*, Surf. Sci. **299**, 183 (1994).

[16] D. Woodruff, *Photoelectron diffraction: past, present and future*, J. Electron. Spectrosc. **126**, 55 (2002).

[17] P. Hohenberg and W. Kohn, *Inhomogeneous Electron Gas*, Phys. Rev. B **136**, 864 (1964).

[18] W. Kohn and L. J. Sham, *Self-Consistent Equations Including Exchange and Correlation Effects*, Phys. Rev. A **140**, 1133 (1965).

[19] M. C. Payne, M. P. Teter, D. C. Allan, T. A. Arias, and J. D. Joannopoulos, *Iterative minimization techniques for ab initio total-energy calculations: molecular dynamics and conjugate gradients*, Rev. Mod. Phys. **64**, 1045 (1992).

[20] D. Sholl and J. Steckel, *Density functional theory : a practical introduction* (Wiley, Hoboken, NJ, USA, 2009), 1st ed.

[21] H. Winick, *Synchrotron radiation sources: A primer* (World Scientific, Singapore, 1994), 1st ed.

[22] *BESSY II*, Website Helmholtz Zentrum Berlin, URL: `http://www.bessy.de/bit/upload/ID_05_2.pdf`, visited in Dec. 2011.

[23] A. Einstein, *Generation and conversion of light with regard to a heuristic point of view*, Ann. Phys. (Leipzig) **17**, 132 (1905).

[24] J. Barton and D. Shirley, *Small-atom approximations for photoelectron scattering in the intermediate-energy range*, Phys. Rev. B **32**, 1906 (1985).

[25] V. Fritzsche, *Approximations for photoelectron scattering*, Surf. Sci. **213**, 648 (1989).

[26] V. Fritzsche, *A new spherical-wave approximation for photoelectron diffraction, EXAFS and MEED*, J. Phys.-Condens. Mat. **2** (1990).

[27] V. Fritzsche, *Consequences of a finite-energy resolution for photoelectron diffraction spectra*, Surf. Sci. **265**, 187 (1992).

[28] V. Fritzsche and J. Pendry, *Linear-superposition method for the multiple-scattering problem in low-energy-photoelectron diffraction*, Phys. Rev. B **48**, 9054 (1993).

[29] V. Fritzsche, *Calculation of Auger-electron diffraction at a Ni(111) surface*, J. Phys.-Condens. Mat. **2**, 9735 (1990).

[30] A. Rubinowicz, *Quantum Mechanics* (Elsevier Science, Amsterdam, NL, 1968), 1st ed.

[31] P. Lee, P. Citrin, P. Eisenberger, and B. Kincaid, *Extended X-ray absorption fine-structure - its strengths and limitations as a structural tool*, Rev. Mod. Phys. **53**, 769 (1981).

[32] V. Fritzsche, K. Schindler, P. Gardner, A. Bradshaw, M. Asensio, and D. Woodruff, *The effect of anisotropic molecular vibrations in photoelectron diffraction of adsorbed species*, Surf. Sci. **269**, 35 (1992).

[33] *EA 125 Energy Analyser*, Website Omicron Nanotechnology (2002), URL: `http://uhv.cheme.cmu.edu/manuals/M470101.pdf`, visited in Dec. 2011.

[34] J. Pendry, *Reliability factors for LEED calculations*, J. Phys. C Solid State **13**, 937 (1980).

[35] R. Dippel, K. Weiss, K. Schindler, P. Gardner, V. Fritzsche, A. Bradshaw, M. Asensio, X. Hu, D. Woodruff, and A. Gonzalez Elipe, *A photoelectron diffraction study of the structure of PF_3 adsorbed on Ni(111)*, Chem. Phys. Lett. **199**, 625 (1992).

[36] N. Booth, R. Davis, R. Toomes, D. Woodruff, C. Hirschmugl, K. Schindler, O. Schaff, V. Fernandez, A. Theobald, P. Hofmann, R. Lindsay, T. Giessel, P. Baumgartel, and A. Bradshaw, *Structure determination of ammonia on Cu(110) - a low-symmetry adsorption site*, Surf. Sci. **387**, 152 (1997).

[37] R. Terborg, J. Hoeft, M. Polcik, R. Lindsay, O. Schaff, A. Bradshaw, R. Toomes, N. Booth, D. Woodruff, E. Rotenberg, and J. Denlinger, *The coverage dependence of the local structure of C on Ni(100): A structural precursor to adsorbate-induced reconstruction*, Surf. Sci. **446**, 301 (2000).

[38] D. P. Woodruff, *The structure of surfaces: What do we know and what would we like to know?*, J. Phys.-Condens. Mat. **22** (2010).

[39] P. Watson, M. Van Hove, and K. Hermann, NIST Surface Structure Database Ver. 5.0, NIST Gaithersburg, MD (2003), URL: `http://www.nist.gov/srd/nist42.cfm`, visited in Dec. 2011.

[40] A. Puschmann, J. Haase, M. D. Crapper, C. E. Riley, and D. P. Woodruff, *Structure determination of the formate intermediate on copper (110) by use of X-ray-absorption fine-structure measurements*, Phys. Rev. Lett. **54**, 2250 (1985).

[41] I. Wachs and R. Madix, *Selective oxidation of CH_3OH to H_2CO on a copper (110) catalyst*, J. Catal. **53**, 208 (1978).

[42] M. Bowker and R. Madix, *XPS, UPS and thermal-desorption studies of alcohol adsorption on Cu(110). 1. Methanol*, Surf. Sci. **95**, 190 (1980).

[43] B. Sexton, A. Hughes, and N. Avery, *A spectroscopic study of the adsorption and reactions of methanol, formaldehyde and methyl formate on clean and oxygenated Cu(110) surfaces*, Surf. Sci. **155**, 366 (1985).

[44] E. Holubkrappe, K. Prince, K. Horn, and D. Woodruff, *X-ray photoelectron diffraction determination of the molecular-orientation of CO and methoxy adsorbed on Cu(110)*, Surf. Sci. **173**, 176 (1986).

[45] P. Singnurkar, I. Bako, H. P. Koch, E. Demirci, A. Winkler, and R. Schennach, *DFT and RAIRS investigations of methanol on Cu(110) and on oxygen-modified Cu(110)*, J. Phys. C Solid State **112**, 14034 (2008).

[46] U. Jayasooriya, C. Anson, O. Aljowder, G. Dalfonso, P. Stanghellini, and R. Rossetti, *Vibrational assignments for methoxy ligands on metal-clusters - interpretation of RAIRS data fromt methoxy groups on single-crystal copper surfaces*, Surf. Sci. **294**, 131 (1993).

[47] A. Peremans, F. Maseri, J. Darville, and J. Gilles, *Infrared characterization of methanol adsorbed on Cu(110)*, J. Vac. Sci. Technol. A-Vac. Surf. Films **8**, 3224 (1990).

[48] S. Francis, F. Leibsle, S. Haq, N. Xiang, and M. Bowker, *Methanol oxidation on Cu(110)*, Surf. Sci. **315**, 284 (1994).

[49] F. Leibsle, S. Francis, R. Davis, N. Xiang, S. Haq, and M. Bowker, *Scanning-tunneling-microscopy studies of formaldehyde synthesis on Cu(110)*, Phys. Rev. Lett. **72**, 2569 (1994).

[50] F. Leibsle, S. Francis, S. Haq, and M. Bowker, *Aspects of formaldehyde synthesis on Cu(110) as studied by STM*, Surf. Sci. **318**, 46 (1994).

[51] A. Carley, A. Owens, M. Rajumon, M. Roberts, and S. Jackson, *Oxidation of methanol at copper surfaces*, Catal. Lett. **37**, 79 (1996).

[52] A. Carley, P. Davies, G. Mariotti, and S. Read, *Reaction pathways in methanol oxidation at Cu(110) surfaces*, Surf. Sci. **364**, L525 (1996).

[53] S. Poulston, A. Jones, R. Bennett, and M. Bowker, *Contrasting reaction pathways in methanol oxidation on Cu(110) studied by STM*, J. Phys.-Condens. Mat. **8**, L765 (1996).

[54] A. Jones, S. Poulston, R. Bennett, and M. Bowker, *Methanol oxidation to formate on Cu(110) studied by STM*, Surf. Sci. **380**, 31 (1997).

[55] S. Poulston, A. Jones, R. Bennett, and M. Bowker, *Identifying molecular species in scanning tunnelling microscopy images - reply*, J. Phys.-Condens. Mat. **9**, 8791 (1997).

[56] F. Leibsle, *Identifying molecular species in scanning tunnelling microscopy images - comment*, J. Phys.-Condens. Mat. **9**, 8787 (1997).

[57] F. Leibsle, *Clues to identifying methoxy and formate structures in scanning tunneling microscopy experiments*, Surf. Sci. **401**, 153 (1998).

[58] S. Silva, R. Lemor, and F. Leibsle, *STM studies of methanol oxidation to formate on Cu(110) surfaces: I. Sequential dosing experiments*, Surf. Sci. **421**, 135 (1999).

[59] S. Silva, R. Lemor, and F. Leibsle, *STM studies of methanol oxidation to formate on Cu(110) surfaces: II. Codosing experiments*, Surf. Sci. **421**, 146 (1999).

[60] L. Zhou, S. Gunther, and R. Imbihl, *Low-pressure methanol oxidation over a Cu(110) surface under stationary conditions: (I) reaction kinetics*, J. Catal. **230**, 166 (2005).

[61] L. Zhou, S. Gunther, and R. Imbihl, *Low-pressure methanol oxidation over a Cu(110) surface under stationary conditions: (II) adsorbate coverages and reactivity*, J. Catal. **232**, 295 (2005).

[62] S. Günther, L. Zhou, M. Hävecker, A. Knop-Gericke, E. Kleimenov, R. Schlögl, and R. Imbihl, *Adsorbate coverages and surface reactivity in methanol oxidation over Cu(110): An in situ photoelectron spectroscopy study*, J. Chem. Phys. **125** (2006).

[63] S. Sakong and A. Gross, *Total oxidation of methanol on Cu(110): A density functional theory study*, J. Phys. Chem. A **111**, 8814 (2007).

[64] C. Ammon, A. Bayer, G. Held, B. Richter, T. Schmidt, and H. Steinruck, *Dissociation and oxidation of methanol on Cu(110)*, Surf. Sci. **507**, 845 (2002).

[65] D. P. Woodruff, C. F. McConville, A. L. D. Kilcoyne, T. Lindner, J. Somers, M. Surman, G. Paolucci, and A. M. Bradshaw, *The structure of the formate species on copper surfaces: New photoelectron diffraction results and SEXAFS data reassessed*, Surf. Sci. **201**, 228 (1988).

[66] D. Kreikemeyer-Lorenzo, W. Unterberger, D. A. Duncan, M. K. Bradley, T. J. Lerotholi, J. Robinson, and D. P. Woodruff, *Face-dependent bond lengths in molecular chemisorption: The formate species on Cu(111) and Cu(110)*, Phys. Rev. Lett. **107**, 046102 (2011).

[67] D. P. Woodruff, *The local structure of molecular reaction intermediates at surfaces*, Chem. Soc. Rev. **37**, 2262 (2008).

[68] M. K. Bradley, D. Kreikemeyer Lorenzo, W. Unterberger, D. A. Duncan, T. J. Lerotholi, J. Robinson, and D. P. Woodruff, *Methoxy species on Cu(110). Understanding the local structure of a key catalytic reaction intermediate*, Phys. Rev. Lett. **105** (2010).

[69] D. Kreikemeyer Lorenzo, M. K. Bradley, W. Unterberger, D. A. Duncan, T. J. Lerotholi, J. Robinson, and D. P. Woodruff, *The structure of methoxy species on Cu(110). A combined photoelectron diffraction and density functional theory determination*, Surf. Sci. **605**, 193 (2010).

[70] S. Clark, M. Segall, C. Pickard, P. Hasnip, M. Probert, K. Refson, and M. Payne, *First principles methods using CASTEP*, Z. Kristallogr. **220**, 567 (2005).

[71] S. Sakong and A. Gross, *Density functional theory study of the partial oxidation of methanol on copper surfaces*, J. Catal. **231**, 420 (2005).

[72] J. M.R. Albert, J. T. Yates, *The Surface Scientist's Guide to Organometallic Chemistry* (J. Am. Chem. Soc., Washington, DC, USA, 1987).

[73] M. Bowker, *Active sites in methanol oxidation on Cu(110) determined by STM and molecular beam measurements*, Top. Catal. **3**, 461 (1996).

[74] J. Stöhr, D. A. Outka, R. J. Madix, and U. Döbler, *Evidence for a novel chemisorption bond: Formate (HCO_2) on copper (100)*, Phys. Rev. Lett. **54**, 1256 (1985).

[75] M. Crapper, C. Riley, and D. Woodruff, *The structure of formate on copper (100) and copper (110) surfaces*, Surf. Sci. **184**, 121 (1987).

[76] A. Sotiropoulos, P. K. Milligan, B. C. C. Cowie, and M. Kadodwala, *A structural study of formate on Cu(111)*, Surf. Sci. **444**, 52 (2000).

[77] U. Doebler, K. Baberschke, J. Stoehr, and D. A. Outka, *Structure of c(2x2) oxygen on copper(100): A surface extended X-ray absorption fine-structure study*, Phys. Rev. B **31**, 2532 (1985).

[78] G. A. Barclay and C. H. L. Kennard, *Crystal structure of anhydrous copper(II) formate*, J. Chem. Soc. pp. 3289–3294 (1961).

[79] K.-U. Weiss, R. Dippel, K.-M. Schindler, P. Gardner, V. Fritzsche, A. M. Bradshaw, A. L. D. Kilcoyne, and D. P. Woodruff, *Chemical shift photoelectron diffraction from molecular adsorbates*, Phys. Rev. Lett. **69**, 3196 (1992).

[80] M. Pascal, C. L. A. Lamont, M. Kittel, J. T. Hoeft, R. Terborg, M. Polcik, J. H. Kang, R. Toomes, and D. P. Woodruff, *Quantitative structural determination of the high coverage phase of the benzoate species on Cu(110)*, Surf. Sci. **492**, 285 (2001).

[81] S. M. Johnston, G. Rousseau, V. Dhanak, and M. Kadodwala, *The structure of acetate and trifluoroacetate on Cu(111)*, Surf. Sci. **477**, 163 (2001).

[82] D. M. Goodgame, N. J. Hill, D. F. Marsham, A. C. Skapski, M. L. Smart, and P. G. Troughto, *Insignificance of metal-metal bonding in antiferromagnetism of copper (II) carboxylate dimers*, J. Chem. Soc. D pp. 629–630 (1969).

[83] A. Golobic, M. Malekov, and P. Segedin, *catena-poly[disodium [[diformato-tricopper(II)]-di-956;3-formato-tetra-956;2-formato]]: a new mode of bridging between binuclear and mononuclear formate-copper(II) units*, Acta Crystallog. C **62**, m102 (2006).

[84] R. Joyner, M. Roberts, and K. Yates, *High-pressure electron spectrometer for surface studies*, Surf. Sci. **87**, 501 (1979).

[85] H. Ruppender, M. Grunze, C. Kong, and M. Wilmers, *Insitu X-ray photoelectron-spectroscopy of surfaces at pressures up to 1 mbar*, Surf. Interface Anal. **15**, 245 (1990).

[86] V. Bukhtiyarov, I. Prosvirin, E. Tikhomirov, V. Kaichev, A. Sorokin, and V. Evstigneev, *In situ study of selective oxidation of methanol to formaldehyde over copper*, React. Kinet. Catal. L. **79**, 181 (2003).

[87] H. Bluhm, M. Havecker, A. Knop-Gericke, E. Kleimenov, R. Schlogl, D. Teschner, V. Bukhtiyarov, D. Ogletree, and M. Salmeron, *Methanol oxidation on a copper catalyst investigated using in situ X-ray photoelectron spectroscopy*, J. Phys. Chem. B **108**, 14340 (2004).

[88] *Methods: High-pressure XPS/XAS*, Website of the Electronic Structure group, Dept. of Inorganic Chemistry, Fritz-Haber-Institut der Max-Planck-Gesellschaft (2009), URL: `http://www.fhi-berlin.mpg.de/acnew/groups/electronicstructure/pages/methods/pages/electronicstructure_group__methods__xps.pdf`, visited in Dec. 2011.

[89] U. Diebold, *The surface science of titanium dioxide*, Surf. Sci. Rep. **48**, 53 (2003).

[90] M. Haruta, *Size- and support-dependency in the catalysis of gold*, Catal. Today **36**, 153 (1997).

[91] M. Valden, X. Lai, and D. Goodman, *Onset of catalytic activity of gold clusters on titania with the appearance of nonmetallic properties*, Science **281**, 1647 (1998).

[92] H. Freund, *Clusters and islands on oxides: from catalysis via electronics and magnetism to optics*, Surf. Sci. **500**, 271 (2002).

[93] L. Molina, M. Rasmussen, and B. Hammer, *Adsorption of O_2 and oxidation of CO at Au nanoparticles supported by TiO_2(110)*, J. Chem. Phys. **120**, 7673 (2004).

[94] A. Vijay, G. Mills, and H. Metiu, *Adsorption of gold on stoichiometric and reduced rutile TiO_2(110) surfaces*, J. Chem. Phys. **118**, 6536 (2003).

[95] A. Corma and P. Serna, *Chemoselective hydrogenation of nitro compounds with supported gold catalysts*, Science **313**, 332 (2006).

[96] A. Grirrane, A. Corma, and H. Garcia, *Gold-catalyzed synthesis of aromatic azo compounds from anilines and nitroaromatics*, Science **322**, 1661 (2008).

[97] S.-C. Li and U. Diebold, *Reactivity of TiO_2 rutile and anatase surfaces toward nitroaromatics*, J. Am. Chem. Soc. **132**, 64 (2010).

[98] C. L. Pang, R. Lindsay, and G. Thornton, *Chemical reactions on rutile TiO_2(110)*, Chem. Soc. Rev. **37**, 2328 (2008).

[99] J. Jamieson, B. Olinger, F. Dachille, P. Simons, and R. Roy, *Pressure-temperature studies of anatase, brookite rutile and TiO_2 (II) - a discussion*, Am. Mineral. **54**, 1477 (1969).

[100] R.W.G.Wyckoff, *Crystal Structures* (Wiley, New York, NY, USA, 1963), 2nd ed.

[101] E. A. Kröeger, D. I. Sayago, F. Allegretti, M. J. Knight, M. Polcik, W. Unterberger, T. J. Lerotholi, K. A. Hogan, C. L. A. Lamont, and D. P. Woodruff, *Photoelectron diffraction investigation of the structure of the clean TiO_2(110) (1x1) surface*, Phys. Rev. B **75** (2007).

[102] W. Unterberger, T. J. Lerotholi, E. A. Kroeger, M. J. Knight, D. A. Duncan, D. Kreikemeyer-Lorenzo, K. A. Hogan, D. C. Jackson, R. Wlodarczyk, M. Sierka, J. Sauer, and D. P. Woodruff, *Local hydroxyl adsorption geometry on TiO_2(110)*, Phys. Rev. B **84** (2011).

[103] G. Charlton, P. Howes, C. Nicklin, P. Steadman, J. Taylor, C. Muryn, S. Harte, J. Mercer, R. McGrath, D. Norman, T. Turner, and G. Thornton, *Relaxation of TiO_2(110)-(1x1) using surface X-ray diffraction*, Phys. Rev. Lett. **78**, 495 (1997).

[104] G. Cabailh, X. Torrelles, R. Lindsay, O. Bikondoa, I. Joumard, J. Zegenhagen, and G. Thornton, *Geometric structure of TiO_2(110) (1x1): Achieving experimental consensus*, Phys. Rev. B **75** (2007).

[105] W. Busayaporn, X. Torrelles, A. Wander, S. Tomic, A. Ernst, B. Montanari, N. M. Harrison, O. Bikondoa, I. Joumard, J. Zegenhagen, G. Cabailh,

G. Thornton, and R. Lindsay, *Geometric structure of TiO_2(110) (1x1): Confirming experimental conclusions*, Phys. Rev. B **81** (2010).

[106] R. Lindsay, A. Wander, A. Ernst, B. Montanari, G. Thornton, and N. Harrison, *Revisiting the surface structure of TiO_2(110): A quantitative low-energy electron diffraction study*, Phys. Rev. Lett. **94** (2005).

[107] G. Parkinson, M. Munoz-Marquez, P. Quinn, M. Gladys, R. Tanner, D. Woodruff, P. Bailey, and T. Noakes, *Medium-energy ion-scattering study of the structure of clean TiO_2(110) (1x1)*, Phys. Rev. B **73**, 245409 (2006).

[108] J. Solomon, R. Madix, and J. Stöhr, *Orientation and absolute coverage of benzene, aniline, and phenol on Ag(110) determined by NEXAFS and XPS*, Surf. Sci. **255**, 12 (1991).

[109] D. Duncan, J. Choi, and D. Woodruff, *Global search algorithms in surface structure determination using photoelectron diffraction*, Surf. Sci. (2011), published online. DOI:10.1016/j.susc.2011.10.003.

[110] R. Dippel, K. Weiss, K. Schindler, D. Woodruff, P. Gardner, V. Fritzsche, A. Bradshaw, and M. Asensio, *Multiple site coincidences and their resolution in photoelectron diffraction - PF_3 adsorbed on Ni(111)*, Surf. Sci. **287**, 465 (1993).

[111] M. Grün, K. Harms, R. Kocker, and K. Dehnicke, *Crystal structures of $[TiF_3(NPPh_3)(HNPPh_3)]_2$ and of $HNPPh_3$*, Z. Anorg. Allg. Chem. **622**, 1091 (1996).

[112] F. Rioux, M. Schmidt, and M. Gordon, *Molecular structures for azatitanatranes*, Organometallics **16**, 158 (1997).

[113] M. Siodmiak, G. Frenking, and A. Korkin, *Theoretical ab initio study of $TiCl_4$ ammonolysis: gas phase reaction of TiN chemical vapor deposition*, J. Mol. Model. **6**, 413 (2000).

[114] Y. Sarazin, R. H. Howard, D. L. Hughes, S. M. Humphrey, and M. Bochmann, *Titanium, zinc and alkaline-earth metal complexes supported by bulky O,N,N,O-multidentate ligands: syntheses, characterisation and activity in cyclic ester polymerisation*, Dalton Trans. pp. 340–350 (2006).

[115] I. Guzei, A. Baboul, G. Yap, A. Rheingold, H. Schlegel, and C. Winter, *Surprising titanium complexes bearing η^2-pyrazolato ligands: Synthesis, structure, and molecular orbital studies*, J. Am. Chem. Soc. **119**, 3387 (1997).

[116] E. Brady, J. Telford, G. Mitchell, and W. Lukens, *Amido-bis(pentamethylcyclopentadienyl)titanium(III)*, Acta Crystallog. C **51**, 558 (1995).

[117] D. A. Kissounko, J. M. Hoerter, I. A. Guzei, Q. Cui, S. H. Gellman, and S. S. Stahl, *Ti-IV-mediated reactions between primary amines and secondary carboxamides: Amidine formation versus transamidation*, J. Am. Chem. Soc. **129**, 1776 (2007).

[118] J. Yates and T. Madey, eds., *Vibrational spectroscopy of molecules on surfaces*, vol. 1 (Plenum Press, New York, NY, USA, 1987), 1st ed.